*Doklady Physics, Vol. 48, No. 5, 2003, pp. 203–205. Translated from Doklady Akademii Nauk, Vol. 390, No. 1, 2003, pp. 32–34.*


**PHYSICS**

# A Stable Method for Reconstructing a Relaxation-Time Spectrum According to Data of Dynamic Experiments

**V. A. Dubovitskiĭ and V. I. Irzhak**

Presented by Academician G.M. Éliashberg November 14, 2002

Received December 12, 2002

In many problems of polymer physics, it becomes necessary to reconstruct the density $\rho(\tau)$ of the mode distribution $\exp\left(-\frac{t}{\tau}\right)$ over relaxation times [1]. The spectrum of the relaxation times makes it possible to describe in broad limits rheological properties of polymers. At the same time, this spectrum is assumed to be closely related to the structure of macromolecules [2].

It is considered that initially predetermined arbitrariness is inherent in well-known methods of describing relaxation spectra [3, 4]. This arbitrariness is manifested in attempts of interpreting experimental data. For example, in the case of the discrete description method, while realizing different fitting procedures, it is easy to obtain unboundedly many complexes of relaxation times and discrete-mode weights. These complexes describe experimental curves with a given accuracy but have no direct correlation either with each other or with the polymer structure. In the continuous description method, an ill-posed problem arises of reconstructing $\rho(\tau)$ as a solution to a linear integral equation of the first kind, which is traditionally solved by regularization methods. In this case, the arbitrariness of reconstructing $\rho(\tau)$ is masked by the method of the organization of the regularization process and discretization of the integral equation. However, it was noted [3] that, in spite of the apparent arbitrariness in describing the relaxation spectrum, its integral characteristics very often reveal an entirely consistent behavior.

In this paper, we suggest a method that allows the indicated discrepancies to be overcome.

In the discrete variant, the relaxation function $g(t)$ being experimentally measured and the corresponding complex function $G(\omega)$ of the frequency modulus are related to the relaxation spectrum [2] by the formula

$$g(t) = \sum_{k=1}^{N} \exp\left(-\frac{t}{\tau_k}\right)\rho_k, \quad G(\omega) = \sum_{k=1}^{N} \frac{i\omega\tau_k}{1 + i\omega\tau_k}\rho_k. \quad (1)$$

Here, $\{\tau_k, \rho_k\}$, $k = 1, 2, \ldots, N$ is a set of $N$ relaxation times and weights of the corresponding modes. In the continuous variant, formula (1) has the form

$$g(t) = \int_0^\infty \exp\left(-\frac{t}{\tau}\right)\rho(\tau)d\tau,$$
$$G(\omega) = \int_0^\infty \frac{i\omega\tau}{1 + i\omega\tau}\rho(\tau)d\tau. \quad (2)$$

According to their physical sense, the values $\tau_k$, $\rho_k$, and $\rho(\tau)$ are nonnegative. The kinetic function and frequency function are related to each other by the Fourier transformation

$$G(\omega) = i\omega\int_0^\infty \exp(-it\omega)g(t)dt.$$

Representations (1) and (2) admit their natural unification in terms of distribution functions and Stieltjes integral construction. We now assume [5, 6] that the relaxation spectrum is described by the distribution function $P(\tau)$, where $P(\tau)$ is the integral intensity of the relaxation spectrum in the half-interval $[0, \tau)$. The function $P(\tau)$ is defined on the extended semiaxis $R_+ = [0, \infty]$ so that $P(0) = 0$. This function is continuous to the left for $0 < \tau < \infty$ but it may have discontinuities at the points $\tau = 0, \infty$. These end discontinuities exist in the case of purely elastic and inert contribution, respectively, to the relaxation spectrum. We denote the totality of all distribution functions in $R_+$ as $M(R_+)$ and express

*Institute for Problems in Chemical Physics, Russian Academy of Sciences, Chernogolovka, Moscow oblast, 142432 Russia*
*e-mail: dubv@icp.ac.ru; irzhak@icp.ac.ru*

1028-3358/03/4805-0203$24.00 

the functions $g(t)$ and $G(\omega)$ by an integral in the Stieltjes sense [7] with respect to $P(\tau)$:

$$g(t) = \int_0^\infty \exp\left(-\frac{t}{\tau}\right) dP(\tau), \quad G(\omega) = \int_0^\infty \frac{i\omega\tau}{1 + i\omega\tau} dP(\tau). \quad (3)$$

In terms of the Stieltjes integral, the steplike distribution function

$$P(\tau) = \sum_{k=1}^{N} \rho_k h(\tau - \tau_k),$$

corresponds to discrete case (1). Here, $h$ is the Heaviside step function. The distribution function

$$P(\tau) = \int_0^\tau \rho(\xi) d\xi,$$

corresponds to the continuous variant; i.e., $P(\tau)$ is the antiderivative of the density $\rho(\tau)$.

In order to avoid an uncertainty in formulas (3) at $\tau = 0$, we complement the definition of the integrand kernels setting $a(t, \tau) = \exp\left(-\frac{t}{\tau}\right)$, $b(\omega, \tau) = \frac{i\omega\tau}{1 + i\omega\tau}$ at $\tau > 0$ and $a(t, \tau) = \delta_{0t}$, $b(\omega, \tau) = \delta_{\infty\omega}$ at $\tau = 0$, where $\delta_{xy}$ is the Kronecker delta. Thus, written out in a rigorous form, formulas (3) are transformed to

$$g(t) = \int a(t, \tau) dP(\tau), \quad G(\omega) = \int b(\omega, \tau) dP(\tau).$$

In applications associated with reconstructing the function $P(\tau)$, a question of the uniqueness of this function and its stability to perturbations of both $g(t)$ and $G(\omega)$ unavoidably arises. We restrict our further analysis to construction of $P(\tau)$ according to the kinetic function $g(t)$, since the description of the frequency-reconstruction variant differs negligibly.

The property of uniqueness follows from the property of unambiguous reversibility of the Laplace transformation. The property of stability is formulated in terms of the weak convergence of monotonous functions on $R_+$ [7, 8] similarly to the following continuity principle.

Let $g_n$, $P_n$ ($n = 1, 2, \ldots$), $g$, $P$ be the sequence composed of kinetic curves and of the corresponding distribution functions. Then, the convergence $g_n(t) \longrightarrow g(t)$ for all $0 \le t < \infty$ is equivalent to the weak convergence $P_n \Rightarrow P$ on $R_+$.

This statement is proved by combining the Helly theorem on the choice of a convergent subsequence of monotonic functions and the property of uniqueness.

The convergence condition for $g_n(t)$ at $t = 0$ is rather important. If it is then eliminated from the convergence $g_n(t) \longrightarrow g(t)$ at $t > 0$, it follows only that $\lim P_n(\tau) = P(\tau) + Ch(\tau)$, where $C$ is an arbitrary constant.

The properties of the uniqueness and continuity imply that the inverse problem

$$A[P] = g, \quad P \in M(R_+), \quad (4)$$

where $A[P](t) = \int_0^\infty a(t, \tau)\, dP(\tau)$ is an integral operator, belongs to a well-posed problem in the classic Hadamard sense for the functions $g$ belonging to the transform $Z = A[M(R_+)]$. Here, $Z$ is treated as a space with the metric $\rho(z_1, z_2) = |z_1(0) - z_2(0)| + \int |z_1(t) - z_2(t)|\, dt$ or its equivalent. It is worth noting that $Z$ has an independent faithful description: it is a class of absolutely monotonic Bernstein functions [8].

Due to the limited convexity of the definition region and the region of values, operator equation (4) is not the traditional linear equation of the first kind. These are the limitations that provide continuous reversibility of the affine operator $A$: $M(R_+) \longrightarrow Z$ and, consequently, the correctness of inverse problem (4).

It is well known that from the weak convergence of the distribution functions $P_n \Rightarrow P$ follows the convergence of the Stieltjes integral

$$\lim \int f(\tau) dP_n(\tau) = \int f(\tau) dP(\tau)$$

for an arbitrary function $f(\tau)$ continuous on $R_+$. Hence, it follows that the integral moments of the distributions converge when the corresponding kinetic functions $g_n(t)$ converge pointwise, and the distributions $P_n(\tau)$, in themselves, are concentrated within the range $\tau \le C$ of relaxation times.

When measuring $g(t)$ experimentally, we obtain a function with a noise component certainly violating the fine descriptive condition of the solvability $g \in Z$. Therefore, after the extremal problem

$$\int_T \nu(dt) |A[P] - g|^q \longrightarrow \min \text{ for } P \in M(R_+) \quad (5)$$

has been analyzed, we introduce a natural notion of the generalized solution. Here, $q$, $\nu(dt)$, $T$ are the parameters of the functional being minimized, namely, $q > 1$ is the Hölder index, $T$ is the set of nonnegative numbers of measurement times, and $\nu(dt)$ is a certain nonnegative Radon weight measure. It is finite and locally positive on $T$, has a jump at $t = 0$, i.e., $\nu(\{0\}) > 0$. The set $T$ must contain 0 and must have a finite positive limiting point. For example, $T = \{0\} \cup [t_1, t_2]$ is suitable, where $t_1 < t_2$.

In expression (5), the minimum is sought among monotonic functions of the class $M(R_+)$. Solution (5) is called the optimal integral representation of the function $g$ over the kernel $a(t, \tau)$ in the Banach space $L_q(T, \nu)$. The following property of uniqueness and stability is valid for optimal integral representation.

(a) For any arbitrary function $g \in L_q(T, \nu)$, there exists a unique optimal distribution $P[g]$.

(b) If the sequence of the functions $g_n$ is weakly convergent in $L_q(T, \nu)$ to $g$, then the corresponding optimal integral representations weakly converge as monotonic functions on $R_+$, i.e., $P[g_n] \Rightarrow P[g]$.

Thus, the optimal integral representations are especially stable: they are stable to integrated small errors and even ignore the white noise with arbitrary amplitude, which is superimposed on the true function $g(t)$.

While setting extremal problem (5), it is theoretically admissible to use an arbitrary finite positive weight measure $\nu(dt)$ and the Hölder index $q$ that control the contribution to the measurement functional at different $t$ and the sensitivity of the functional to large spikes.

In the case of numerical realization of the method, we deal with a finite set of measurement times $T = \{t_j\}$, $j = 1, 2, \ldots, n$. We perform the discretization of the continuous problem introducing a fixed net of nodes $\{\tau_i\}$, $i = 1, 2, \ldots, m$. The desired distribution function is approximated by the steplike combination $P(\tau) = \sum_{i=1}^{m} \alpha_i h(\tau - \tau_i)$.

Instead of infinite-dimensional extremal problem (5), we now obtain

$$J(\alpha) = \sum_{j=1}^{n} \nu_j \left| \sum_{i=1}^{m} a(t_j, \tau_i)\alpha_i - g(t_j) \right|^q \to \min, \quad \alpha_i \geq 0, \quad i = 1, 2, \ldots, m, \tag{6}$$

where $\nu_j$ is a set of fixed positive weight coefficients. This is the problem of minimizing a finite-dimensional convex function on a cone of nonnegative vectors. In its solution, the logarithmic penalization method [9] combined with the second-order descent is rather efficient, which results in rapidly convergent iterations. In the usual case of employing the index $q = 2$, problem (6) relates to the quadratic programming, and the NNLS finite-step algorithm [10] is applied in solving the problem.

In order to attain a good approximation of continuous problem (5) by discrete problem (6), a sufficiently dense net of nodes $\tau_i$, $t_j$ about tens per decade is necessary, which covers the region of a possible concentration of the relaxation spectrum. Among moments of measurements of $T$ and among discretization nodes, it is desirable (but not necessarily) to have $t = 0$ and $\tau = 0$, $\infty$, respectively. The window of the concentration of positive times $t$ must be wider to both sides by an order of magnitude than the window of positive nodes $\tau_i$. This allows the manifestation of the degeneration of the matrix columns $\{a(t_j, \tau_i)\}$ to be avoided As a result, the typical dimension of problem (6), which we meet in applications, is rather high ($m, n \sim 300$). The practice of solving problem (6) has shown that the method of disposing calculation nodes $\{\tau_i\}$ does not affect the quality of the solution, only the net density is important. Although different sets of weights are calculated for different representations of nodes, the corresponding final primitive steplike distribution functions coincide with each other within an accuracy determined by both the density of the nets and the error in $g(t)$. The nonuniqueness of the solution (undetermined case) possible in the case of $m > n$ is insignificant. In practice, it is reasonable to distribute finite positive nodes $\tau$ uniformly in the logarithmic scale and equalize weights for $t > 0$. These practical observations are consistent with the theory of the correctness of the optimal integral representation, which was described above.

## ACKNOWLEDGMENTS

This work was supported by the Russian Foundation for Basic Research "Podmoskov'e," project no. 01-03-97001.

## REFERENCES

1. H. H. Winter, J. Non-Newtonian Fluid Mech. **68**, 225 (1997).
2. G. M. Bartenev and A. G. Barteneva, *Relaxation Properties of Polymers* (Khimiya, Moscow, 1992).
3. A. Ya. Malkin and I. Masalova, Rheol. Acta **40**, 261 (2001).
4. A. Ya. Malkin, Vysokomol. Soedin., Ser. A **44**, 1598 (2002).
5. V. A. Dubovitskiĭ and I. A. Milyutina, Preprint OIKhF Akad. Nauk SSSR (Otd. Inst. Khim. Fiz., Chernogolovka, 1985).
6. V. A. Dubovitskiĭ and K. V. Ermolaev, Zh. Fiz. Khim. **70**, 1233 (1996).
7. É. Kh. Gokhman, *Stieltjes Integral and Its Applications* (Fizmatgiz, Moscow, 1958).
8. G. E. Shilov and V. A. Gurevich, *Integral, Measure, and Derivative* (Nauka, Moscow, 1967).
9. A. Fiacco and G. McCormick, *Nonlinear Programming: Sequential Unconstrained Minimization Techniques* (Wiley, New York, 1968; Mir, Moscow, 1972).
10. C. L. Lawson and R. J. Hanson, *Solving Least Squares Problems* (Prentice-Hall, Englewood Cliffs, N.J., 1974).

*Translated by G. Merzon*

*Doklady Physics, Vol. 48, No. 5, 2003, pp. 206–208. Translated from Doklady Akademii Nauk, Vol. 390, No. 1, 2003, pp. 35–38.*


**PHYSICS**

# Superionic Transition and Self-Propagating High-Temperature Synthesis of Copper Selenide in Thin Films

**V. G. Myagkov[1,*], L. E. Bykova[1], and G. N. Bondarenko[2]**

Presented by Academician V.V. Osiko January 23, 2003

Received November 28, 2002

An increase in the reactivity of reagents under crystallographic transformations in solid-state synthesis is known as the Hedvall effect (see, e.g., [1]). However, as was shown in [2–5], solid-state reactions in thin films are initiated independently of crystallographic transformations in reagents and begin at temperatures of structural solid-state transformations in the reaction products. In particular, the initiation temperature in a Fe/S bilayer film system is determined by the temperature of the metal–dielectric phase transition in iron monosulphide (FeS) [2]. Solid-state synthesis in Cu/Au films occurs in the mode of self-propagating high-temperature synthesis (SHS) whose initiation temperature coincides with the temperature of the order–disorder transition in a CuAu alloy [3]. The connection of solid-state reactions in Ni/Ti and Cd/Au thin-film samples with martensitic transformations in NiTi and AuCd alloys was studied in [4, 5]. The general rule of the formation of the first phase and phase sequence in bilayer films and multilayers with increasing annealing temperature was formulated in [4] as follows. The first phase forming at the film interface is a phase with the minimum temperature of structural phase transformations in the phase diagram. Further phase formation with an increase in the annealing temperature for solid-state reactions in thin films is determined by structural transformations in a given binary system. The initiation temperatures of solid-state reactions coincide with the temperatures of structural phase transitions.

The first-phase rule indicates that the initiation temperatures $T_0$ of synthesis in bilayer films and multilayers are equal to the temperatures $T_K$ of solid-state transitions in the corresponding binary systems and implies that the mechanisms of synthesis and phase separation are of primary importance in solid-state transformations.

The aim of this work is to expand the first-phase rule to superionic transformations by the example of solid-state synthesis of copper selenide in the Se/Cu thin-film system.

In the Se–Cu system, the low-temperature $\alpha$-$Cu_2Se$ phase, whose structure is not definitely determined, is transformed to the cubic superionic high-temperature $\beta$ phase at a temperature of $T_K \sim 380$–$400$ K. The superionic-transformation temperature $T_K$ decreases strongly with deviation from stoichiometry, and $T_K$ for $Cu_{2-x}Se$ samples with $x \sim 0.2$ is about room temperature. The $\beta$-$Cu_2Se$ superionic phase exhibits mixed conductivity, whose ionic component is about 10% [6].

The experiments were carried out with bilayer film systems consisting of Cu and Se layers obtained by sequential deposition on glass substrates and freshly spalled (001)MgO surface. The thicknesses of Cu and Se films were in the ranges 50–100 and 100–200 nm, respectively. More complete data concerning the conditions of the production of bilayer film samples and initiation of SHS in them were given in [2–4]. The original bilayer samples exhibit reflexes only from (111) and (200) Cu planes, which indicates primary growth in these planes with respect to the glass substrate (Fig. 1a). The absence of reflexes from Se implies that it is grown amorphous or small-crystalline on the Cu surface. Samples were heated at a rate of $\eta \sim 1$ K/s. The solid-state reaction between Cu and Se layers was initiated at a substrate temperature of $T_S \sim 380$ K and occurred in the SHS mode, whose front propagated typically for SHS in thin films. Figure 2 shows the relative resistance $R$ as a function of the substrate temperature $T_S$. Behind the SHS front, there is a region where the color of the original film changes. However, diffraction patterns do not indicate the formation of compounds in this region. It likely exists due to the melting or structural transformation of amorphous selenium. Analysis of reacted Se/Cu film samples indicates that synthesis occurs over the entire thickness of a film. As follows from diffraction

[1] *Kirenskiĭ Institute of Physics, Siberian Division, Russian Academy of Sciences, Akademgorodok, Krasnoyarsk, 660036 Russia*

[2] *Institute of Chemistry and Chemical Technology, Siberian Division, Russian Academy of Sciences, Krasnoyarsk, Russia*

* *e-mail: miagkov@iph.krasn.ru*

1028-3358/03/4805-0206$24.00 

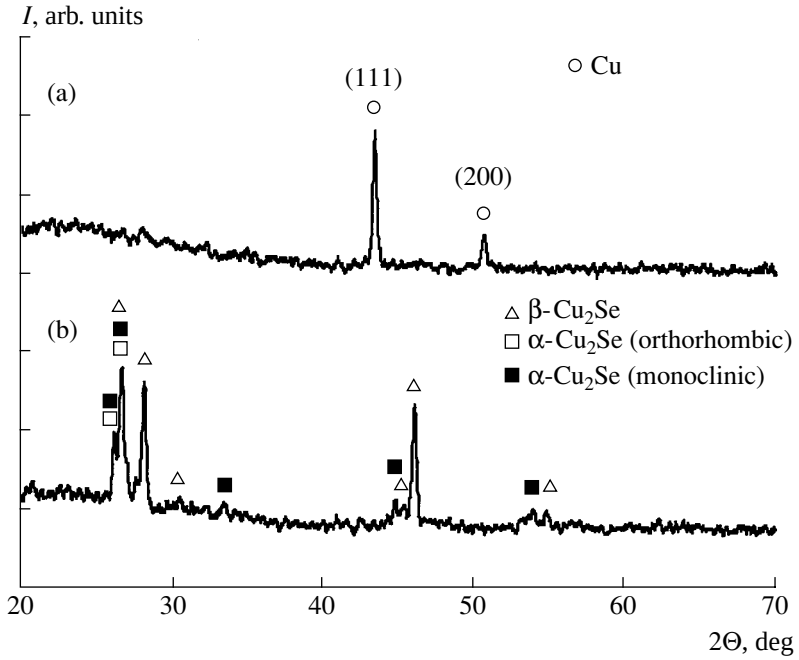


**Fig. 1.** Diffraction patterns of the Se/Cu bilayer film system: (a) before the reaction, (b) after the passage of the SHS wave through the original sample and after the secondary initiation of SHS in the film system consisting of the $Cu_2Se$ reacted sample and the Se layer deposited on it.

patterns, reacted samples (Fig. 1b) consist of a mixture of the α-$Cu_2Se$ and β-$Cu_2Se$ phases. The reaction products can also include CuSe and $Cu_3Se_2$ phases due to the $Cu_2Se$–$Cu_{2-x}Se$ and CuSe–$Cu_3Se_2$ phase transformations as a result of aging and thermal processing [7, 8]. Reacted samples do not include the nonstoichiometric $Cu_{2-x}Se$ phase, which is always present when other obtaining methods are used [7–10]. The most substantial feature is the possibility of continuing solid-state synthesis if a reacted $Cu_2Se$ sample is covered by an Se layer. The reaction in these Se/$Cu_2Se$ and Se/$Cu_2Se$/Cu film systems occurs in the SHS mode and is initiated at the same temperature $T_0$ = 380 K. The diffraction pattern from twice-reacted samples was similar to that from samples reacted only once (Fig. 1b). The continuation of the reaction implies that synthesis in Se/$Cu_2Se$ and Se/$Cu_2Se$/Cu film systems is accompanied by the formation of nonstoichiometric $Cu_{2-x}Se$ phase, as well as CuSe and $Cu_3Se_2$ phases, which exist in a wide composition range and can be produced from $Cu_2Se$ phase.

Solid-state synthesis in bilayer film systems can also be initiated if the upper layer is deposited at the substrate temperature $T_S$ above the initiation temperature $T_0$ ($T_S > T_0$). When Se is deposed on a single-crystal Cu(001) surface grown on a MgO(001) spall, the diffraction pattern involves only reflexes with interplane spacings $d_1$ = 0.68 nm and $d_2$ = 0.34 nm. These reflexes correspond to reflections from (110) and (220) planes of the (card 19-0401 JCPSD) orthorhombic form, from (111) and (222) planes of the (card 29-568 JCPSD) tetragonal form, or from (030) and (060) planes of the (card 27-1131 JCPSD) monoclinic form of the α-$Cu_2Se$ phase. Self-propagating high-temperature synthesis often leads to single-crystal reaction products [11]. The formation of an α-$Cu_2Se$ single-crystal layer on the Cu(001) surface implies that atomic transport through a reaction product in synthesis is directed and ordered. This deterministic atomic motion is responsible for oriented growth with the formation of orientational relations between reagents and reaction products.

The initiation temperature $T_0$ of SHS in Se/Cu bilayer films is equal to the temperature $T_K$ of the superionic transition in $Cu_2Se$ phase, and the reaction products include the $Cu_2Se$ phase and phases to which it is transformed. Therefore, solid-state synthesis in Se/Cu film systems is determined by the superionic transition in the $Cu_2Se$ phase and satisfies the first-phase rule presented above. Assuming that the initial resistance $R_0$ corresponds to the resistance of the original sample and the final resistance $R_K$ corresponds to the reaction products, we conclude that the reaction rate $\kappa(T_S)$ depends on the substrate temperature $T_S$ as $\frac{R(T_S) - R_0}{\eta(R_K - R_0)}$. Assuming that $\eta$ in this relation is constant and $\kappa(T_S) = A\exp\left(-\frac{E_a}{kT_S}\right)$, where $A$ is constant, we obtain the reaction activation energy $E_a$ from $R(T_S)$ (Fig. 2). This energy is equal to 0.9 eV near the initiation temperature. This value agrees with the low energy of ionic-

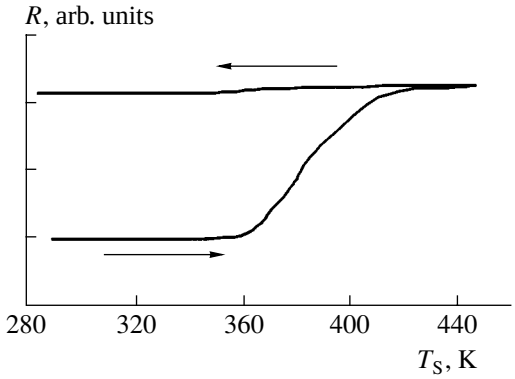


**Fig. 2.** Relative resistance $R$ vs. the substrate temperature $T_S$ for the heating rate $\eta \sim 1$ K/s of the Se/Cu bilayer film sample. The arrows show the direct and reverse variation in resistance.

conductivity activation, which does not exceed 0.3–0.4 eV in the superionic state [12].

Let us assume that the reaction front starts at the interface and propagates inside the film with the SHS front velocity $V_f$ in the film plane. In this case, the lower limit of the diffusion coefficient when the SHS front passes is estimated as $D_{eff} = V_f d \sim 10^{-9}$ m$^2$/s, where $d$ = 100 nm is the thickness of the reacted layer and $V_f$ = 100 m/s is the front velocity near the initiation temperature. This estimate coincides with the diffusion coefficients of $Ag^+$ cations in Ag-based superionic conductors [12]. The above results imply common mechanisms of solid-state synthesis and fast ionic transport and make it possible to propose the following model of solid-state synthesis in Se/Cu bilayer systems determined by the superionic transformation in the $Cu_2Se$ phase. The interface between film condensates after chemisorption is a 2D reaction product, which is a germ of the first phase. When the temperature of the bilayer film exceeds the superionic transformation temperature ($T_S > T_K$), the 2D germ of the first phase is transformed to the $Cu_2Se$ superionic phase. Since the cation mobility of Cu atoms is high in the superionic state, copper cations migrate through the 2D β-$Cu_2Se$ layer of the reaction products into the selenium film. The transport of Cu cation lines through the β-$Cu_2Se$ layer must occur via cooperative jumps from one crystallographic position to another in channels coinciding with conductivity channels [12] and must be directed, which ensures a low energy of synthesis activation. Self-organization in the motion of Cu cations is responsible for the growth of a new epitaxial β-$Cu_2Se$ layer at the interface with selenium. As the substrate temperature decreases below the initiation temperature ($T_S < T_0$), the high-temperature β-$Cu_2Se$ phase is transformed to the low-temperature α-$Cu_2Se$ phase and synthesis is damped.

In conclusion, we note that SHS in thin films propagates to a depth up to 200 nm and indicates that synthesis mechanisms are long-range. The way of the migration of atoms to the reaction zone is important. The kinetics of front propagation are independent of the kind of the solid-state transformation (order–disorder transition, martensitic transformation, or superionic transition) determining SHS in thin films. This property implies that these transformations have a common physicochemical mechanism. Indeed, the order–disorder phase transition can proceed through the martensitic mechanism (see, e.g., [13]). The similarity between martensitic and superionic transformations was previously analyzed in [1, 14]. Since the activation energy is low and mobility of atoms is high at $T_S > T_0 = T_K$, diffusionless, martensitic-like, and collective mechanisms of atomic transport can play the primary role in the solid-state transformation and at the initial stage of solid-state synthesis in thin films.

## ACKNOWLEDGMENTS

This work was supported by the Krasnoyarsk Science Foundation (project no. 11F001C) and MMK–AUSFERR–Intels Foundation (grant no. 10-03-02).

## REFERENCES

1. Yu. D. Tret'yakov, *Solid-State Reactions* (Khimiya, Moscow, 1978).
2. V. G. Myagkov, L. E. Bykova, V. S. Zhigalov, *et al.*, Dokl. Akad. Nauk **371**, 763 (2000) [Dokl. Phys. **45**, 157 (2000)].
3. V. G. Myagkov, L. E. Bykova, G. N. Bondarenko, *et al.*, Pis'ma Zh. Éksp. Teor. Fiz. **71**, 268 (2000) [JETP Lett. **71**, 183 (2000)].
4. V. G. Myagkov, L. E. Bykova, L. A. Li, *et al.*, Dokl. Akad. Nauk **382**, 463 (2002) [Dokl. Phys. **47**, 95 (2002)].
5. V. G. Myagkov, L. E. Bykova, and G. N. Bondarenko, Dokl. Akad. Nauk **388**, 46 (2003).
6. N. N. Bikkulova, S. A. Danilkin, Kh. Fuss, *et al.*, in *Phase Transformations in Solid Solutions and Alloys* (OMA-II, Sochi, 2001), pp. 49–50.
7. M. Lakohmi, K. Bindu, and K. P. Viyayakumar, Thin Solid Films **386** (1), 127 (2001).
8. C. Levy-Clement, M. Neumann-Spallart, S. K. Haram, and K. S. V. Santhanam, Thin Solid Films **302** (1/2), 12 (1997).
9. S. Xu, H. Wang, J.-J. Zhu, and H.-Y. Chen, J. Cryst. Growth **234** (1), 263 (2002).
10. N. Nancheva, P. Docheva, N. Piourelov, and M. Balcheva, Mater. Lett. **54** (2/3), 169 (2002).
11. V. G. Myagkov, L. E. Bykova, and G. N. Bondarenko, Dokl. Akad. Nauk **368**, 715 (1999) [Dokl. Phys. **44**, 667 (1999)].
12. L. O. Atov'yan and E. A. Ukshe, in *Physical Chemistry* (Khimiya, Moscow, 1983), pp. 92–115.
13. Ch. S. Barret and T. B. Massal'skiĭ, *Metal Structure* (Metallurgiya, Moscow, 1984).
14. J. C. Phillips, Electrochim. Acta **22** (6), 709 (1977).

*Translated by R. Tyapaev*

*Doklady Physics, Vol. 48, No. 5, 2003, pp. 209–215. Translated from Doklady Akademii Nauk, Vol. 390, No. 1, 2003, pp. 39–45.*


**PHYSICS**

# Crystal Structure of a New Microporous $Na_2\{Al_3(OH)_2[PO_4]_3\}$ Aluminum Phosphate

**O. V. Yakubovich*, O. V. Dimitrova, and Corresponding Member of the RAS V. S. Urusov**

Received December 5, 2002

Investigations of the last decade significantly extended the list of known zeolite-like compounds, whose crystal structure is based on mixed frameworks composed of various anion polyhedra. In addition to the well-known natural and artificial zeolites with the Al and Si tetrahedron frameworks, a large number of microporous phases with three-dimensional anion constructions based on Zn–P, Be–P, Zn–As, Al–P, and other cation matrices were found [1–6]. Oxygen complexes of amphoteric metals in combination with $[PO_4]^{3-}$ acid complex anions form mixed anion frameworks containing pores or channels, where either alkaline or organic cations are located. In this group of compounds, which are often used as molecular sieves as an alternative to aluminum silicates, aluminum phosphates are most studied. Systematically investigating aluminum phosphates, we synthesized one more such compound.

In this work, we study colorless transparent isometric well-cut crystals up to 5 mm in size, which were produced in standard Teflon-lined 4-$cm^3$ autoclaves by the method of soft hydrothermal synthesis ($T$ = 250°C and $P$ = 100 atm). A mechanical mixture of $Na_2O$–$Al_2O_3$–$P_2O_5$–$B_2O_3$ components prepared in equal weight amounts was introduced into a water-filled autoclave. Experiments continued for 18–20 days. The diffraction pattern recorded from a powder sample by a DRON UM diffractometer indicated that the synthesized compound is original. The X-ray analysis (CanScan 4DV) showed that this phase include Na, Al, and P atoms.

Investigating a single crystal with a SYNTEX $P\bar{1}$ four-circle autodiffractometer, we found that the parameters of a rhombic (pseudotetragonal) unit cell are $a$ = 8.475(2) Å, $b$ = 8.471(2) Å, and $c$ = 14.319(3) Å. Experimental data needed to interpret the structure were obtained with the same diffractometer (Mo$K_\alpha$ radiation) by the 2θ : θ-scanning method. The intensities of reflexes were adjusted with allowance for the Lorenz factor and polarization effect.

Calculations were made with the SHELX program package [7, 8] by using the curves of atomic scattering and the corrections for anomalous dispersion taken from [9]. We could not find a structural model in the framework of the tetragonal symmetry ($P4_22_12$ space group). For this reason, we supposed that the crystal has rhombic symmetry, and the pseudotetragonal symmetry results from merohedric or pseudomerohedric microtwinning. The structure was determined by direct methods and refined in the anisotropic full-matrix approximation with allowance for absorption and secondary isotropic extinction. In the absence of chemical analysis, atoms were identified by taking into account the composition of the system in the process of crystal synthesis, interatomic spacings, temperature factors, and the character of ellipsoids of thermal vibrations. Allowance for pseudotetragonal twinning showed that the samples under investigation contain two kinds of objects with different orientations in a ratio of 0.440(3) : 0.560(3). The Flack parameter [10] testified to the proper choice of an "absolute" acentric configuration ($P2_12_12_1$ space group). The structure is described by the formula

$$Na_2\{Al_3(OH)_2[PO_4]_3\}.$$

The positions of hydrogen atoms were localized by difference synthesis of the electron density and refined in the isotropic approximation. The crystallographic characteristics of the new phase, data of X-ray analysis, and refinement parameters of the structure are listed in Table 1. The coordinates of basic atoms (with the anisotropic and equivalent temperature factors) and interatomic spacings are presented in Tables 2 and 3, respectively. Table 4 presents the geometric characteristics of hydrogen bonds. The local balance of valences including the contribution of protons [11, 12] is given in Table 5.

The crystal structure is formed by two types of Al polyhedra (in three nonequivalent positions)—octa-

*Moscow State University,*
*Vorob'evy gory, Moscow, 119899 Russia*
** e-mail: yakubol@geol.msu.ru*

1028-3358/03/4805-0209$24.00 

**Table 1.** Crystallographic characteristics and data of the experiment and structure refinement

| | |
|---|---|
| Crystallographic characteristics | |
| Chemical formula | $Na_2\{Al_3(OH)_2[PO_4]_3\}$ |
| Absorption μ, $mm^{-1}$ | 1.014 |
| Space group | $P2_12_12_1$ |
| The number of formula units $Z$ | 4 |
| Parameters of a unit cell, Å: | |
| $a$ | 8.475(2) |
| $b$ | 8.471(2) |
| $c$ | 14.319(3) |
| Unit-cell volume $V$, $Å^3$ | 1028.0(4) |
| Density ρ, $g/cm^3$ | 2.881 |
| Experimental data | |
| Diffractometer | SYNTEX $P\bar{1}$ |
| Radiation | Mo$K_\alpha$ (Graphite monochromator) |
| Temperature, K | 293 |
| Measured range: $\theta_{max}$ | 35°00 |
| Data of structure refinement | |
| The number of reflection: independent $I$ and observed with $I > 1.96\sigma(I)$ | 2404/2251 |
| Refinement method | in $F^2$ |
| The number of refined parameters | 206 |
| Correction for absorption | DIFABS |
| $T_{max}$, $T_{min}$ | 1.000, 0.758 |
| Uncertainty parameters: | |
| $R$ (for observed reflexes) | 0.046 |
| $wR_2$ (for all independent reflexes) | 0.099 |
| $s$ | 1.099 |
| Extinction coefficient | 0.0004(7) |
| Residual election density, $e/Å^3$ | $\rho_{max} = 0.71$, $\rho_{min} = -0.65$ |

and pentahedra. The shape of Al1 octahedra is rather regular, and they are larger than Al2 and Al3 pentahedra. Cation–oxygen interatomic spacings in Al1 octahedra vary from 1.869 to 1.909 Å (the average value is equal to 1.891 Å), while the average spacings in Al2 and Al3 polyhedra are equal to 1.830 and 1.832 Å, respectively. The *cis*-type conformation is typical for $AlO_4(OH)_2$ octahedra. The bond lengths between Al atoms and two OH groups in the *cis*-position are minimal in a polyhedron and are equal to 1.869 and 1.880 Å. One vertex in each of the Al2 and Al3 pentahedra is also occupied by a hydroxyl group, but the interatomic spacings (Al2–OH = 1.801 Å and Al3–OH = 1.842 Å) are not minimal in the corresponding polyhedra. Although the mean aluminum–oxygen bond lengths in pentahedra coincide to within the limits of experimental error (0.005 Å), it is seen (Table 3) that the spread of the lengths in Al2 polyhedra is wider. For example, Al2–O interatomic lengths lie in the range 1.782–1.884 Å, whereas the minimum and maximum Al3–O lengths in Al3 pentahedra are equal to 1.795 and 1.858 Å, respectively.

**Table 2.** Coordinates of the basic atoms and equivalent and anisotropic thermal parameters (Å$^2$)

| Atom | *x*/*a* | *y*/*b* | *z*/*c* | $U_{eq}$ | $U_{11}$ | $U_{22}$ | $U_{33}$ | $U_{23}$ | $U_{13}$ | $U_{12}$ |
|---|---|---|---|---|---|---|---|---|---|---|
| Al1 | 0.6540(2) | 0.6181(2) | 0.0418(2) | 0.0072(3) | 0.0090(8) | 0.0053(7) | 0.0073(6) | –0.0001(7) | 0.0009(7) | 0.0002(6) |
| Al2 | 0.8631(2) | 0.3832(3) | 0.1994(1) | 0.0078(3) | 0.0089(9) | 0.0077(8) | 0.0070(7) | 0.0005(7) | 0.0001(6) | 0.0010(6) |
| Al3 | 0.3923(2) | 0.1099(2) | 0.1134(1) | 0.0080(3) | 0.0075(7) | 0.0083(8) | –0.0006(7) | 0.0006(7) | 0.0005(6) | –0.0003(6) |
| P1 | 0.5369(2) | 0.2837(2) | 0.2924(1) | 0.0070(2) | 0.0084(7) | 0.0067(7) | 0.0058(4) | 0.0002(5) | 0.0009(5) | 0.0005(5) |
| P2 | 0.9712(2) | 0.7247(2) | 0.1280(1) | 0.0067(2) | 0.0060(7) | 0.0067(7) | 0.0075(5) | 0.0001(5) | –0.0005(5) | –0.0003(4) |
| P3 | 0.0508(2) | 0.2021(2) | 0.0459(1) | 0.0073(2) | 0.0079(6) | 0.0061(7) | 0.0079(5) | –0.0018(6) | –0.0006(5) | 0.0008(5) |
| Na1 | 0.7603(4) | 0.9798(4) | –0.0365(3) | 0.0374(9) | 0.019(1) | 0.021(2) | 0.073(2) | 0.002(2) | –0.011(2) | –0.005(1) |
| Na2 | 0.2205(4) | 0.5008(4) | 0.2890(3) | 0.0402(10) | 0.017(2) | 0.024(2) | 0.080(3) | 0.023(2) | –0.009(2) | –0.006(1) |
| O1 | 0.5150(6) | 0.1813(6) | 0.3796(3) | 0.0109(9) | 0.012(2) | 0.010(2) | 0.011(2) | 0.003(2) | 0.001(2) | –0.003(2) |
| O2 | 0.0167(6) | 0.0359(5) | 0.0097(3) | 0.0086(8) | 0.011(2) | 0.007(2) | 0.008(2) | –0.002(2) | 0.003(2) | –0.003(2) |
| O3 | 0.7035(5) | 0.4725(5) | 0.1353(3) | 0.0141(9) | 0.010(2) | 0.013(2) | 0.019(2) | 0.010(2) | –0.006(2) | –0.003(2) |
| O4 | 0.3131(5) | 0.9488(5) | 0.0408(4) | 0.0099(7) | 0.012(2) | 0.008(2) | 0.010(1) | 0.001(2) | –0.005(2) | 0.001(2) |
| O5 | 0.8023(6) | 0.7628(6) | 0.0940(3) | 0.0107(8) | 0.009(2) | 0.009(2) | 0.014(2) | 0.001(2) | –0.001(2) | 0.002(2) |
| O6 | 0.9233(6) | 0.2333(6) | 0.1197(3) | 0.0102(9) | 0.013(2) | 0.012(2) | 0.006(2) | –0.004(2) | 0.001(2) | –0.003(2) |
| O7 | 0.0081(6) | 0.8526(6) | 0.2014(3) | 0.0109(9) | 0.011(2) | 0.007(2) | 0.014(2) | 0.000(2) | –0.003(2) | –0.000(2) |
| O8 | 0.5868(5) | 0.7713(6) | –0.0460(3) | 0.0087(8) | 0.009(2) | 0.012(2) | 0.005(2) | 0.003(2) | –0.002(2) | –0.001(2) |
| O9 | 0.9869(6) | 0.5599(6) | 0.1716(3) | 0.0103(9) | 0.012(2) | 0.007(2) | 0.012(2) | 0.003(1) | –0.003(2) | –0.001(2) |
| O10 | 0.2917(6) | 0.7613(6) | 0.2395(3) | 0.0108(9) | 0.007(2) | 0.010(2) | 0.015(2) | –0.002(2) | 0.003(2) | 0.003(2) |
| O11 | 0.4231(6) | 0.2479(6) | 0.2125(3) | 0.0114(9) | 0.013(2) | 0.010(2) | 0.011(2) | –0.005(2) | –0.003(2) | –0.001(2) |
| O12 | 0.5032(6) | 0.4589(5) | 0.3176(3) | 0.0101(8) | 0.009(2) | 0.007(2) | 0.014(2) | –0.000(2) | –0.002(2) | 0.003(2) |
| O13 | 0.2143(6) | 0.2233(6) | 0.0892(4) | 0.0128(9) | 0.006(2) | 0.013(2) | 0.019(2) | –0.003(2) | –0.002(2) | 0.003(2) |
| O14 | 0.0423(6) | 0.3243(6) | –0.0339(3) | 0.0120(9) | 0.009(2) | 0.011(2) | 0.016(2) | 0.008(2) | –0.000(2) | –0.003(2) |
| H1 | 0.63(1) | 0.44(1) | 0.137(8) | 0.05(3) | | | | | | |
| H2 | 0.36(1) | 0.88(1) | 0.043(8) | 0.04(3) | | | | | | |

Note: For H atoms, the isotropic thermal factors are presented.

**Table 3.** Interatomic spacings, Å

| Al1-octahedron | | Al2-pentahedron | | Al3-pentahedron | | P1-tetrahedron | |
|---|---|---|---|---|---|---|---|
| Al1–O3 | 1.869(5) | Al2–O6 | 1.782(5) | Al3–O14 | 1.795(5) | P1–O11 | 1.527(5) |
| O4 | 1.880(5) | O3 | 1.801(5) | O13 | 1.821(5) | O1 | 1.531(5) |
| O8 | 1.895(5) | O7 | 1.810(5) | O4 | 1.842(5) | O10 | 1.535(5) |
| O2 | 1.896(5) | O9 | 1.871(5) | O12 | 1.844(5) | O12 | 1.553(5) |
| O1 | 1.899(5) | O10 | 1.884(5) | O11 | 1.858(5) | | |
| O5 | 1.909(5) | | | | | | |
| Mean | 1.891 | Mean | 1.830 | Mean | 1.832 | Mean | 1.537 |
| P2-tetrahedron | | P3-tetrahedron | | Na1-octahedron | | Na2-octahedron | |
| P2–O8 | 1.529(5) | P3–O2 | 1.529(5) | Na1–O8 | 2.303(6) | Na2–O7 | 2.313(6) |
| O9 | 1.535(5) | O13 | 1.529(5) | O2 | 2.326(6) | O10 | 2.394(6) |
| O7 | 1.542(5) | O6 | 1.534(5) | O1 | 2.634(6) | O12 | 2.456(6) |
| O5 | 1.546(5) | O14 | 1.544(5) | O5 | 2.645(7) | O5 | 2.629(6) |
| | | | | O13 | 2.654(7) | O9 | 2.645(6) |
| | | | | O14 | 2.680(6) | O6 | 2.660(7) |
| Mean | 1.538 | Mean | 1.534 | Mean | 2.539 | Mean | 2.516 |

**Table 4.** Geometric characteristics of hydrogen bonds

| *D*–H··*A* | *D*–H, Å | H··*A*, Å | *D*··*A*, Å | Angle *D*–H··*A* |
|---|---|---|---|---|
| O3–H1···O11 | 0.66(9) | 2.63(9) | 3.238(6) | 155(11)° |
| O4–H2 ⋱ O1 | 0.69(9) | 2.29(9) | 2.925(7) | 154(12)° |
| O4–H2 ⋱ O8 | 0.69(9) | 2.50(9) | 3.031(6) | 136(11)° |

Note: *D* and *A* are the donor and the acceptor of a hydrogen bond.

**Table 5.** Bond–valence analysis

| Atom | Al1 | Al2 | Al3 | P1 | P2 | P3 | Na1 | Na2 | H1 | H2 | Σ | \|δ\| |
|---|---|---|---|---|---|---|---|---|---|---|---|---|
| O1 | 0.51 | | | 1.26 | | | 0.11 | | | 0.07 | 1.95 | 0.05 |
| O2 | 0.52 | | | | | 1.27 | 0.25 | | | | 2.04 | 0.04 |
| O3(OH) | 0.55 | 0.67 | | | | | | | 0.92 | | 2.14 | 0.14 |
| O4(OH) | 0.54 | | 0.60 | | | | | | | 0.89 | 2.03 | 0.03 |
| O5 | 0.50 | | | | 1.21 | | 0.10 | 0.11 | | | 1.92 | 0.08 |
| O6 | | 0.70 | | | | 1.25 | | 0.10 | | | 2.05 | 0.05 |
| O7 | | 0.65 | | | 1.22 | | | 0.25 | | | 2.12 | 0.12 |
| O8 | 0.52 | | | | 1.27 | | 0.26 | | | 0.04 | 2.09 | 0.09 |
| O9 | | 0.55 | | | 1.25 | | | 0.10 | | | 1.90 | 0.10 |
| O10 | | 0.53 | | 1.25 | | | | 0.20 | | | 1.98 | 0.02 |
| O11 | | | 0.57 | 1.28 | | | | 0.04 | 0.08 | | 1.97 | 0.03 |
| O12 | | | 0.59 | 1.19 | | | | 0.17 | | | 1.95 | 0.05 |
| O13 | | | 0.63 | | | 1.27 | 0.10 | | | | 2.00 | 0.00 |
| O14 | | | 0.68 | | | 1.22 | 0.10 | | | | 2.00 | 0.00 |
| Σ | 3.14 | 3.10 | 3.07 | 4.98 | 4.95 | 5.01 | 0.92 | 0.97 | | | | |

Note: The balance is calculated using the relationship $s_{ij} = \exp\left(\frac{R_I - R_{ij}}{b}\right)$, where $s_{ij}$ is the valence force of the *i*th cation that is transmitted to the *j*th anion; the bond length $R_I$ of unit valence for a particular cation–anion pair is tabulated as an empirical constant; and $R_{ij}$ is the experimental cation–anion length in a particular crystal structure; and $b = 0.37$.

The lengths of P–O bonds in three independent $PO_4$ tetrahedron complexes vary from 1.527 to 1.553 Å (the mean value is equal to 1.536 Å), which is quite usual for orthophosphate groups. Cation–oxygen interatomic spacings in sodium octahedra lie in the range 2.303–2.680 Å (the mean value is equal to 2.539 Å) and 2.313–2.660 Å (the mean value is equal to 2.516 Å) for Na1 and Na2, respectively. An additional oxygen atom lying at a distance of 2.955 Å completes an anion polyhedron around Na2 to a septahedron.

Hydrogen bonds in the structure are rather weak and (as is typical of inorganic compounds) asymmetric and essentially nonlinear (Table 4). The system of hydrogen bonds is complicated by the presence of bifurcated bonds between an O4 donor and two O1 and O8 acceptors.

Each Al1 octahedron shares two OH vertices with the neighboring Al2 and Al3 pentahedra, which form band-shape constructions parallel to the *c* axis in a unit cell (Fig. 1). The Al2 and Al3 polyhedra have no common vertices and interact via Al1 octahedra within bands consisting of $Al_3(OH)_2O_{12}$. Orthophosphate tetrahedra share all oxygen vertices with Al polyhedra, thereby uniting the bands described above into a frame-

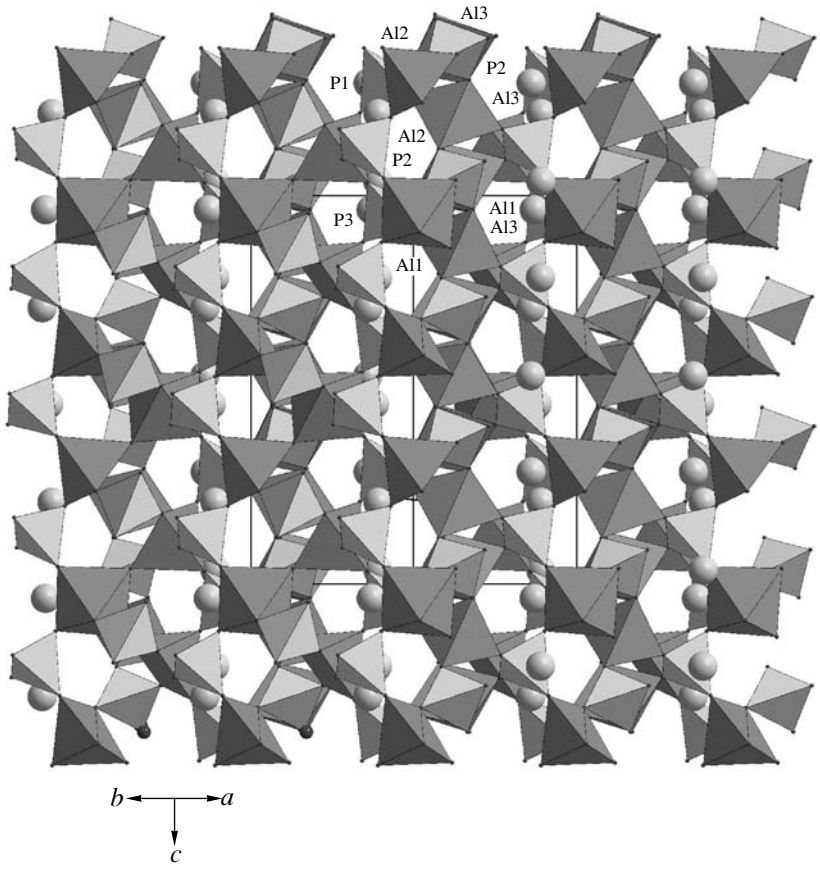


**Fig. 1.** Crystal structure of $Na_2\{Al_3(OH)_2[PO_4]_3\}$ in the projection along the diagonal of the *ab* plane. Bands that are parallel to the *c* axis and consist of vertex-linked Al polyhedra are clearly seen. Circles are Na atoms.

work construction (Fig. 2). Each of the P1 and P3 tetrahedra shares two vertices with the Al3 pentahedra and one vertex with the Al1 and Al2 polyhedra. A P2 tetrahedron has no common oxygen atoms with the Al3 pentahedra and shares two vertices with an Al1 octahedron and two vertices with an Al2 pentahedron. The resulting mixed-type framework $\{Al_3(OH)_4[PO_4]_3\}_{\infty\infty\infty}$ contains parallel [001] channels having tri- and octagonal cross sections. In the latter, $Na^+$ cations are situated (Fig. 3a).

In the framework of the Na–Al–P–O–H system, there are two natural minerals: wardite

$$Na\{Al_3(OH)_4(H_2O)_2[PO_4]_2\}\ [13]$$

and brazilianite

$$Na\{Al_3(OH)_4[PO_4]_2\}\ [14].$$

Their structures are based on mixed anion frameworks composed of Al octahedra and P tetrahedra. However, the topologies of the frameworks differ significantly from each other and from the topology of the structure of the new artificial phase described above. For example, the wardite structure includes layers consisting of

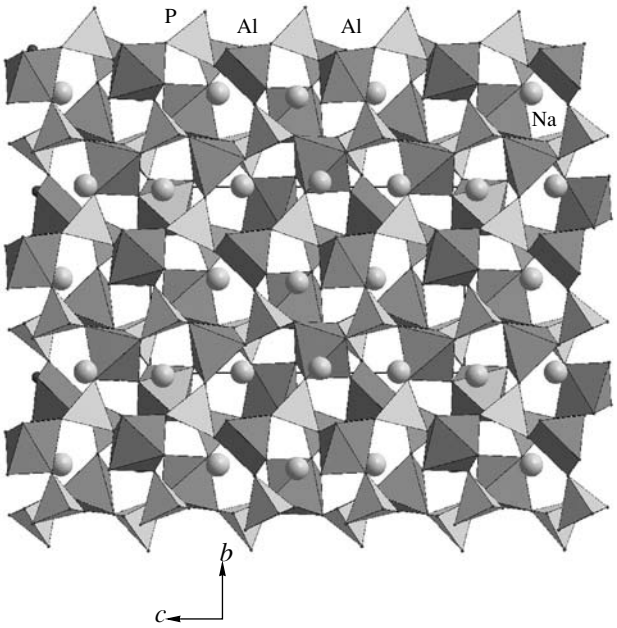


**Fig. 2.** Anion mixed-type framework consisting of Al and P polyhedra in the $Na_2\{Al_3(OH)_2[PO_4]_3\}$ structure (*yz* projection). Circles are cation "sodium" filling of the framework.

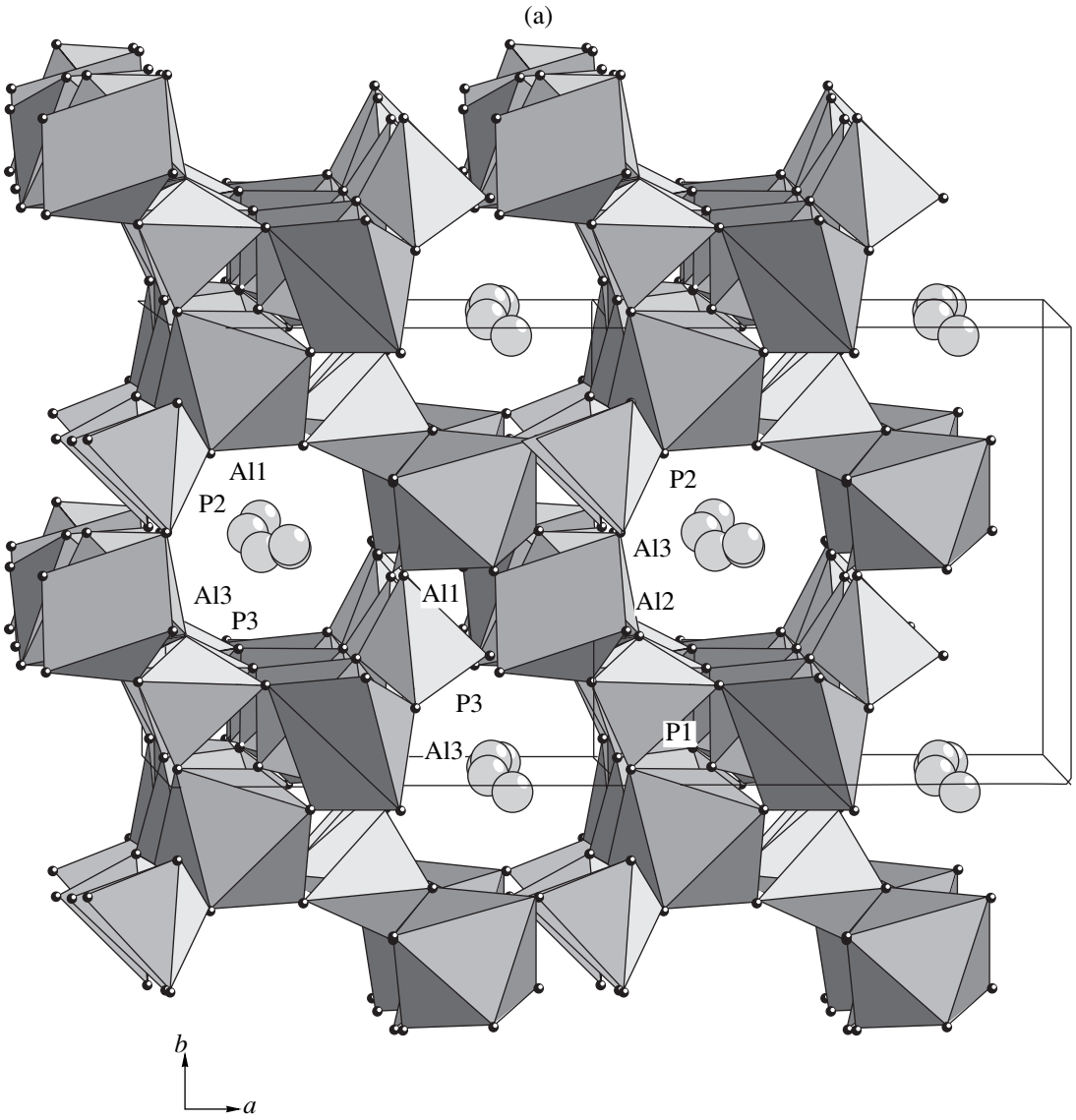


**Fig. 3.** Crystal structure of the (a) $Na_2\{Al_3(OH)_2[PO_4]_3\}$ synthetic phase and (b) $K\{Al_2F(H_2O)_4[PO_4]_2\}$ minyulite mineral. The view along the *c* axes of unit cells.

vertex-linked Al octahedra. These layers are united into a framework by orthophosphate octahedra and hydrogen bonds. In the crystal structure of brazilianite, chains composed of edge-linked Al octahedra are united to a framework by orthophosphate tetrahedron complexes. The voids in the microporous frameworks are filled with $Na^+$ cations.

The $Na_2\{Al_3(OH)_2[PO_4]_3\}$ aluminum phosphate, which we synthesized, is described by a new structure type. However, the topology of the Al- and P-based framework in the *ab* projection (up to the "absolute" configuration) is close to that of Al- and P-layers in the crystal structure of the pseudotetragonal minyulite mineral described by the formula

$$K\{Al_2F(H_2O)_4[PO_4]_2\}\ [15].$$

Pores of octagonal cross sections in layers parallel to the {001} plane contain $K^+$ cations, which are larger than $Na^+$ cations. An "elementary link" of mixed-type anion layers in the minyulite structure is an $\{Al_2F(H_2O)_4[PO_4]_2\}$ quasi-cluster (Fig. 3b) consisting of two Al octahedra and two P tetrahedra. In the *c*-axis direction, the layers are connected by hydrogen bonds. Similar quasi-clusters are present in the $Na_2\{Al_3(OH)_2[PO_4]_3\}$ structure. However, one octahedron is replaced by an Al pentahedron in the formation of these quasi-clusters. In the framework structure of sodium aluminum phosphate, these clusters are connected by common oxygen vertices with similar clusters not only in the *ab* plane (as in the minyulite structure), but also in the direction of the third crystallo-

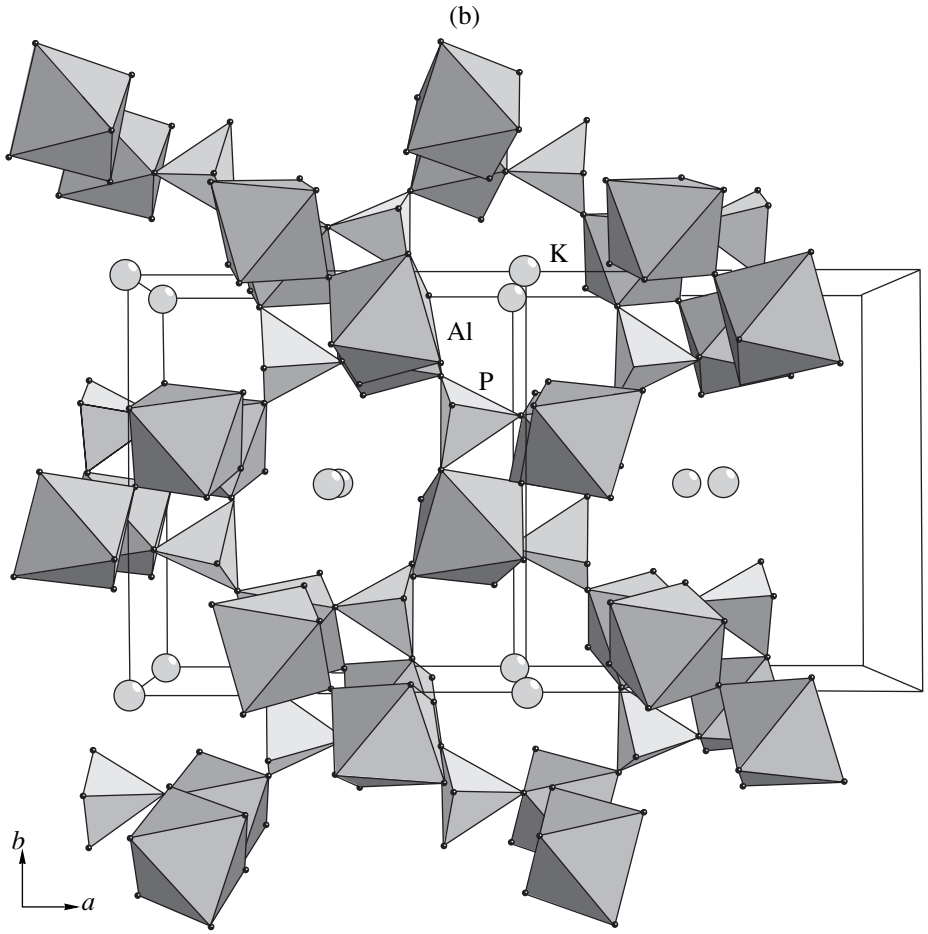


**Fig. 3.** (Contd.)

graphic axis. Since sodium aluminum phosphate was synthesized under soft hydrothermal conditions and its structure is topologically similar to the structure of minyulite, the probability of the existence of a natural mineral analogue of the new phase is quite high.

## ACKNOWLEDGMENTS

We are grateful to E.V. Guseva for assistance in the X-ray analysis of the samples. This work was supported by the Russian Foundation for Basic Research.

## REFERENCES

1. O. V. Yakubovich and M. S. Dadashov, Kristallografiya **33**, 848 (1988) [Sov. Phys. Crystallogr. **33**, 500 (1988)].
2. O. V. Yakubovich and O. K. Mel'nikov, Kristallografiya **34**, 62 (1989) [Sov. Phys. Crystallogr. **34**, 34 (1989)].
3. O. V. Yakubovich and V. I. Tarasov, Dokl. Akad. Nauk SSSR **303**, 1382 (1988) [Sov. Phys. Dokl. **33**, 880 (1988)].
4. X. H. Bu, P. Y. Feng, T. E. Gier, and G. D. Stucky, Zeolites **19**, 200 (1997).
5. W. T. A. Harrison, M. L. F. Phillips, and X. H. Bu, Microporous Mesoporous Mater. **39**, 359 (2000).
6. K. O. Koneshaug, H. Fjellvag, and K. F. Lillerud, Microporous Mesoporous Mater. **39**, 341 (2000).
7. G. M. Sheldrick, *SHELXS-97. Program for the Solution of Crystal Structures* (Göttingen Univ., Göttingen, 1997).
8. G. M. Sheldrick, *SHELXL-97. Program for the Refinement of Crystal Structures from Diffraction Data* (Göttingen Univ., Göttingen, 1997).
9. *International Tables of Crystallography*, Ed. by T. Hahn (Kluwer, Dordrecht, 1995), Vol. A.
10. H. D. Flack, Acta Crystallogr. A **39**, 876 (1983).
11. V. S. Urusov and I. P. Orlov, Kristallografiya **44**, 736 (1999) [Crystallogr. Rep. **44**, 686 (1999)].
12. I. D. Brown, Acta Crystallogr. A **32**, 24 (1976).
13. L. Fanfani, A. Nunzi, and P. F. Zanazzi, Miner. Mag. **37**, 598 (1970).
14. B. M. Gatehouse and B. K. Miskin, Acta Crystallogr. B **30**, 1311 (1974).
15. A. R. Kampf, Am. Mineral. **62**, 256 (1977).

*Translated by Yu. Vishnyakov*

*Doklady Physics, Vol. 48, No. 5, 2003, pp. 216–220. Translated from Doklady Akademii Nauk, Vol. 390, No. 2, 2003, pp. 178–182.*


**PHYSICS**

# Structurally Unstable Magnetic Configurations in the Three-Dimensional Geometry

**Corresponding Member of the RAS D. P. Kostomarov*, I. N. Inovenkov*, E. Yu. Echkina*, A. V. Leonenko*, V. V. Pichushkin*, F. Pegoraro**, and S. V. Bulanov*****

Received December 24, 2002

## 1. INTRODUCTION

Magnetic fields play an important role in the formation and evolution of structures peculiar to space and laboratory plasma. In the evolution process of these structures, rapid dissociation of magnetic energy with its transformation into that of accelerated particles and of radiation, as well as into plasma energy, is observed. Examples of these phenomena are solar bursts, substorms in the Earth's magnetosphere, and disruptive instabilities in tokamak plasmas, the main reason of such instabilities being a physical process known as reconnection of magnetic-field lines [1–4]. The magnetic reconnection occurs in the vicinity of critical points in magnetic configurations. It is accompanied by a change in topology of the magnetic field and leads to the formation of singular distributions of the electric current in plasma (current sheets) and shock waves.

The problem of reconnection of magnetic-field lines is closely related to that of the structural stability of vector fields. It is well known that the magnetic-field topology is described in terms of a phase space of the corresponding dynamical system. Therefore, results obtained in the theory of dynamical systems can be used to analyze the structural stability of magnetic fields. The general problem of the structural stability was comprehensively discussed in [5]. It was concluded there that a system is structurally stable if, for small perturbations of an initial configuration, the resulting system is equivalent to the original one. Otherwise, the system is structurally unstable. In particular, fields with degenerate critical points, i.e., with points in the vicinity of which the eigenvalues of the linearized problem vanish, correspond to structurally unstable vector fields.

Recently, magnetic reconnection in structurally unstable magnetic fields has attracted much attention owing also to the fact that these fields exhibit important features of magnetic configurations in tokamaks with the inverse shear [6]. These are the configurations that make it possible to attain a more efficient plasma confinement. Thus, the analysis of magnetic reconnection in structurally unstable fields acquires a practical importance in studies of both stability and transport processes in thermonuclear plasma with magnetic confinement.

As was mentioned above, magnetic reconnection changes the magnetic-field topology. It is natural to assume that, as a result of this situation, structurally unstable magnetic configurations transform into structurally stable ones. However, the analysis of the structural stability in the case of the magnetic reconnection turns out to be more complicated than in the case of the structural stability of only one vector field depending on a parameter. This is explained by the fact that the magnetic reconnection in high-conductivity plasma is determined by the nonlinear interaction of two vector fields, namely, the magnetic field and the plasma velocity field. The analytic description of such nonlinearly evolving systems under conditions of multidimensional geometry encounters essential difficulties. Therefore, the adequate description of these processes requires the application of numerical-simulation methods.

Until the present time, the theory of reconnection in structurally unstable configurations was considered only for one-dimensional and two-dimensional systems [7–9]. The goal of the present paper is the study of the magnetic reconnection in the process of a passage of structurally unstable three-dimensional magnetic configurations into structurally stable ones.

Our analysis is developed in the following manner. In Section 2, analytic expressions describing the shape of the magnetic field in the vicinities of degenerate high-order critical points are given. In the next section, the results of a numerical magnetohydrodynamic (MHD) simulation are presented. In the concluding section, the basic results of the analysis are formulated.

* *Moscow State University, Vorob'evy gory, Moscow, 118899 Russia*

** *Physical Faculty and National Institute of Matter Physics, Pisa University, Italy*

*** *Institute of General Physics, Russian Academy of Sciences, ul. Vavilova 38, Moscow, 119991 Russia*

*e-mail: ino@cs.lnsu.su*

1028-3358/03/4805-0216$24.00 

## 2. MAGNETIC-FIELD STRUCTURE IN THE VICINITY OF A DEGENERATE CRITICAL POINT

In the vicinity of a critical point, in which the magnetic field vanishes, this field can be represented in the form of the following power expansion:

$$B_i = B_{ij}x_j + \frac{1}{2}B_{ijk}x_jx_k + K. \quad (1)$$

Here, $B_{ij} = \left.\frac{\partial B_i}{\partial x_j}\right|_{x=0}$, $B_{ijk} = \left.\frac{\partial^2 B_i}{\partial x_j \partial x_k}\right|_{x=0}$, and $K$ is a residual term. If the magnetic field is potential, i.e., is produced by sources situated far from the critical point, then the field can be represented in the form of a gradient of a scalar potential $F(x, y, z)$: $\mathbf{B} = \mathrm{grad}F$.

Locally, the topology of a magnetic field is determined by the first nonzero term on the right-hand side of expression (1). We now suppose that the matrix $B_{ij}$ is not the zero matrix. For a potential field ($\mathrm{curl}\mathbf{B} = 0$), this matrix can be represented in the diagonal form with the zero trace:

$$B_{ij} = \mathrm{diag}\{a^{(2)}, b^{(2)}, -(a^{(2)} + b^{(2)})\}.$$

In this expression, the superscript (2) describes the order of a singular point. The scalar potential of the magnetic field has the form

$$F^{(2)}(x, y, z) = \frac{1}{2}(a^{(a)}(x^2 - z^2) + b^{(2)}(y^2 - z^2)). \quad (2)$$

The magnetic configuration is determined by the parameters $a^{(2)}$, $b^{(2)}$ and corresponds to the zero point. The magnetic field related to this potential function has a critical (singular) field line connecting the zero point to the infinitely remote point. This field also has a singular (separatrix) plane passing through the zero point. By virtue of the condition $\mathrm{div}\mathbf{B} = 0$, the sum of eigenvalues of the matrix $B_{ij}$ is zero, whereas $l_1 = a^{(2)}$, $l_2 = b^{(2)}$, and $l_3 = -(a^{(2)} + b^{(2)})$. As follows from expression (2), in this case, the magnetic field may be represented as a superposition of two two-dimensional magnetic fields with the potentials $\frac{1}{2}a^{(2)}(x^2 - z^2)$ and $\frac{1}{2}b^{(2)}(y^2 - z^2)$. The potential function describing the two-dimensional field is the real-valued part of the complex potential $W^{(2)}(h) = F - iA$, which, in turn, has the form of the quadratic function $W^{(2)}(h) = \frac{1}{2}a^{(2)}h^2$. For the first and second terms in formula (2), the complex variables are in this case $h = x + iz$ and $g = y + iz$, respectively.

In the general case, the critical point of field (2) is nondegenerate. To provide the degeneration of the critical point, one of the eigenvalues vanishes. Let $b^{(2)} = 0$, then the potential function is $F^{(2)} = \frac{1}{2}a^{(2)}(x^2 - z^2)$. This is a magnetic field with the $X$-type zero field line located in a plane parallel to the $OY$ axis. The $X$-type field line is a zero line of the magnetic field. Along this line and on it, two separatrix surfaces and the magnetic field intensity, respectively, vanish. While passing to the structurally stable field, the zero point disappears and a second separatrix plane arises.

For the zero matrix $B_{ij}$, the next term on the right-hand side of expression (1) becomes the defining one, the potential function

$$F^{(3)}(x, y, z) = \frac{(a^{(3)} + b^{(3)})}{3}z^3 - z(a^{(3)}x^2 + b^{(3)}y^2) + \frac{(c^{(3)} + d^{(3)})}{3}x^3 - x(c^{(3)}y^2 + d^{(3)}z^2) + \frac{(e^{(3)} + f^{(3)})}{3}y^3 - y(e^{(3)}z^2 + f^{(3)}x^2) \quad (3)$$

corresponding to this term. At the critical point $x = 0$, all elements of the matrix $B_{ij}$ vanish, and the magnetic-field configuration is then determined by the parameters $a^{(3)}$, $b^{(3)}$, $c^{(3)}$, $d^{(3)}$, $e^{(3)}$, and $f^{(3)}$. In this case, the magnetic field, in itself, is a superposition of two-dimensional magnetic fields, each of them determining the zero line of the third order. The characteristic shape for one of the coordinate-dependent two-dimensional magnetic fields is given by the potential function $F^{(3)}(x, y) = c^{(3)}\left(\frac{x^3}{3} - xy^2\right)$. As in the preceding case, the potential function is equal to the real-valued component of the complex potential $W^{(3)}(z) = F - iA$, which depends on the complex variable $z = x + iy$ in the following way: $W^{(3)}(z) = \frac{c^{(3)}z^3}{3}$. We now consider a surface given by the equation $F^{(3)} = 0$ for the following values of the parameters:

$$a^{(3)} = 1, \quad b^{(3)} = 0, \quad c^{(3)} = 0, \quad d^{(3)} = 1,$$
$$e^{(3)} = -1, \quad f^{(3)} = 0.$$

The magnetic field defined by this equation is of certain interest, because it possesses only one critical field line connecting the zero point to an infinitely remote point. It also has two separatrix planes passing through the zero point. It is worth noting that the magnetic field acquires a more complicated form in the case of a special relation between the parameters $a^{(3)}$, $f^{(3)}$, on one hand, and the residual term $K$ of the power expansion, on the other. In particular, a combination is possible in which there are critical field lines and no separatrix surface. In this case, by the proper choice of parameter values and by a linear transformation of coordinates, relationship (3) can be reduced to the expression $F^{(3)}(x, y, z) = g^{(3)}xy$.

In the two-dimensional case, the peculiar shape of the magnetic field in the vicinity of a critical point of the third order is determined by the potential function

$$F^{(3)}(x, y) = f^{(3)}\left(\frac{y^3}{3} - yx^2\right). \quad (4)$$

The magnetic configuration contains three separatrices intersecting each other at the zero point. Perturbations of the magnetic field, which were caused by the excitation of a low electric current by potential magnetic field (2), as well as by the external homogeneous magnetic field, result in either a bifurcation of the degenerate singular point or its disappearance. A comprehensive analysis of the bifurcations in magnetic field (4) can be found in the book by Postone and Stewart [10].

In the three-dimensional case, small perturbations caused by electric current, as well as by terms of a lower order, including a homogeneous magnetic field, lead to a change in the magnetic-field topology. For example, the superposition of a homogeneous field or a quadrupole field and a field of form (3) leads to the appearance of a structurally stable configuration possessing zero points of a lower order. However, from the standpoint of ideal magnetohydrodynamics, the transformation of a structurally unstable configuration into a structurally stable one is impossible, since this transformation must be accompanied by a change in the magnetic-field topology. In order to describe such a transformation, it is necessary to allow for dissipative effects.

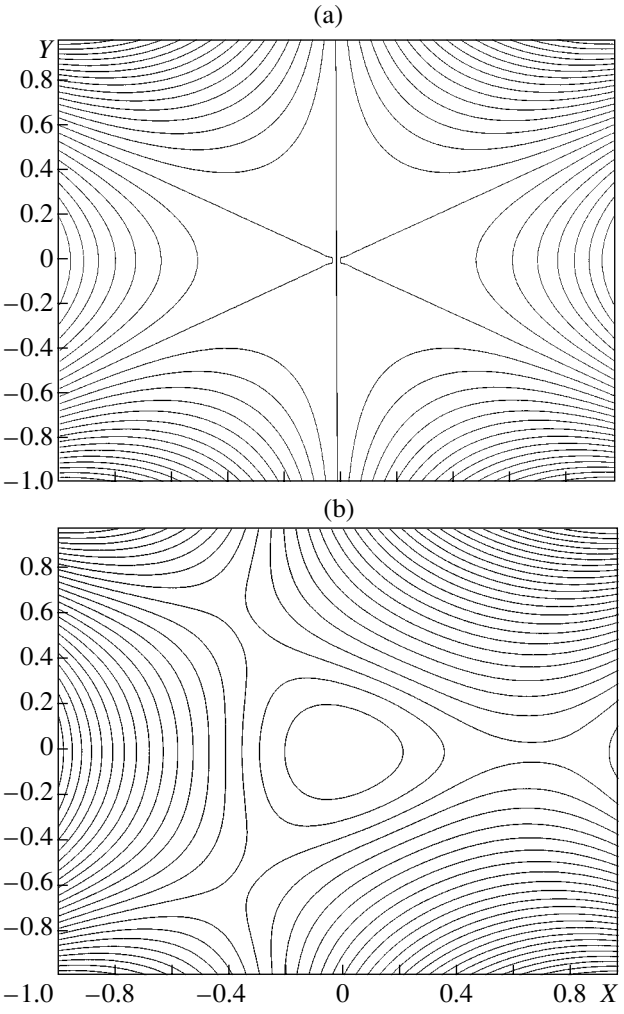


**Fig. 1.** Magnetic-field lines at the times (a) $t = 0$ and (b) $t = 4$ (two-dimensional case).

## 3. MHD SIMULATION OF TRANSFORMATION OF A STRUCTURALLY UNSTABLE MAGNETIC CONFIGURATION INTO A STRUCTURALLY STABLE ONE

The mixed problem for MHD equations, whose solution describes a self-consistent evolution of both plasma and the magnetic field in the vicinity of the initial critical point, was solved numerically. It was assumed that, at the initial time, a plasma with a uniform density and pressure is in the quiescent state in a two-dimensional potential field of type (4) (in the first variant of the calculations) or in a three-dimensional potential field of the type (3) (in the second variant of the calculations). The set of MHD equations used and boundary conditions were described in detail in [11, 12]. There, a magnetic reconnection in fields with other initial structures was simulated.

**Restructuring the magnetic-field structure in the vicinity of a two-dimensional third-order zero point.** The results of the third calculation variant show the evolution of initial two-dimensional configuration (4) under the action of azimuth-symmetric perturbations that excited in plasma an electric current of a finite intensity.

Figure 1a demonstrates the distribution of magnetic-field lines at the initial moment of time. Hereinafter, the time is measured in Alfven periods [11].

The magnetic field corresponding to this configuration is conveniently represented in the complex form: $\mathbf{B} = B_x - iB_y$. In this case, the dependence of $\mathbf{B}$ on the complex variable $z = x + iy$ is of the form

$$\mathbf{B} = C(z^3 - l^3)^{1/2}, \quad (5)$$

where $l$ is the dimensionless length of the current sheet. Analytical and numerical study of the self-consistent plasma evolution in magnetic field (5) shows that there are three cuts (current sheets) with the length $l$ in the plane of the complex variable $z$. Each current sheet is directed along one of the rays $j = 0$, $\frac{2}{3}\pi$, or $\frac{4}{3}\pi$. The magnetic field vanishes at the ends of the current sheets, whereas at the center, $z = 0$, both the magnetic field and the electric-current density vanish. Such behavior of the magnetic field is intrinsic to the transient stage of the development process. The duration of this stage is shorter than one Alfven period.

In a time on the order of the Alfven period, a current region of finite dimensions is formed, which is bounded by three magnetic-field separatrices. In the corners of these region, three zero *X*-type magnetic-field lines are situated, whereas, in its center, an O-type zero line is formed [1]. In the corners of the current region, the current sheets are located. They are similar to those that appear in the vicinity of the *X*-type zero field line. Plasma flows around the current region moving along the magnetic separatrices at its boundaries (Fig. 1b). In the neighborhood of the current sheets, shock waves arise. These magnetic configurations can be compared with the triangular magnetic "islands" that were observed in [13], where the double tearing mode in a tokamak plasma with the inverse magnetic shear was studied.

**Restructuring the magnetic-field structure in the vicinity of a three-dimensional zero point of the third order.** The boundary conditions for the set of MHD equations correspond to the excitation of the electric current directed along the *OZ* axis, similar to the case analyzed in [12]. We have considered initial three-dimensional magnetic fields of the form

$$\mathbf{B} = \{x^2 - z^2 - 2xz, z^2 - y^2, z^2 - x^2 + 2z(y - x)\}, \quad (6)$$

$$\mathbf{B} = \{x^2 - z^2 - 2x(y + z), y^2 - x^2, z^2 - x^2 - 2zx\}, \quad (7)$$

$$\mathbf{B} = \{x^2 - z^2 + 2xy, x^2 - y^2 - 2yz, z^2 - y^2 - 2zx\}. \quad (8)$$

As an example, we present the results of the numerical study for the transformation of a structurally unstable configuration into a structurally stable one for magnetic field (8).

In Fig. 2a, an initial magnetic configuration that corresponds to this magnetic field is shown. As a result of exciting the electric current at the boundary of the calculation region, the initial magnetic configuration transforms into a structurally stable one (Fig. 2b). We can see that splitting of the third-order zero point into two three-dimensional zero points of the second order has occurred. In the figure, formation of the separatrix surface separating these points is clearly seen. Localization of the electric current in the vicinity of the zero points does occur.

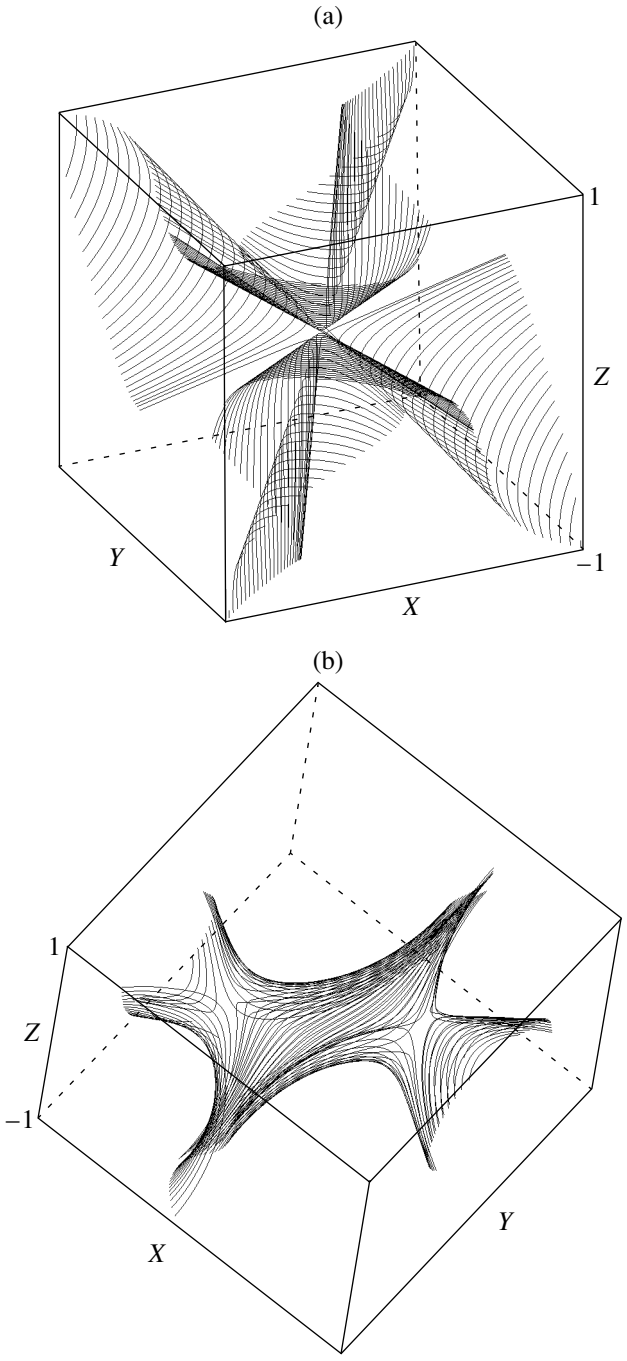


**Fig. 2.** Magnetic-field lines at the times (a) $t = 0$ and (b) $t = 15$ (three-dimensional case).

## 4. CONCLUSIONS

Thus, we have managed to show that the potential magnetic field in the vicinity of a critical point of the third order is determined by 6 parameters. Since a critical point of the third (and higher) order is degenerate, the problem of the evolution of a structurally unstable magnetic configuration into a structurally stable one acquires a principal importance.

In the framework of the plasma model based on the use of ideal magnetic hydrodynamics, the condition of freezing-in the magnetic field into plasma is valid. By virtue of this fact, the topology of the magnetic field must be conserved and the transformation of a structurally unstable magnetic configuration into structurally stable one turns out to be impossible. Therefore, in order to describe this transformation, it is necessary to take into account dissipative effects and to use numerical methods for detailed simulation of magnetic-reconnection processes.

In this paper, we have presented the results of a numerical MHD simulation for processes of the pas-

sage from a structurally unstable magnetic configuration into a structurally stable one in conditions of two-dimensional and three-dimensional geometry. The structure transformation of the initial structurally unstable magnetic field into a structurally stable one is accompanied by the reconnection of magnetic-field lines in plasma with the formation of current sheets near magnetic separatrices. This fact was discovered previously when investigating the reconnection in structurally stable systems. At the same time, formation of current regions with finite dimensions takes place, which demonstrates novel features of the magnetic-reconnection phenomenon.

## REFERENCES

1. S. I. Syrovatskiĭ, Zh. Éksp. Teor. Fiz. **60**, 1727 (1971) [Sov. Phys. JETP **33**, 933 (1971)].
2. V. V. Kadomtsev, Fiz. Plazmy **1**, 710 (1975) [Sov. J. Plasma Phys. **1**, 389 (1975)].
3. D. Biskamp, *Nonlinear Magnetohydrodynamics* (Cambridge Univ. Press, Cambridge, 1993).
4. V. S. Berezinskiĭ, S. V. Bulanov, V. L. Ginzburg, *et al.*, *Astrophysics of Cosmic Rays* (North Holland, Amsterdam, 1990), pp. 534–537.
5. V. I. Arnol'd and Yu. S. Il'yashenko, *Ordinary Differential Equations* (VINITI, Moscow, 1985).
6. P. J. Morrison, Phys. Plasmas **7**, 2279 (2000).
7. S. V. Bulanov, V. V. Pichushkin, and K. Shindler, Fiz. Plazmy **22**, 979 (1996) [Plasma Phys. Rep. **22**, 885 (1996)].
8. S. V. Bulanov, E. Yu. Echkina, I. N. Inovenkov, *et al.*, Phys. Plasmas **6**, 802 (1999).
9. N. A. Bobrova, S. V. Bulanov, J. I. Sakai, and D. Sugiyama, Phys. Plasmas **8**, 759 (2001).
10. T. Poston and I. Stewart, *Catastrophe Theory and Its Applications* (Pitman, London, 1978; Mir, Moscow, 1981).
11. K. V. Brushlinskiĭ, A. M. Zaborov, and S. I. Syrovatskiĭ, Fiz. Plazmy **6**, 297 (1980) [Sov. J. Plasma Phys. **6**, 165 (1980)].
12. S. V. Bulanov, E. Yu. Echkina, I. N. Inovenkov, and F. Pegoraro, Phys. Plasmas **9**, 38 (2002).
13. Y. Ishii, M. Azumi, and Y. Kishimoto, Phys. Rev. Lett. **89**, 205002 (2002).

*Translated by G. Merzon*

*Doklady Physics, Vol. 48, No. 5, 2003, pp. 221–223. Translated from Doklady Akademii Nauk, Vol. 390, No. 2, 2003, pp. 183–186.*


**TECHNICAL PHYSICS**

# Features of the Film Boiling Regime in Organic Liquids

**S. A. Zhukov, V. A. Rafeev, S. Yu. Afanas'ev, S. B. Echmaev, and B. L. Korsunskiĭ**

Presented by Academician A.I. Leont'ev November 26, 2002

Received November 26, 2002

It is thought that the theory of film boiling in liquids is well developed on the basis of an assumed analogy with the film-condensation process [1, 2]. However, experimental data corroborating the theoretical representations are predominantly obtained for cryogenic or easily boiling organic liquids such as carbon tetrachloride, methanol, ethanol, isopropanol, gasoline, etc. The possibility of the existence of special features of film boiling in organic liquids was never discussed.

We studied film boiling in organic liquids on the basis of the available data indicating that the heat exchange in this regime was accompanied by pronounced signs of chemical reactions. The purpose of this study was to determine the degree of the effect of chemical reactions proceeding in a film on the heat-exchange processes.

Applying the heated-filament method, supplemented by various methods of chemical analysis, we used a Pt wire 0.1 mm in diameter and 4 cm in length as a heater. Current in the heater was constant ($I$ = const). The parameters were stabilized by a special fast analog control unit. Current and voltage were measured by 12-digit analog-to-digital converters (ADCs) connected with a computer and were used to calculate the working temperature of the heater and the released power. The ADC sampling frequency was 5 kHz.

The film regime was studied in a hermetic quartz reactor, which contained 15 ml of the liquid under investigation and was equipped with a dephlegmator and a reflux condenser. The liquid-bulk temperature, product-condensation temperature, change in the volume of the liquid, and the release rate and volume of permanent gaseous products were measured in the experiments. The volume of gas released in boiling was measured with an accuracy of 0.1 $mm^3$. The liquid-bulk temperature was controlled by a liquid thermostat.

The products were analyzed by the following methods: chromatography, nuclear magnetic resonance, mass spectrometry, chromatographic mass spectrometry, and analytical chemistry methods. The visual information was recorded by a digital video camera with a magnification of 10–25×.

As working liquids, we used carbon tetrachloride and various alcohols ($C_1$–$C_5$). The purity degree of original liquids was monitored by chromatography and IR spectroscopy.

Intense steady gas emission was observed in the film-boiling regime for all liquids under investigation. This emission in different substances became noticeable for different heater temperatures. For example, the indications of the decomposition of carbon tetrachloride appear already at 550–600°C, whereas the decomposition of ethanol becomes noticeable only at temperatures above 900°C. Figure 1 shows the time dependences of the volume of gas released for various heater temperatures in methanol, and Fig. 2 displays the summary data for gas emission in four liquids.

Organic liquids have a low heat of vaporization, and the transition to the film regime in them is not accompanied by catastrophic superheating of the heater even at low liquid temperatures. For this reason, they are often used as model systems to investigate mechanisms of the underheated film regime. It is well known that film thickness decreases with an increase in underheat-

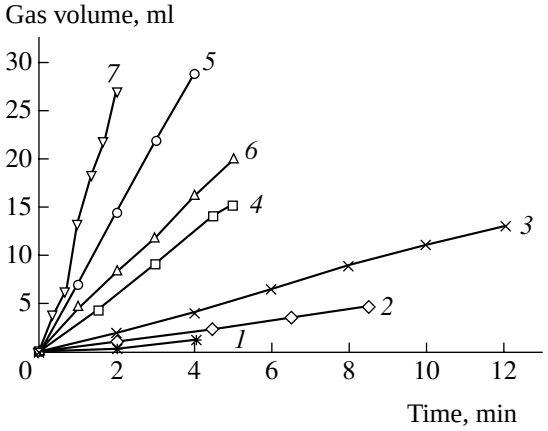


**Fig. 1.** Time dependence of the emitted-gas volume for methanol, $T_l = T_{sat}$, and heater temperatures (*1*) 910, (*2*) 950, (*3*) 1000, (*4*) 1050, (*5*) 1065, (*6*) 1090, and (*7*) 1130°C.

*Institute of Problems of Chemical Physics, Russian Academy of Sciences, Chernogolovka, Moscow oblast, 142432 Russia*

1028-3358/03/4805-0221$24.00 © 2003 MAIK "Nauka/Interperiodica"

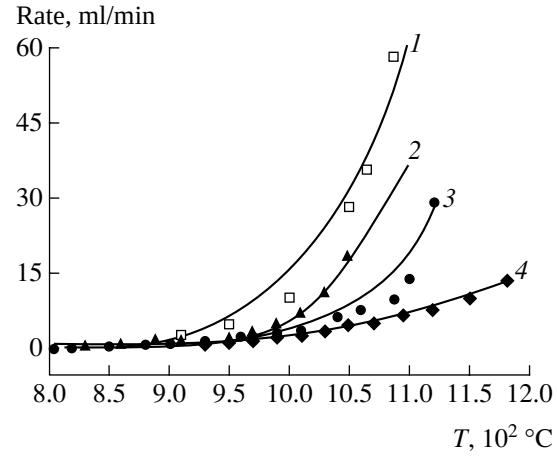


**Fig. 2.** Gas-emission rate vs. heater temperature in (*1*) methanol, (*2*) *t*-butanol, (*3*) isobutanol, and (*4*) ethanol for $T_l = T_{sat}$.

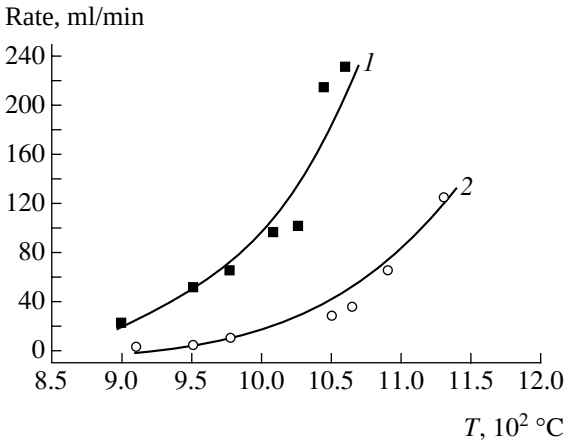


**Fig. 3.** Gas-emission rate vs. heater temperature in methanol for $T_l$ = (*1*) –20 and (*2*) 75°C.

ing and, thus, temperature gradients inside the film increase. Chemical transformations, which are extremely sensitive to the temperature regime, cannot be unchanged under these variations. This conclusion is corroborated in Fig. 3, where the specific gas-emission rate is shown for two temperatures of the liquid.

Our investigations of the kinetics and mechanisms of chemical reactions proceeding in the vapor cavern provide the following general conclusions.

The composition of gas released in the film regime is determined by all basic parameters of the process, such as the heater temperature, underheating degree, purity of liquid, and heater material. For lower alcohols, where the bulk temperature is sustained near the saturation temperature, the main products are hydrogen, methane, ethane, ethylene, and carbon oxide. As underheating increases, the number of components decreases. The primary components are now simple substances—hydrogen and carbon oxide. For higher alcohols, the composition of the gas phase is more complicated. The chemical analysis reveals significant quantities of unsaturated compounds. More complicated, often exotic substances are formed in addition to typical pyrolysis products, which testifies to secondary synthesis reactions, whose components are likely radicals formed at the primary stages. The liquid-phase composition also varies. This phase accumulates such compounds as aldehydes (primarily, formaldehyde), various alcohols, and ketones. In carbon tetrachloride, the major fraction of the product remaining in the liquid is represented by hexachlorethane.

Thus, the experiments corroborate that the chemical composition of organic liquids is substantially modified in film boiling, and the boiling is accompanied by gas emission of the chemical nature. Undoubtedly, these features significantly affect film-boiling mechanisms.

We observed film boiling within a very wide interval of underheating. Under these conditions, heater-temperature fluctuations increase significantly in all liquids being investigated, which is manifested with an increase in underheating. This effect is pronounced in carbon tetrachloride. Furthermore, in this system, heater-temperature fluctuations are easily visible. As underheating increases, spots darker than the remaining surface appear periodically on the heater surface heated up to a temperature of 700–1200°C. Their size depends only slightly on the underheating degree and heater temperature.

Video recordings show that local temperature oscillations are periodic and associated with the growth and separation of a bubble from the heater surface.

For further investigations, we use the procedure proposed in [3] for studying critical phenomena accompanying boiling of a metastable liquid. The essence of this procedure is in using a heater whose length is comparable with the characteristic size of the process under investigation. In this case, the system is concentrated rather than distributed. Both the advantages and disadvantages of this procedure are evident. An advantage is the insensitivity or low sensitivity of heat exchange on such a heater to spatial inhomogeneities. For this reason, we can investigate the regime in detail. A disadvantage of this procedure is the impossibility of directly measuring temperature by using ohmic resistance.

Figure 4 displays thermograms obtained for a 2-mm-long heater in carbon tetrachloride when $I$ = const. Being estimated from the luminous exitance, the temperature in the glow maximum was equal to about 900–1000°C depending on experimental conditions. At the same time, the heater remained dark at the minimum-temperature point. This fact means that its temperature was below 650°C. Thus, the amplitude of observed oscillations is equal to 350–450°C. For slight underheating, the oscillation frequency increased with decreasing liquid temperature but then became constant for $T_h - T_l$ = 30–40°C.

The synchronization of the video recording of the process occurring on an individual domain with ther-

mograms leads us to the conclusion that the oscillation process involved several repeating stages. At the first stage, a bubble separates and leaves a thin (~10 μm) vapor–gas layer symmetrically covering the heater surface. Immediately after the bubble separation, the film thickness increases, which is accompanied by an increase in the heater temperature. The further growth of the bubble leads to a significant transformation in its shape. Its upper section extends upwards rising over the heater, while a base length decreases. The major temperature drop is associated with the development of this process. Attaining a certain size, the bubble separates. At the moment of separation, the heater temperature is minimal. Further, the first stage begins again, and the process is repeated.

We try to construct a qualitative model explaining the mechanism of self-oscillations of the surface temperature on the basis of the data obtained.

Let the heater be surrounded by a spherically symmetric vapor film at the initial time. We assume that heat is transferred from the heater to the liquid phase due to the thermal conductivity through the vapor layer and is entirely spent on evaporating the liquid. As the film thickness increases, the heater temperature increases because the heat-removal conditions deteriorate. When a certain temperature is reached, a chemical reaction accompanied by gas emission becomes noticeable. This leads to an increase in the diameter of the vapor film and, respectively, in the heater temperature, which further increases the reaction rate. When the bubble grows so that the contribution of the buoyancy force becomes considerable, the film extends upwards. In addition, its lower boundary further approaches the heated surface, whereas its upper section recedes from it. As follows from experimental data, the thickness of the lower section of the film is equal to about 10 μm, whereas the film dome is at a distance of about 2 mm from the heated surface at this moment of time. Under these conditions, all the vapor is exceptionally formed in the lower section of the heater and is transferred into the upper section of the film through a vapor gap, whose size is of the same order of magnitude as the minimum thickness of the vapor coat. The estimates made in this simplest of models show that the amount of liquid evaporated in the lower section of the film is sufficient for the vapor velocity in the narrowest section of the gap to exceed tens or even hundreds of meters per second.

Forced convection with such a high velocity of motion has to abruptly increase the heat transfer coefficient and, thus, to decrease the heater temperature. Passing to the upper section of the dome, most of the vapor can be condensed on the cool interface surface. However, the domain grows due to the accumulation of gaseous reaction products. When the bubble diameter exceeds the separation diameter, the bubble separates from the surface, leaving a thin vapor–gas layer on it, and the process is repeated.

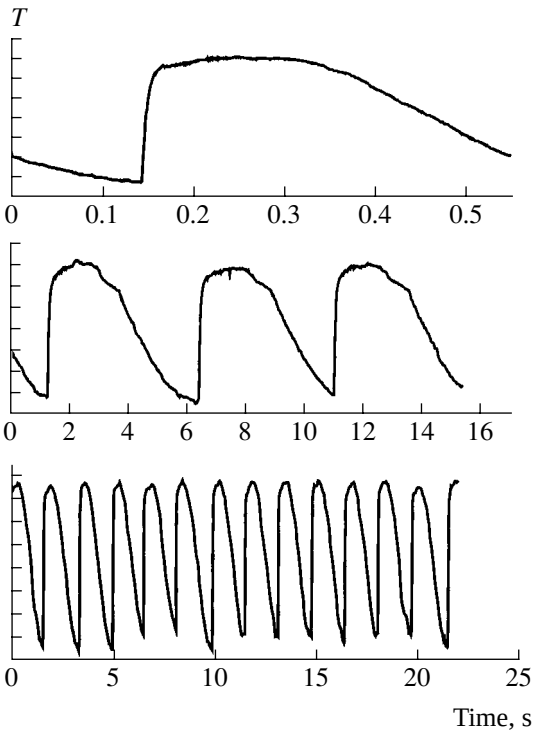


**Fig. 4.** Thermograms of self-oscillation heat transfer in the film-boiling regime in $CCl_4$ on a 2-mm-long individual (elementary) domain for $T_{CCl_4} = -10°C$.

Thus, our experiments confirm that the film-boiling mechanism in organic liquids is primarily determined by chemical reactions proceeding in the film. The self-oscillation regime of the film boiling has been discovered.

## ACKNOWLEDGMENTS

This work was supported by the Russian Foundation for Basic Research, project nos. 01-02-1723 and 01-03-32075.

## REFERENCES

1. L. A. Bromley, Chem. Eng. Prog. **46** (2), 221 (1950).
2. D. P. Jordan, in *Advances in Heat Transfer* (Academic, New York, 1968; Mir, Moscow, 1971), pp. 68–143.
3. S. Yu. Afanas'ev, S. A. Zhukov, B. L. Korsunskiĭ, *et al.*, Dokl. Akad. Nauk **372**, 337 (2000).
4. S. Yu. Afanas'ev, S. A. Zhukov, and S. B. Echmaev, Teplofiz. Vys. Temp. **34** (5), 712 (1996).

*Translated by V. Bukhanov*

*Doklady Physics, Vol. 48, No. 5, 2003, pp. 224–227. Translated from Doklady Akademii Nauk, Vol. 390, No. 2, 2003, pp. 187–191.*


**TECHNICAL PHYSICS**

# Description of Electrorheological Fluids

**V. É. Zgaevskiĭ**

Presented by Academician A.E. Shilov December 10, 2002

Received December 10, 2002

Electrorheological fluids are extensively used in industry and technology due to their unique ability to considerably change their effective viscosity in an electric field. Typical electrorheological fluids have low permittivity and contain a given concentration of fine dielectric particles (a dispersed phase) of high permittivity.

Extensive use of electrorheological fluids has stimulated their theoretical and experimental investigation. The rheological properties of electrorheological fluids were recently studied by various methods in numerous theoretical works. A phenomenological approach is based on the Bingham equation and on its modifications such as the Cason equation [1] or the Shul'man equation [2], which involves fractional-powers terms. A continuous approach was developed in [3]. Motion of particle in an electrorheological fluid in the presence of both an electric field and velocity gradients has been extensively simulated by numerical methods [4].

Most theoretical works are based on models of electrorheological fluids. For example, models involving filler-particle chains, which are directed along the electric field when velocity gradients are absent, were used in [5–7].

In this paper, the rheological properties of electrorheological fluids are described in a three-dimensional ordered many-particle model of a composite (crystal model) [8] rather than in the model of one-dimensional chains of particles.

Suspension of dielectric particles in a viscous fluid is modeled by identical rigid particles, which are located in sites of a given-symmetry lattice in the absence of an electric field and velocity gradients. The permittivities of the particles ($\varepsilon_p$) and fluid ($\varepsilon_l$) differ from each other. The electrorheological fluid is situated in a uniform electric field $\mathbf{E}$ with components $\mathbf{E}_i$ ($i$ = 1, 2, 3) in the laboratory coordinate system. The applied field polarizes the particles, which begin to electrostatically interact with each other. We use the approximation of pair interaction between particles considered as equivalent dipoles. In addition to electrostatic forces, viscous forces act on particles moving in the viscous fluid due to velocity gradients. The figure shows a configuration of an experimental setup, where the electrorheological fluid is subjected to both an electric field (the plates represent electrodes) and velocity gradient. The left positive electrode is fixed, while the right one moves from its initial position with the given velocity $\mathbf{U}$. Thus, the experimental setup provides both electrostatic and viscous forces on each particle.

The origin of the Cartesian laboratory coordinate system with the axes $X_i$ ($i$ = 1, 2, 3) is situated in the pattern center.

To derive the governing equation of motion, which represents the balance of forces applied to a chosen volume element of the model, we first derive an expression for the electrostatic potential energy density of the model.

We consider a pair of neighboring particles of the model and place the origin of the local coordinate system at the center of one of them. Particles are polarized by an external electric field, and the potential energy of their interaction with each other as equivalent dipoles has the form [9]

$$W = \frac{(\mathbf{p}_1, \mathbf{p}_2)}{4\pi\varepsilon_0\varepsilon_l r^3} - \frac{3(\mathbf{r}, \mathbf{p}_1)(\mathbf{r}, \mathbf{p}_2)}{4\pi\varepsilon_0\varepsilon_l r^5}. \quad (1)$$

Here, $p_i$ is the dipole moment of the $i$th particle, $\mathbf{r}$ is the

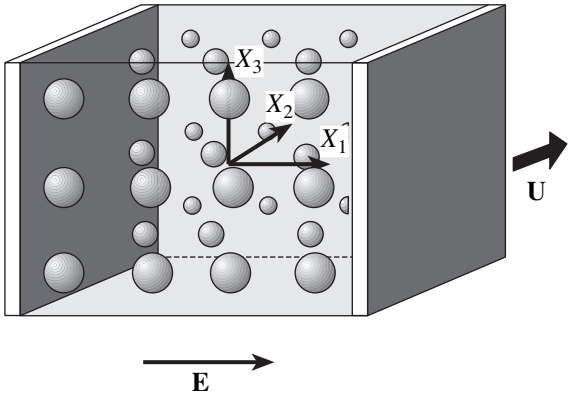


Configuration of the setup for experiments with an electrorheological fluid.

*Institute of Applied Mechanics,*
*Russian Academy of Sciences,*
*Leninskiĭ pr. 32a, Moscow, 117334 Russia*

1028-3358/03/4805-0224$24.00 

vector directed from the center of the chosen particle to the center of the closest neighboring particle, $r$ is the distance between the above-mentioned centers, $\varepsilon_0 = 8.85 \times 10^{-12}$ F/m is the permittivity of vacuum, and parentheses denote the scalar product.

The dipole moment of a polarized sphere is expressed as [3]

$$\mathbf{p} = \frac{\pi}{2}\varepsilon_0\varepsilon_1\frac{(\varepsilon_p - \varepsilon_1)a^3}{(\varepsilon_p + 2\varepsilon_1)}\mathbf{E}, \quad (2)$$

where $a$ is the sphere diameter. It is assumed that all particles of the dispersed phase are identical and the dipole moments of equivalent dipoles are equal to each other. Substituting Eq. (2) into Eq. (1), we obtain

$$W = A\left[\frac{E^2}{r^3} - \frac{3(\mathbf{r}, \mathbf{E})^2}{r^5}\right], \quad (3)$$

where $A = \dfrac{\pi\varepsilon_0\varepsilon_1(\varepsilon_p - \varepsilon_1)^2 a^6}{16(\varepsilon_p + 2\varepsilon_1)^2}$.

For small displacements of particles with respect to each other ($\mathbf{r} = \mathbf{r}^0 + \mathbf{u}$, where $u \ll r^0$ and $r^0$ is the initial distance between the centers of the particles), the potential energy of the dipoles is equal to

$$W = A\left[\frac{1}{r^{03}}(E^2 - 3\overset{1}{e}_l\overset{1}{e}_k E_l E_k)\right.$$

$$-\frac{3}{r^{04}}(E^2 - 5\overset{1}{e}_l\overset{1}{e}_k E_l E_k)\overset{1}{e}_n u_n - \frac{6}{r^{04}}\overset{1}{e}_k E_k E_l u_l$$

$$-\frac{3}{2r^{05}}(E^2 - 5\overset{1}{e}_l\overset{1}{e}_k E_l E_k)u_n u_n$$

$$+\frac{15}{2r^{05}}(E^2 - 7\overset{1}{e}_l\overset{1}{e}_k E_l E_k)\overset{1}{e}_n\overset{1}{e}_m u_n u_m$$

$$\left.-\frac{3}{r^{05}}(E_i u_i - 10\overset{1}{e}_m u_m\overset{1}{e}_k E_k)E_n u_n\right] \quad (4)$$

up to the second order, where summation over repeated indices is implied and $\overset{1}{e}_l = \dfrac{r_l^0}{r^0}$ is the unit vector. Correspondence of this vector to the chosen pair of neighboring particles will be denoted as $\overset{1}{e}_n\begin{pmatrix} l & l' \\ s & s' \end{pmatrix}$, where $l$ and $l'$ mark the unit lattice cells of the two neighboring particles and $s$ and $s'$ number the particles in the corresponding cells. Particle displacements with respect to each other will be denoted in a similar way. Summing expression (4) over the closest neighbors of the chosen particle throughout the unit cell and dividing the sum by the doubled cell volume $V$, we obtain the electrostatic energy density of the model in the form

$$\Phi = \frac{A}{2V}\sum_{l's'}\left[\frac{1}{r^{03}}\left(E^2 - 3\overset{1}{e}_l\begin{pmatrix} l & l' \\ s & s' \end{pmatrix}\overset{1}{e}_k\begin{pmatrix} l & l' \\ s & s' \end{pmatrix}E_l E_k\right)\right.$$

$$-\frac{3}{r^{04}}\left(E^2 - 5\overset{1}{e}_l\begin{pmatrix} l & l' \\ s & s' \end{pmatrix}\overset{1}{e}_k\begin{pmatrix} l & l' \\ s & s' \end{pmatrix}E_l E_k\right)$$

$$\times\overset{1}{e}_n\begin{pmatrix} l & l' \\ s & s' \end{pmatrix}u_n\begin{pmatrix} l & l' \\ s & s' \end{pmatrix}$$

$$-\frac{6}{r^{04}}e_k^1\begin{pmatrix} l & l' \\ s & s' \end{pmatrix}E_k E_l u_l\begin{pmatrix} l & l' \\ s & s' \end{pmatrix}$$

$$-\frac{3}{2r^{05}}\left(E^2 - 5\overset{1}{e}_l\begin{pmatrix} l & l' \\ s & s' \end{pmatrix}\overset{1}{e}_k\begin{pmatrix} l & l' \\ s & s' \end{pmatrix}E_l E_k\right)$$

$$\times u_n\begin{pmatrix} l & l' \\ s & s' \end{pmatrix}u_n\begin{pmatrix} l & l' \\ s & s' \end{pmatrix}$$

$$+\frac{15}{2r^{05}}\left(E^2 - 7\overset{1}{e}_l\begin{pmatrix} l & l' \\ s & s' \end{pmatrix}\overset{1}{e}_k\begin{pmatrix} l & l' \\ s & s' \end{pmatrix}E_l E_k\right)$$

$$\times\overset{1}{e}_n\begin{pmatrix} l & l' \\ s & s' \end{pmatrix}\overset{1}{e}_m\begin{pmatrix} l & l' \\ s & s' \end{pmatrix}u_n\begin{pmatrix} l & l' \\ s & s' \end{pmatrix}u_m\begin{pmatrix} l & l' \\ s & s' \end{pmatrix}$$

$$-\frac{3}{r^{05}}\left(E_l u_l\begin{pmatrix} l & l' \\ s & s' \end{pmatrix} - 10\overset{1}{e}_m\begin{pmatrix} l & l' \\ s & s' \end{pmatrix}u_m\begin{pmatrix} l & l' \\ s & s' \end{pmatrix}\right.$$

$$\left.\left.\times\overset{1}{e}_k\begin{pmatrix} l & l' \\ s & s' \end{pmatrix}E_k\right)E_n u_n\begin{pmatrix} l & l' \\ s & s' \end{pmatrix}\right]. \quad (5)$$

The first term (the first line) of the sum in the square brackets in Eq. (5) represents the interaction energy of the chosen dipole with the closest neighboring dipoles. It is equal to zero for an isotropic body and a crystal with cubic symmetry [10], as well as for bcc, fcc, and hexagonal lattices. This statement is verified by directly calculating the sums for these lattices with the expressions for components of the unit vectors $\overset{1}{e}_l$ from [11, 12] and is associated with the fact that the total field formed by the closest neighboring particles vanishes on the chosen dipole in these lattices.

Further, we consider the particular case corresponding to the figure. The electrostatic field $\mathbf{E}$ is directed along the $X_1$ axis so that its components are $E_i = E\delta_{i1}$, where $\delta_{i1}$ is the Kronecker delta, which is equal to unity and zero for $i = 1$ and $i \neq 1$, respectively. It is assumed

that the displacement is uniform and its gradient $\frac{\partial u_i}{\partial x_k}$ ($u_i$ is the component of the displacement of a body point from its initial position) is constant throughout the sample. According to the figure, $i = 2$ and $k = 1$. Direct calculations show that the term linear in displacements in Eq. (5) vanishes for the above types of lattices. In addition, the last line of Eq. (5) also vanishes, because the displacement is perpendicular to the electric field (see figure), and therefore $(E_n, u_n) = 0$. Finally, the electrostatic energy density of the model for this case is expressed in the form

$$\Phi = \frac{A}{2V}\sum_{l's'}\left[-\frac{3}{2r^{05}}\left(E^2 - 5e_1^{12}\begin{pmatrix} l & l' \\ s & s' \end{pmatrix}E^2\right)u_2^2\begin{pmatrix} l & l' \\ s & s' \end{pmatrix}\right.$$
$$\left.+\frac{15}{2r^{05}}\left(E^2 - 7e_2^{12}\begin{pmatrix} l & l' \\ s & s' \end{pmatrix}E^2\right)e_2^{12}\begin{pmatrix} l & l' \\ s & s' \end{pmatrix}u_2^2\begin{pmatrix} l & l' \\ s & s' \end{pmatrix}\right], \quad (6)$$

where all terms are quadratic in the displacement of particles, which is related to the displacement gradient as

$$u_m = r^0 u_{n,k} e_k^1. \quad (7)$$

External forces causing the displacement gradient $u_{2,1}$ in the body do the work per unit volume $F$, which is opposite to the electrostatic field energy (6) [10].

In what follows, we omit indices numbering cells and particles in them and denote the summation over the closest neighbors as cn.

Substitution of Eq. (7) into Eq. (6) and certain transformations yield

$$F = \frac{3AE^2}{4Vr^{03}}u_{2,1}^2\sum_{\text{cn}}(1 - 5e_1^1e_1^1)e_1^1e_1^1$$
$$-5(1 - 7e_1^1e_1^1)e_1^1e_1^1e_2^1e_2^1]. \quad (8)$$

Since the displacement gradient is constant throughout the sample, it is extracted from the sum.

The numerical simulation [4] shows that particles of the electrorheological fluid are aggregated in a tetragonal body-centered crystal lattice. Therefore, we choose a bcc lattice and describe the rheological properties of this model.

Direct calculations by Eq. (8) for a bcc lattice yield

$$F = \frac{7\pi\varepsilon_0\varepsilon_1(\varepsilon_p - \varepsilon_1)^2a^6E^2}{36(\varepsilon_p + 2\varepsilon_1)^2Vr^{0^3}}u_{2,1}^2. \quad (9)$$

Stress is calculated from Eq. (9) as

$$\sigma_{21} = \frac{\partial F}{\partial u_{2,1}} = \frac{14\pi\varepsilon_0\varepsilon_1(\varepsilon_p - \varepsilon_1)^2a^6}{36(\varepsilon_p + 2\varepsilon_1)^2Vr^{03}}E^2u_{2,1}. \quad (10)$$

Using the volume $V = \frac{4}{3\sqrt{3}}r^{03}$ of a unit cell [11, 12], we obtain the relation $\frac{a^6}{Vr^{03}} = \frac{16\sqrt{3}}{\pi^2}\varphi^2$, where the volume fraction $\varphi$ of filling is equal to the ratio of the particle volume to the unit-cell volume of the bcc lattice. The substitution of the last expression into Eq. (10) yields

$$\sigma_{21} = 3.43\varepsilon_0\varepsilon_l\beta^2\varphi^2E^2u_{2,1}, \quad (11)$$

where $\beta = \frac{\varepsilon_p - \varepsilon_l}{\varepsilon_p + 2\varepsilon_l}$.

The viscous stress tensor for the bcc lattice is given by the formula [8, 12]

$$\sigma'_{21} = 0.21\pi\psi(\varphi)\eta\dot{u}_{2,1}, \quad (12)$$

where $\psi(\varphi) = \left(\frac{\varphi}{\varphi_{\max}}\right)^{4/3}\left[1 - \left(\frac{\varphi}{\varphi_{\max}}\right)^{1/3}\right]^{-3}$ and $\varphi_{\max}$ is the maximum filling. Expression (12) is derived in the approximation of high filling, when $\varphi$ is close to $\varphi_{\max}$ [8, 12]. If $\varphi$ tends to zero, $\psi(\varphi)$ also tends to zero.

However, at $\varphi = 0$, relation (12) must take the form $\sigma'_{21} = \eta\dot{u}_{2,1}$ characteristic for a pure fluid. The function

$$\tilde{\sigma}_{21} = [0.21\pi\psi(\varphi) + 1]\eta\dot{u}_{2,1} \quad (13)$$

satisfies these conditions.

The equation of motion of the system represents the balance of external and internal elastic (11) and viscous (13) forces applied to the unit body volume. It has the form

$$3.43\varepsilon_0\varepsilon_l\beta^2E^2\varphi^2u_{2,1}$$
$$+[0.21\pi\psi(\varphi) + 1]\eta\dot{u}_{2,1} = f_{21}(t). \quad (14)$$

Here, $f_{21}(t)$ is the time-dependent external force per unit area. It is directed along the $X_2$ axis and is applied to the surface perpendicular to the $X_1$ axis. A solution of Eq. (14) is known for an arbitrary given function $f_{21}(t)$. In particular, if load varies as a periodic function $f = f_{21}^0 e^{i\omega t}$ with the cyclic frequency $\omega$, we have [13]

$$u_{2,1}(t) = 0.29\frac{f_{21}^0}{\varepsilon_0\varepsilon_l\beta^2\varphi^2E^2}\frac{1}{1 + i\omega\tau}e^{i\omega t}. \quad (15)$$

Therefore, the complex shear modulus is written in the form

$$G^* = 3.43\varepsilon_0\varepsilon_l\beta^2E^2\varphi^2 + i\omega[0.21\pi\psi(\varphi) + 1]\eta, \quad (16)$$

which shows that, for small displacement gradients under the loading conditions described in the figure, the electrorheological fluid behaves as a viscoelastic body.

An important advantage of the approach under development is that an expression for stress can be

obtained for arbitrary displacement gradients by using both a microscopic theory of crystals and the results for small displacement gradients (14). As a result, stress can be determined as a function of the velocity gradient in an electrorheological fluid. To obtain this dependence, we use the Peierls approach presented in [11]. According to the crystal model (see figure), the elastic part of stress (11) associated with the displacement of crystal planes must be a periodic odd function of the displacement $S_2 = \gamma X_1$ along the $X_2$ axis, where $\gamma$ is the displacement gradient. Expanding this function in a Fourier series and retaining only the first term of the latter, we obtain

$$\sigma_{21}(S_2) \approx a_1 \sin\left(2\pi\frac{S_2}{c}\right),$$

where $c$ is the lattice constant. For small displacements, this expression must take the form of Eq. (11). Consequently, $a_1 = \frac{3.43}{2\pi}\varepsilon_0\varepsilon_l\beta^2E^2$ and the maximum displacement stress, which is an analogue of the yield stress of a crystal, can be estimated as

$$\sigma_{\max} \approx \frac{3.43}{2\pi}\varepsilon_0\varepsilon_l\beta^2\varphi^2E^2.$$

Thus, the final expression has the form

$$f_{21} = \frac{3.43}{2\pi}\varepsilon_0\varepsilon_l\beta^2\varphi^2E^2 + [0.21\pi\psi(\varphi) + 1]\eta\dot{u}_{2,1}. \quad (17)$$

For small velocity gradients, the second term can be neglected and the stress is determined by the first term of Eq. (17). In this case, the stress is independent of the velocity gradient, so that the corresponding part of the stress vs. velocity gradient plot is a straight line parallel to the abscissa axis. For large velocity gradients, the first term can be neglected and the diagram corresponds to the Newtonian flow. The dependence of the stress on both the electric intensity and the velocity gradient that is described by Eq. (17) agrees well with the experimental data [14]. We note that, if pair interaction between particles is taken into account up to the third order, a factor of 5.54 appears in Eq. (17) instead of 3.43.

## ACKNOWLEDGMENTS

This work was supported by the Russian Foundation for Basic Research, project no. 02-01-01060.

## REFERENCES

1. L. G. Loĭtsyanskiĭ, *Fluid and Gas Mechanics* (Nauka, Moscow, 1973).
2. A. V. Lykov, Z. P. Shul'man, and Yu. F. Deinega, *Electrorheological Effect* (Nauka i Tekhnika, Minsk, 1972).
3. Y. M. Shkel and D. J. Klingenlerg, J. Rheol. **43** (5), 1307 (1999).
4. R. Tao and Qi Jiang, Phys. Rev. Lett. **73**, 205 (1994).
5. P. M. Adriani and A. R. Gast, Phys. Fluids **31**, 2757 (1988).
6. A. M. Kraynik, R. T. Bonnecaze, and J. F. Brady, in *Proceedings of International Conference on Electrorheological Fluids, Singapore, October 15–16, 1991* (World Science, Singapore, 1992), p. 59.
7. J. E. Martin and R. A. Anderson, J. Chem. Phys. **104** (12), 4814 (1996).
8. V. E. Zgaevskiĭ, Dokl. Akad. Nauk **350** (1), 45 (1996) [Phys. Dokl. **41**, 412 (1996)].
9. W. Panofsky and M. Fillips, *Classical Electricity and Magnetism* (Addison-Wesley, Cambridge, Mass., 1962; Fizmatgiz, Moscow, 1963).
10. I. E. Tamm, *Principles of Electricity Theory* (Nauka, Moscow, 1989).
11. G. Leibfried, *Gittertheorie der Mechanischen und Thermischen Eigenschaften der Kristalle. Handbuch der Physik* (Springer-Verlag, Berlin, 1955; Fizmatgiz, Moscow, 1963), Vol. 7, Part 2.
12. V. E. Zgaevskiĭ and Yu. G. Yanovskiĭ, Mekh. Kompoz. Mater. Konstr. **2** (1), 137 (1996).
13. I. Narisava, *Strength of Polymeric Materials* (OHMSHA, Tokyo, 1982; Khimiya, Moscow, 1987).
14. L. Marshall, C. F. Zukoski, and J. W. Goodwin, J. Chem. Soc., Faraday Trans. 1 **85** (9), 2785 (1989).

*Translated by Yu. Verevochkin*

*Doklady Physics, Vol. 48, No. 5, 2003, pp. 228–231. Translated from Doklady Akademii Nauk, Vol. 390, No. 2, 2003, pp. 192–195.*


**TECHNICAL PHYSICS**

# Heat Transfer in Pulse-Superheated Liquids

**P. V. Skripov*, A. A. Starostin, and D. V. Volosnikov**

Presented by Academician V.E. Fortov November 25, 2002

Received November 25, 2002

Thermophysical properties [thermal conductivity $\lambda(p, T)$ and thermal diffusivity $a(p, T)$, which depend on pressure $p$ and temperature $T$] are usually determined for liquids in a stable state. Measurements are carried out with small temperature perturbation $\delta T(t) \ll T_0$ [1]. Reference to the thermostat temperature $T_0$ and long measurement time $t_{exp}$ provide the upper limit of the temperature range in a thermophysical experiment $\Delta T = T_s(p) - T_0$, where $T_s(p)$ is the temperature of the equilibrium coexistence of a liquid and vapor. The region beyond the line of the absolute stability of the liquid is poorly studied.

We aim to experimentally study heat transfer in short-lived liquids superheated with respect to the equilibrium temperature $T_s(p)$ and/or with respect to the onset temperature $T_d$ of the thermal destruction of molecules in a quasi-static process. The investigation is distinctive because the system lifetime $\bar{t}(T)$ is limited, and the farther the system is from thermal stability, the more stringent is this limit. The approach under development is aimed at creating short-term quasi-isothermal conditions $t$ ($T$ = const) in a chemically reacting system, $t_{exp} < \bar{t}$). Single- and multicomponent polymer liquids were studied as typical thermally unstable systems ($T_d < T_c$, where $T_c$ is the effective critical temperature of a substance). In pulsed processes with characteristic times $t_{exp} \sim 10^{-5}$–$10^{-3}$ s, a polymer can be substantially superheated with respect to a temperature of $T_d$ with negligible thermal destruction [2].

To solve the problem, we developed methods for an automatic choice of the heating function for a thermal probe, determination of the phase stability boundary by using the heat flux density into the substance $q(t)_T$, and calculation of the effective coefficients of thermal conductivity and thermal activity of locally superheated liquids on the basis of pulsed-experiment data and chosen model of the process. Experiments were carried out in a virtually unstudied part of the phase diagram, including experiments where a system exhibits phase and chemical instabilities as factors perturbing the heat-transfer process.

For definiteness, we analyze the liquid–vapor phase diagram for a monomer (lines *1* and *2* with point *3* in Fig. 1). The upper limit of the region of stable states of the liquid in the $p$–$T$ plot is determined by the binodal $T_s(p)$. The region that is located above the binodal and below the attainable-superheating curve $T^*(p)$ is the region of metastable (superheated) states of the liquid [3]. The latter line can be observed in an experiment, because the spontaneous boiling of the highly superheated liquid is almost at the threshold temperature.

As the length of the molecular chain increases sequentially and achieves a certain critical value, the critical temperature of the liquid and then the curve $T^*(p)$ exceed a temperature of $T_d$ (lines *4* and *5* in

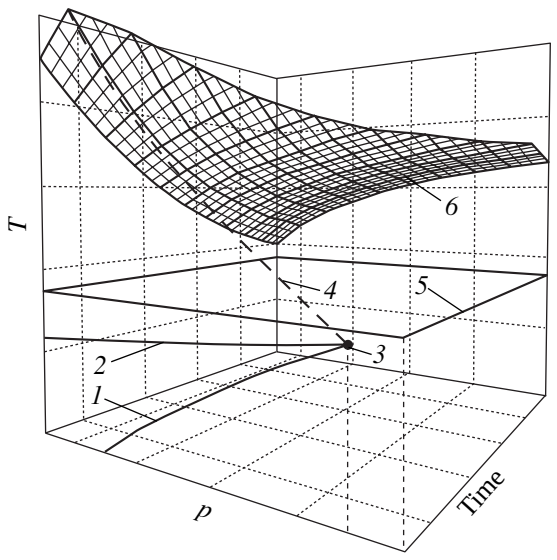


**Fig. 1.** Phase diagram of a monomer in $p$–$T$ coordinates: (*1*) $T_s(p)$ binodal, (*2*) attainable-superheating curve $T^*(p)$, (*3*) critical point, (*4*) line of the critical points in a monomer–polymer system, (*5*) temperature $T_d$ of the thermal destruction of the liquid in a quasi-static process, and (*6*) kinetic surface $T^*(p; t_{exp})$ of the spontaneous boiling for the products of the thermal destruction of the pulse-heated polymer liquid.

*Institute of Thermal Physics, Ural Division, Russian Academy of Sciences, ul. Pervomaĭskaya 91, Yekaterinburg, 620219 Russia*

** e-mail: pavel-skripov@lyceum.usu.ru*

1028-3358/03/4805-0228$24.00 

Fig. 1). In this case, the liquid–vapor phase transition ceases to be pointlike and is expanded in temperature. Since the characteristic time of spontaneous boiling is much less than the temperature of thermal destruction ($t_{sb} \ll t_d$ at a comparable transformation degree [4]), the coordinates in the attainable superheating curve correspond to the initial stage of thermal destruction and depend on the heating time (line *6* in Fig. 1). Since the thermal destruction process is involved in the relaxation of the pulse-superheated polymer, it is possible to observe boiling in the melt of macromolecules. The temperature range $T^*(t_{exp})$–$T_d$ of the thermal instability of polymers achieves 500 K [2, 4–6]. Numerical data concerning the characteristics of heat transfer in this temperature range are absent.

It is important to apply an appropriate method for solving the problem under consideration. A search for a method of controlling the probe temperature, as well as analysis of both the engineering capability of experiments and the correspondence of their conditions to the mathematical description of the process, led us to a new variant of the isothermal-heater method [7], the method of the thermal stabilization of a pulse-superheated probe. It is based on the selection of a combination of a short heating pulse and thermal stabilizing pulse serving as a highly sensitive transmitter of the heat-transfer intensity in the experiment. The advantage of the method is that the desired quantity—heat transfer from the thermally stabilized probe to the medium—is in balance with electric power supplied to the probe, which is a quantity convenient for automatic adjustment and detection [8] (Fig. 2).

The method enables one to rapidly increase the probe temperature up to a chosen "plateau" temperature $T_{pl}$ and to maintain this temperature $T(t > t_{pl}) \approx T_{pl}$ during the time interval necessary for measurement. A wire probe 20 μm in diameter achieves the thermal-stabilization regime in $t_{pl} \approx 100$ μs, and a constant temperature is maintained for $t_{exp} - t_{pl} \sim 1$–$10$ ms. This regime is convenient, because the characteristics of heat transfer are involved at a definite temperature and the probe temperature can be gradually increased from one experiment to another up to the attainable-superheating temperature of the substance. As an example, Fig. 2 shows the heating function near the spontaneous-boiling temperature $T^*(t - t_{pl})$ at $t_{exp} = 2.7$ ms. The solid line is the projection of the boundary of substance continuity breaking $t^* = \bar{t}(T_{pl})$. Heat exchange between the probe and two-phase medium is perturbed at $t > t^*$. This "unexpected" perturbation is detected by the fast feedback system and is compensated by the corresponding change in the heating function, which maintains the probe temperature near a given value of $T_{pl}$.

Test experiments with standard substances (toluene, hexadecane) showed that the input $P(t)$ and output $T(t)$ functions are reproducible and consistent with each other. The high resolution of the method is revealed when pressure is taken as a parameter, ensuring a small

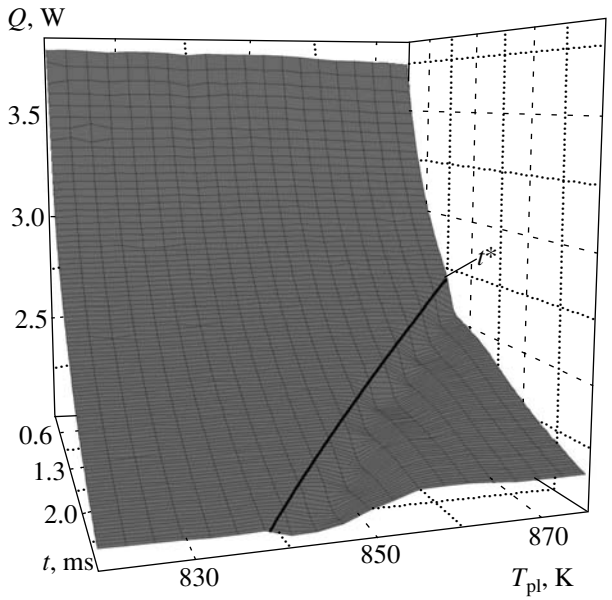


**Fig. 2.** Heat power that must be released in the probe for its thermal stabilization in polymethyl siloxane PMS-350 as a function of the heating time and temperature $T_{pl}$. The spontaneous-boiling region to the right from the $t^* = \bar{t}(T_{pl})$ line is characterized by a time-localized increase in the thermal resistance of the system.

shift in the characteristics of heat transfer in the substance.

At the next stage, it is necessary to separate contributions associated in the generalized heat-transfer function with thermal conductivity and thermal diffusivity of the substance. These contributions are effective values, because local superheating is high and observations are short-term. The correspondence between the electric quantities measured in the experiment and thermophysical properties of the substance is established in the model of unsteady heat exchange between an instantaneously thermostated cylinder and a substance with zero temperature [9]. Assuming that the thermal contact is ideal, superheating $\Delta T$ does not vary over the probe length, and coefficients λ and $a$ are temperature independent, we write heat exchange in the form

$$q(t) = \frac{I^2(t)R_T}{2\pi rl}$$

$$= \frac{4\lambda\Delta T}{\pi^2 r}\int_0^\infty e^{-au^2t}\frac{du}{u[J_0^2(ru) + Y_0^2(ru)]}, \qquad (1)$$

where $r$ and $l$ are the radius and length of the probe, $I(t)$ is the current through the wire probe thermometer with a resistance of $R_T = R(T)$, and $J_0$ and $Y_0$ are the Bessel functions.

For convenience, we consider the regular stage of the thermal regime [7]. The corresponding dimension-

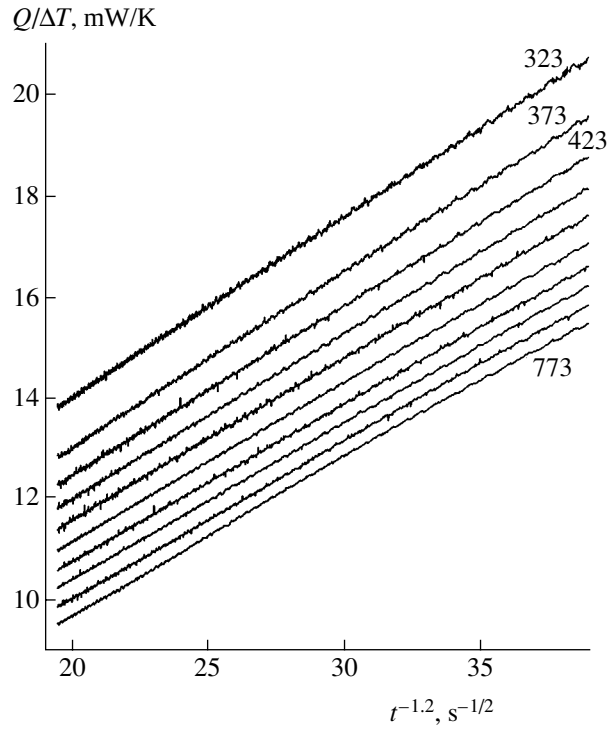


**Fig. 3.** Superheating-divided heat power that must be released in the probe for its thermal stabilization in polymethyl siloxane PMS-350 vs. $t^{-1/2}$, where $t$ is the heating time, for $T_{pl}$ varying from 323 to 773 K with a step of 50 K.

less time range (Fourier number) is $\mathrm{Fo} = \dfrac{at}{r^2} = 0.25–1$. In this interval, the dimensionless heat flux $\dfrac{qr}{\lambda\Delta T}$, where $q$ is given by Eq. (1), as a function of $\mathrm{Fo}^{-1/2}$ is approximated by the linear function

$$\frac{qr}{\lambda\Delta T} = 0.392 + 0.594\ \mathrm{Fo}^{-1/2} = A + B\ \mathrm{Fo}^{-1/2} \qquad (2)$$

to within an accuracy of 99%. Relation (2) indicates an obvious method for separating the contributions associated with thermal conductivity and thermal activity $b = \lambda a^{-1/2}$ of the substance. End corrections are taken into account by measurements with probes of various lengths. The final relations for a pair of probes with lengths $l_1$ and $l_2$ have the simple form

$$\lambda = \frac{1}{2\pi A}\frac{C_1 - C_2}{l_1 - l_2} = 0.406\frac{C_1 - C_2}{l_1 - l_2},$$
$$b = \frac{1}{2\pi B r}\frac{K_1 - K_2}{(l_1 - l_2)} = 0.268\frac{K_1 - K_2}{r(l_1 - l_2)}, \qquad (3)$$

where $C$ and $K$ are experiment constants.

The applicability of the model to the real process was verified by the direct use of Eq. (1) in the iteration procedure of the formation of a thermal stabilizing pulse [2] and by the generalization of experimental data in coordinates corresponding to Eq. (2). It was revealed that these data can be represented in the linear approximation in wide ranges of temperature (323–923 K), pressure (0–4 kbar) [10], and probe length (0.5–5 cm). In particular, Fig. 3 shows the results of data processing for various temperatures $T_{pl}$. Changes in shift and slope of isotherms indicate a decrease in heat transfer with increasing temperature.

The total scheme of experiments with thermally unstable objects includes various measurements. The temperature $T^*(p)$ of the attainable superheating of a substance was determined by the method of monotonic pulsed heating with variation of the thermostat temperature $T_0$ and rate of heating. The temperature of the characteristic step in the smooth dependence $T^*(T_0)$, which is associated with the appearance of the first low-molecular products in the system, was considered as the thermal-destruction temperature $T_d$ for the polymer. The coordinates of the end point of the attainable superheating curve $T^*(p; t \longrightarrow 0)$ were taken as an approximation for the critical point, which was used to generalize experimental data concerning heat transfer in the dimensionless coordinates. Then, the method of the iteration selection of the heating function is applied to simulate the thermal stabilization regime [2] and to estimate the boundary $T_{pl}$–$\bar{t}$ of the region where the sample exhibits short-term thermal stability and pulsed measurements of its thermophysical properties are possible.

When measuring the coefficients $\lambda(T; t < \bar{t})$ and $b(T; t < \bar{t})$ for high-molecular-weight compounds, current $I(t)$ in the probe circuit was recorded for a constant thermal resistance $R_T$ of the probe and given superheating $\Delta T = T_{pl} - T_0$. Using these data for times $\bar{t} \geq 1$ ms, we determined the ratio of heat release in the probe to its superheating (Fig. 3). The effective thermophysical properties were calculated by Eqs. (3) for known sizes of the probe.

Figure 4 shows the thermal conductivity measured for PMS-350 polymethyl siloxane ($T_d \approx 570$ K) and Stirosil polystyrene–polysiloxane copolymer ($T_d \approx 490$ K) in a wide temperature range $\dfrac{T}{T_c} \sim 0.3–0.9$. In the temperature range characteristic for quasi-static changes, our results for PMS-350 agree with the data on the molecular thermal conductivity [11], which were obtained by a precise method, when a cell was thermostated at the measurement temperature. The last points in the plots, which deviate from the smooth continuation of $\lambda(T)$, are of interest for discussing the specific behavior of heat transfer in the thermal-instability region. These points include the contribution from the thermal destruction and microphase separation of the components of the chemically active system in the heat-transfer process. This deviation increases, and the cor-

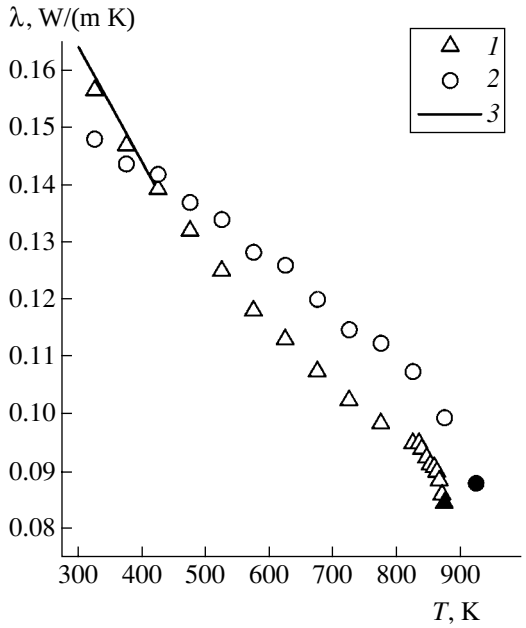


**Fig. 4.** Thermal conductivity of (triangles) PMS-350 polymethyl siloxane and (circles) Stirosil polystyrene–polysiloxane copolymer vs. temperature for $T_0$ = 295 K, $t_{exp}$ = 2.7 ms, and $p$ = 0.1 MPa. The straight line approximates data obtained in [11] by the method of the equivalent impedance for the identical PMS-350 sample. The solid points correspond to the system lifetime $\dot{t}(T_{pl})$ = 1 ms minimal in our experiments.

responding temperature decreases, when carbon dioxide, which imitates the final products of thermal destruction, dissolves in given substances. After spontaneous boiling, the perturbation of heat transfer is alternating, which is determined by pressure and by the length of the thermal stabilization interval $\delta q(t) = \delta q(p; t^* - t_{pl})$. The entire set of objects under study (in addition to those indicated above, these are polyethers and motor and synthetic compressor oils) exhibit a common tendency to decreasing λ and $b$ with increasing temperature. This result was not *a priori* obvious. Data obtained by various authors on the sign of $\lambda(T)$ for melts of identical polymers are contradictory [12].

Thus, an approach to studying heat transfer in the region of the thermal instability of a substance was developed. It can be applied to compare the thermophysical properties of substances as functions of the superheating degree and to follow the transformation of the high-temperature part of the phase diagram for a chemically active system by using the characteristic perturbation of its thermal resistance.

## ACKNOWLEDGMENTS

This work was supported by the Russian Foundation for Basic Research, project nos. 00-15-96719 and 02-02-16243.

## REFERENCES

1. L. P. Filippov, *Measurement of Thermophysical Characteristics of Substances* (Énergoatomizdat, Moscow, 1984).
2. P. V. Skripov, A. A. Starostin, and S. E. Puchinskis, Dokl. Akad. Nauk **375**, 615 (2000) [Dokl. Phys. **45**, 663 (2000)].
3. V. P. Skripov, *Metastable Liquid* (Nauka, Moscow, 1972; Wiley, New York, 1974).
4. P. A. Pavlov and P. V. Skripov, Teplofiz. Vys. Temp. **36** (3), 448 (1998).
5. S. E. Puchinskis and P. V. Skripov, Int. J. Thermophys. **22** (6), 1755 (2001).
6. D. V. Volosnikov, P. V. Skripov, and A. A. Starostin, *Physics of the Extreme State of Matter* (Inst. Probl. Khim. Fiz., Ross. Akad. Nauk, Chernogolovka, 2001), pp. 103–105.
7. E. S. Platunov, S. E. Buravoĭ, V. V. Kurepin, and G. S. Petrov, *Thermophysical Measurements and Instruments* (Mashinostroenie, Leningrad, 1986).
8. S. Yu. Afanas'ev, S. A. Zhukov, and S. B. Echmaev, Teplofiz. Vys. Temp. **34** (4), 583 (1996).
9. H. Carslaw and J. Jaeger, *Conduction of Heat in Solids* (Clarendon Press, Oxford, 1959; Nauka, Moscow, 1964).
10. D. V. Volosnikov, P. V. Skripov, and A. A. Starostin, *Physics of the Extreme State of Matter* (Inst. Probl. Khim. Fiz., Ross. Akad. Nauk, Chernogolovka, 2001), pp. 62–64.
11. A. V. Baginskiĭ, S. V. Stankus, and R. A. Khaĭrulin, in *Proceedings of X Russian Conference on Thermophysical Properties of Materials* (Kazan Gos. Tekh. Univ., Kazan, 2002), p. 78.
12. D. Hands, Rubber Chem. Technol. **50** (3), 480 (1977).

*Translated by R. Tyapaev*

*Doklady Physics, Vol. 48, No. 5, 2003, pp. 232–234. Translated from Doklady Akademii Nauk, Vol. 390, No. 3, 2003, pp. 330–332.*


**TECHNICAL PHYSICS**

# Effect of the Rotor Shape on the Efficiency of a Liquid Centrifuge

**Academician G. A. Abakumov and V. B. Fedoseev**

Received February 14, 2003

Previously, we showed that the shape effect can substantially modify the composition and the distribution of chemical components in gas [1] and liquid [2] mixtures. In this study, we considered those features of the vessel-shape effect in liquid-phase systems that can provide much higher degrees of separation in liquid centrifuges than for gas mixtures.

From the condition of a constant mechanical–chemical potential in equilibrium [1], the distribution of the component concentration over the rotor radius is found in the form

$$\Pi_i = \mu_i^{0L} + RT\ln x_i(r) - \frac{M_i\omega^2 r^2}{2} + \overline{V}_i P(r), \qquad (1)$$

$$x_i(r) = \exp\left(\frac{\Pi_i - \mu_i^{0L} + \frac{M_i\omega^2 r^2}{2} - \overline{V}_i P(r)}{RT}\right), \qquad (2)$$

where $x_i(r)$ is the molar fraction of the $i$th component at the radius $r$, $\mu_i^{0L}$ is the standard chemical potential of the component in a liquid, $\overline{V}_i$ is the molar volume of the component, $M_i$ is the molecular mass of the component, and $\omega$ is the angular velocity of the centrifuge rotor,

$$P(r) = \int_{r_h}^{r} \rho(r)\omega^2 r dr$$

is the hydrostatic pressure at the radius $r$, $\rho(r)$ is the local density of the liquid at the radius $r$, and $r_h$ is the liquid-surface radius. For a binary mixture, it follows from Eqs. (1) and (2) that

$$\ln\frac{x_1(r)}{x_1(r_0)} - b\ln\frac{x_2(r)}{x_2(r_0)} = -\frac{\omega^2(r_0^2 - r^2)}{2RT}(M_1 - bM_2), \qquad (3)$$

where

$$b = \frac{M_1\rho_2}{M_2\rho_1} = \frac{\overline{V}_1}{\overline{V}_2};$$

$x_i(r_0)$ is the $i$th-component concentration at the rotor radius $r = r_0$. Relationship (3) describes the composition at an arbitrary point of the two-component system in the form $x_i(r) = f(x_i(r_0))$.

We describe the two-component mixture in the cylindrical rotor with a conic diaphragm dividing the rotor in two insulated sections (see Fig. 1a). The generatrices of the upper ($u$) and lower ($d$) sections have the form $h_u(r) = \frac{L}{r_0} r$ and $h_d(r) = \frac{L}{r_0}(r_0 - r)$, respectively. The

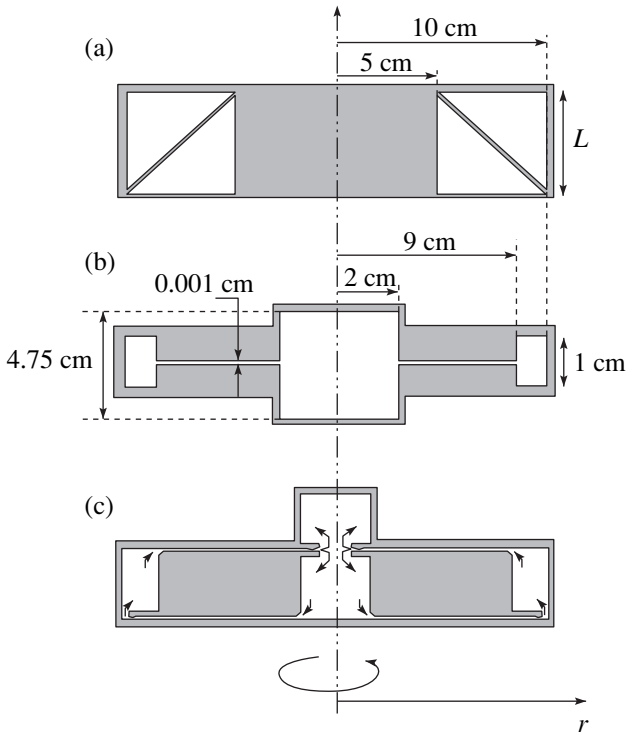


**Fig. 1.** Section of rotors; the colorless section is filled with a liquid, the dark one is the rotor material.

*Razuvaev Institute of Organometallic Chemistry, Russian Academy of Sciences, ul. Tropinina 49, Nizhni Novgorod, 603600 Russia*

1028-3358/03/4805-0232$24.00 

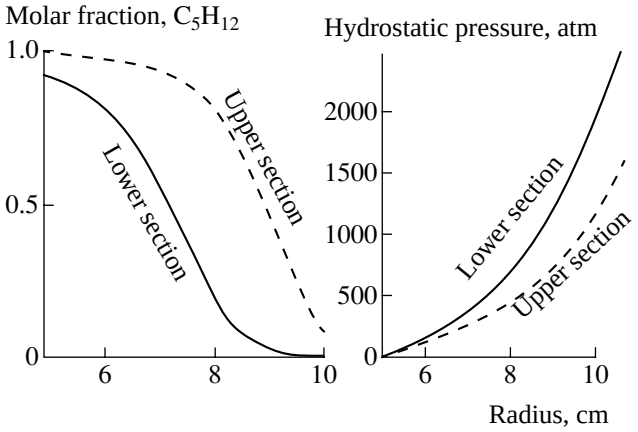


**Fig. 2.** Radial dependence of the pentane concentration and the hydrostatic pressure in the upper and lower sections of the rotor shown in Fig. 1a.

geometric sizes are indicated in Fig. 1. The volume concentration of the mixture is identical in both sections:

$$C_{i,s} = \frac{n_{i,s}}{V_s} = \frac{\int_{r_h}^{r_0} \frac{x_{i,s}(r)h_s(r)r}{\bar{V}_1 x_{1,s}(r) + \bar{V}_2 x_{2,s}(r)} dr}{\int_{r_h}^{r_0} h_s(r) r dr}$$

$$= \frac{\int_{r_h}^{r_0} \frac{x_{i,s}(r)h_s(r)r}{1 + x_{1,s}(r)(b-1)} dr}{\bar{V}_2 \int_{r_h}^{r_0} h_s(r) r dr}, \quad (4)$$

$$x_{1,s}(r) + x_{2,s}(r) = 1, \quad C_i = C_{i,u} = C_{i,d},$$

$$i = 1, 2, \quad s = u, d.$$

Equations (3) and (4) enable us to calculate $x_{i,s}(r)$ and $P_s(r)$ in both sections. We illustrate the result by the example of a particular system. The disconnected upper and lower sections of the rotor (Fig. 1a), whose angular velocity is equal to $\omega = 60000$ rpm, are filled with an equimolar pentane–methyl-iodide mixture, whose temperature is equal to $T = 300$ K. Under equilibrium in the centrifugal field, the $C_5H_{12}$ concentration and hydrostatic pressure in the upper section for an arbitrary radius $r$ are higher and lower than the respective quantities in the lower section (Fig. 2). Thus, the properties of the liquid-phase chemical system depend on the vessel shape much stronger than those of gaseous systems [1].

This feature of the behavior of liquids in a centrifuge makes it possible to search for nonstandard solutions to the fundamental problem of centrifugal technologies—the most complete separation of mixture components. We illustrate this by a particular example. The binary mixture of equal volumes of $CH_3I$ and $C_5H_{12}$ is placed in a rotor composed of two sections (Fig. 1b). The sections have the shapes of a cylinder and a ring, whose principal axes coincide with the rotation axis. The heights of the sections are chosen so that the volumes of the cylinder and ring are equal to the volumes of the light ($C_5H_{12}$) and heavy ($CH_3I$) components of the mixture, respectively. The sections are connected with each other by a slot cavity, whose volume is negligible compared to the cylinder and ring volumes. In the general case, the heights of the sections are chosen so that their volumes are equal to the volumes of the light and heavy components, respectively.

Using Eq. (4), we calculate the volume fractions of the components in every section for $T = 300$ K and $\omega = 60000$ rpm (see table).

This calculation shows that, in equilibrium, 98.92% of the $C_5H_{12}$ contained in the system is located in the cylinder section, whereas 98.97% of the $CH_3I$ is in the ring section of the rotor.

The centrifugal field made it possible to almost completely separate the components in the single-stage process. The result can be optimized by varying the rotation velocity, the radius and shape of the rotor sections, and other parameters. However, the successful use of the vessel-shape effect is principally based on minimizing the volume section where the mixture has an "unsatisfactory" composition.

The result obtained is purely thermodynamic. Meanwhile, the diffusivities in liquids are lower than

**Table**

| | Cylinder ($V$ = 59.7 ml) | Slot ($V$ = 0.24 ml) | Ring ($V$ = 59.7 ml) |
|---|---|---|---|
| $C_5H_{12}$, vol % | 99.12 | 63.06 | 0.82 |
| $CH_3I$, vol % | 0.88 | 36.94 | 99.17 |

those in gases by a factor of $10^5$. Therefore, the time of establishing equilibrium by means of diffusion through a narrow slot is very long. However, this time can be reduced by using the shape effect. We consider the rotor shown in Fig. 1c. The pressure drop between rotor sections of different shapes is caused by the difference in the radial distribution of the components. If the sections are connected by orifices at various levels as is shown in Fig. 1c, the pressure difference leads to the circulation of the liquid in the system until the radial distributions in sections are equalized. This situation corresponds to establishing equilibrium. It is evident that the time of this establishment is reduced to the extent to which the diffusion rate is lower than the viscous-flow velocity. We emphasize that the pressure difference plays here the role of feedback in self-controlled systems.

## REFERENCES

1. G. A. Abakumov and V. B. Fedoseev, Dokl. Akad. Nauk **365**, 608 (1999) [Dokl. Phys. **44**, 205 (1999)].
2. G. A. Abakumov and V. B. Fedoseev, in *Tests of Materials and Constructions* (Intelservis, Nizhni Novgorod, 2000), No. 2, pp. 164–167.

*Translated by V. Bukhanov*

*Doklady Physics, Vol. 48, No. 5, 2003, pp. 235–238. Translated from Doklady Akademii Nauk, Vol. 390, No. 3, 2003, pp. 333–336.*


**TECHNICAL PHYSICS**

# Features of the Film Boiling Regime on Wire Heaters in Subcooled Distilled Water

**S. A. Zhukov*, S. Yu. Afanas'ev, and S. B. Echmaev**

Presented by Academician A.I. Leont'ev January 23, 2003

Received November 26, 2002

As was shown in [1], the film boiling of organic liquids is accompanied by various chemical reactions most of whose products are gaseous compounds. To determine features of heat exchange due to chemical reactions, we carried out experiments concerning the film boiling of distilled water.

We applied a method close to that described previously for a short wire in [1]. The film regime was initiated at the saturation temperature, and power on an external heater was then decreased so that a liquid was cooled at a rate of 0.01–0.5°C per minute. In this process, with a step of 0.5°C, voltage on a sensor was recorded and boiling regimes were videotaped. Platinum wires with diameters 50, 100, and 200 μm and lengths from 0.8 to 40 mm were used as heaters.

In [1], the self-oscillating regime of heat transfer in the film boiling of subcooled liquids was observed, and it was supposed that a similar regime must also be realized in water.

Figure 1 shows some time scans of voltage on a short heater for various temperatures of the liquid. The heater length was chosen so that only one domain existed on the heater. For $T_{liq} = T_{sat}$, even such a heater ensures a film boiling regime similar to the film regime on a long element. This regime (Fig. 1, $T_{liq} = 98$°C) is easily identified by the presence of high-frequency (~100 Hz) oscillations associated with the separation of vapor bubbles from the upper part of a vapor cavity. Since the separation frequency is high and the vapor film is thick, the time-average temperature of the sensor does not noticeably vary.

As the liquid temperature decreases to 93°C,[1] the separation frequency decreases to about 20 Hz. With the further decrease in temperature, the self-oscillating regime of heat transfer is almost instantaneously established on the heater, where each bubble is formed from one second to tens of minutes (Figs. 1–3). This behavior indicates that the rearrangement of the heat-transfer regime is critical in the temperature of the liquid, because the transition from one regime to another occurs in a very narrow temperature interval (<0.1°C). In one oscillation period, the heater temperature varies in the interval 650–1200°C, according to visual estimates.

As the temperature of the liquid decreases, the period of oscillations increases until the emission of vapor from the film surface to the bulk of the liquid ceases at a temperature of 80–81°C. Thus, the disappearance of the self-oscillating regime of heat transfer and the transition to steady film boiling occur smoothly (Fig. 2). As temperature decreases further, a single domain of the film regime occupies a symmetric position with respect to the heater. The shape and size of the bubble do not then vary until a minimum achieved liquid temperature of 35°C.

If only one elementary (single) domain is realized on the heater, the critical temperatures, as well as the form of oscillations and their period, from which the temperature of the liquid can be estimated with a high accuracy, are completely reproduced in different experimental runs. However, when the heater length exceeds the size of the single domain of the film regime, the behavior is more complex. Even when the temperature of the liquid is below the saturation temperature by 2–3°C, the formation of a dynamic structure begins on the heater. This structure consists of several single domains, one of which has sizes characteristic for this regime, and the remaining domains are in a suppressed state. The sizes of the latter domains only slightly exceed the heater diameter, and vapor is not emitted on the surface. When vapor is separated from the vapor-film surface, the structure is rearranged, and one of previously suppressed domains can become the dominating domain. The regular pattern of thermograms disappears, and oscillations take a complicated form. The coordinate of the point corresponding to the maximum temperature moves periodically over the wire surface.

[1] For a given heater diameter, this temperature is reproduced in different experimental runs within an accuracy of about ±0.5°C.

*Institute of Problems of Chemical Physics, Russian Academy of Sciences, Chernogolovka, Moscow oblast, 142432 Russia*

** e-mail: zhukov@cat.icp.ac.ru*

1028-3358/03/4805-0235$24.00 

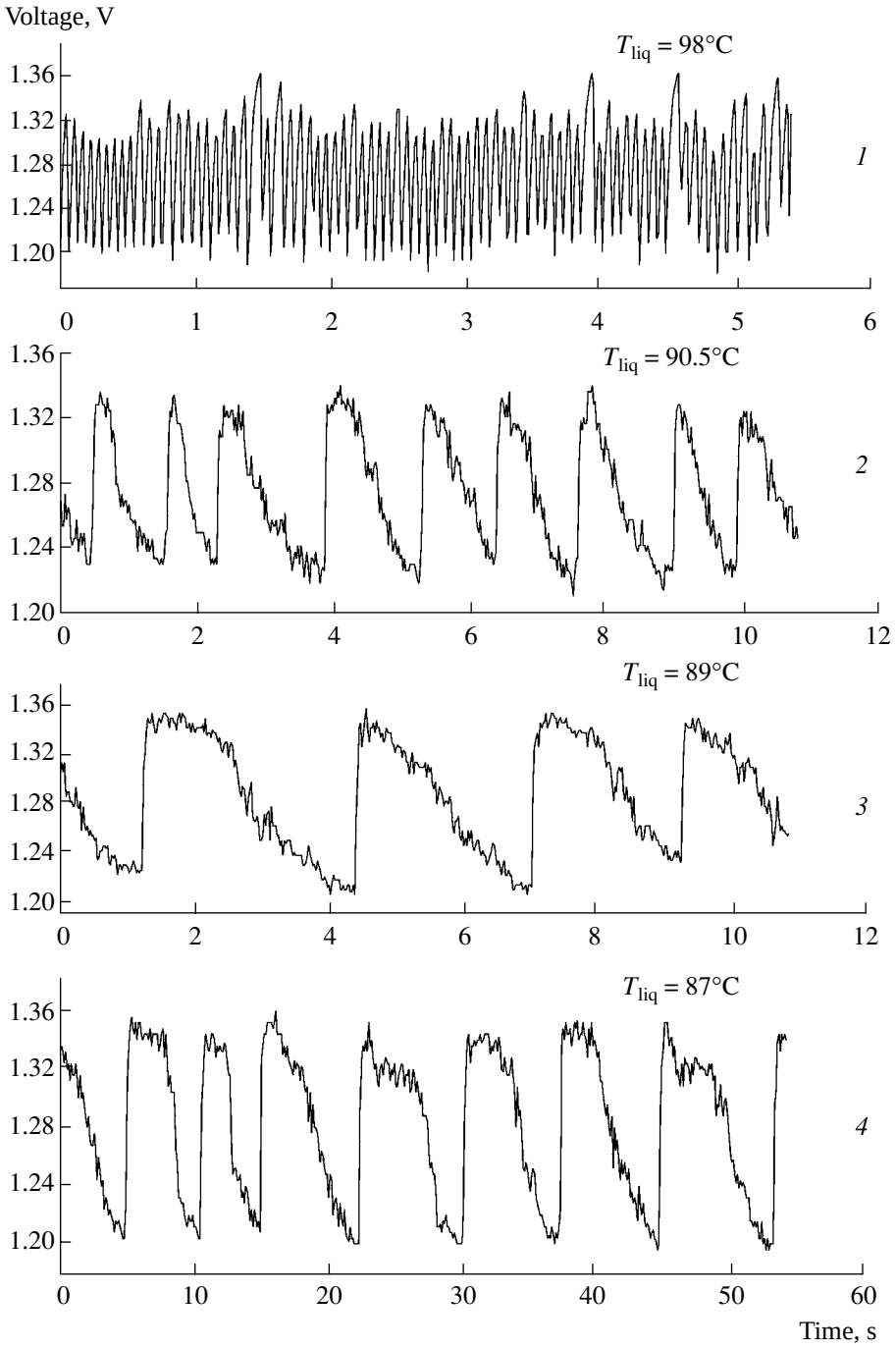


**Fig. 1.** Time scans of the voltage on the 1-mm-long sensor for the temperature of the liquid $T_{liq}$ = (from top to bottom) 98, 90.5, 89, and 87°C.

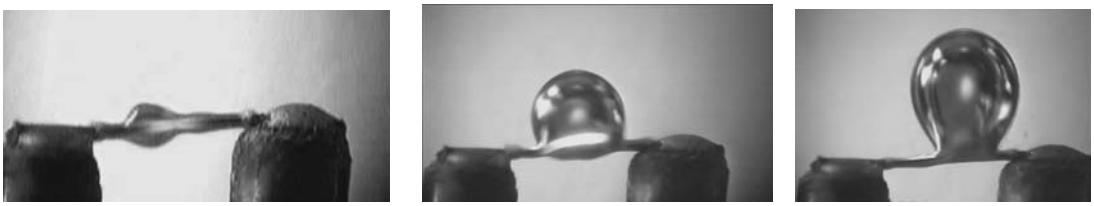

**Fig. 2.** Pictures of oscillations.

Thus, the heater exhibits indications characteristic for a spatially distributed system.

A steady symmetric vapor structure is formed on longer heaters below 93°C. This structure consists of one large elementary domain located at the center of the heater and several suppressed domains located on both sides of the central domain. Vapor is separated only in the central part of the structure. As the temperature of water decreases to 89°C, the film disappears through the autowave process.

The observed phenomena are completely reproducible. When the temperature of the liquid increases to $T_{sat}$, the structure of the domain becomes homogeneous again; i.e., all elementary domains have an identical size.

To determine the properties of interaction between elementary domains, experiments were carried out with heater lengths 1, 2, 4, 8, 12, 24, and 48 mm. The results can be briefly formulated as follows.

(i) Heaters with different lengths behave identically if the water temperature is maintained near the saturation temperature.

(ii) As the heater length increases, it is more difficult to separate the self-oscillating-instability region in an average-integrated signal, the amplitude of oscillations decreases, and they become more chaotic. A 24-mm-long sensor can already be considered as infinitely long.

(iii) As the temperature of the liquid decreases by 3–4°C below $T_{sat}$, the formation of a structure begins on short heaters. This structure consists of several dominating domains located at the center of the film-boiling region and a system of suppressed domains located at the edge of this region symmetrically with respect to the central part.

The effect of the diameter and material of the heater on the above properties was tested in experiments with heaters of diameters 50 and 200 μm. The phenomena are reproduced on any wire heaters (Fig. 2). Experiments with wires whose resistance is virtually independent of temperature corroborate that the observed effects are not attributed to the thermal sensors used as heaters. The phenomena observed on platinum samples were also reproduced on 0.1-mm sensors made of the high-resistivity Kh27Yu5T (Chromal) alloy.

In our opinion, the formation of ordered structures on small domains is attributed to the existence of mass flows along the heat-releasing surface within the film. These flows arise due to the dependence of pressure within a single domain on its size. Therefore, a system of a limited number of domains, which are originally identical and joined with each other through vapor channels, is unstable. A random fluctuation in the sizes of one domain is developed due to the positive pressure feedback. Pressure in a larger domain is lower than in surrounding domains, and vapor generated in neighboring domains flows to this larger domain. As the process

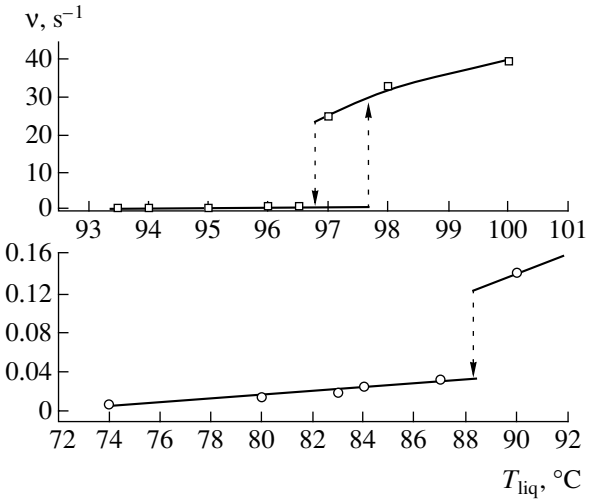


**Fig. 3.** Bubble separation frequency ν vs. the temperature of the liquid $T_{liq}$ for a heater diameter of (top) 50 and (bottom) 200 μm.

develops, pressure within donor domains increases, while sizes and, therefore, the heater temperature under them decrease. Therefore, the film structure on a small heater is rearranged, and a temperature-inhomogeneous regime involving domains of various sizes is finally established.

We suppose that structures similar to those observed on short wires must also exist on long heaters. A film part that adjoins the bubble regime and is in a colder region must have characteristics different from those for the central part of the film. Therefore, the formation of a system of suppressed domains must begin at the interface of the film regime. This gives rise to the fundamental rearrangement of the structure of this part of the film. As a result, a region where temperature is lower than temperature in the central region and is primarily determined by hydrodynamic factors arises in this part of the heater.

According to our observations, the processes described above occur on long heaters as the temperature of water decreases to 93–94°C (Fig. 4). For 0.1-mm-diameter heaters at $T_{liq} = T_{sat}$, the length of "cold ends," where temperature decreases from $T_{film}$ to $T_{bub}$, is less than 0.5 mm. At the same time, videotaping shows that the length of the region from the end of luminosity to the visible boundary of the film is equal to about 6–8 mm for $T_{liq} = 90$°C. Film boiling in this part of the heater is realized as a system of domains decreasing in size. This structure is naturally much less stable than the central part of the film.[2] It is the decomposition of this structure that is responsible for the premature destruction of the film. This is corroborated by our experiments with short sensors. A low-temperature structure cannot be realized on a heater whose size is

[2] This is probably due to narrowing of a vapor channel joining suppressed domains, which weakens mass exchange.

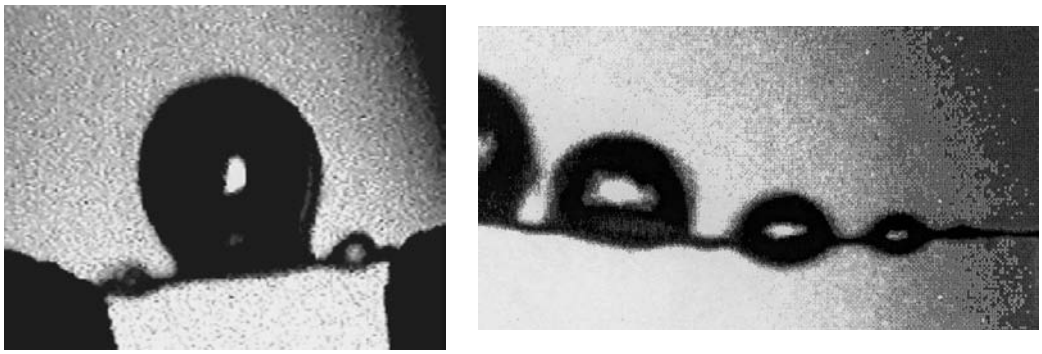

**Fig. 4.** Pictures of the film boiling structure on (left panel) a short wire ($L$ = 2.5 mm) and (right panel) at the end of a long wire.

commensurate with the elementary-domain size. Therefore, the elementary domain remains stable for any subcooling of the liquid.

A mechanism of origin of self-oscillating instability in the boiling of chemically reacting liquids was described in [1]. It is applicable with small refinements for the case under consideration. It is assumed that the heater temperature oscillates due to the change of the conduction mechanism of heat transfer in a film to the convection mechanism. Convective flows arise when a vapor film moves to the upper part of the heater under the action of the buoyancy force, and the liquid evaporates into a very thin vapor layer remaining at the bottom. The produced vapor passes through the narrow channel to the upper part of the vapor dome, where it condensates. Estimates show that, due to the narrowness of the vapor channel, the velocity of the flow can achieve about 10 m/s, which significantly increases the heat-transfer coefficient. In contrast to organic liquids, where gaseous reaction products constitute a considerable part of the flow and oscillations exist over the entire subcooling region, the self-oscillating regime in water can be realized only in a narrow interval of parameters, where the rates of evaporation and condensation are approximately equal to each other.

## ACKNOWLEDGMENTS

This work was supported by the Russian Foundation for Basic Research, project nos. 01-02-1723 and 03-01-32075.

## REFERENCES

1. S. A. Zhukov, V. A. Rafeev, and S. Yu. Afanas'ev, Dokl. Akad. Nauk **390** (2), 183 (2003) [Dokl. Phys. **48**, 221 (2003)].

*Translated by R. Tyapaev*

*Doklady Physics, Vol. 48, No. 5, 2003, pp. 239–243. Translated from Doklady Akademii Nauk, Vol. 390, No. 1, 2003, pp. 46–50.*


**MECHANICS**

# New Type of the Cumulation of the Energy and Momentum of Plates and Shells Accelerated by Explosions

**S. I. Zonenko and Academician G. G. Chernyĭ**

Received January 17, 2003

The instability of the interface between two deformable media, in particular the instability of the free surface of a deformable medium, has been studied for a long time in numerous investigations.

The problem of the stability of various material layers under the dynamic action of bulk and surface forces is a specific branch of this field of research. The following cases can serve as examples: the behavior of a horizontal layer of a magnetic fluid after switching on a magnetic field opposite to the direction of gravity [1] and the formation of periodic structures at the interface between two high-velocity metallic plates undergoing an oblique collision under explosive welding [2].

The instability of cylindrical shells expanding under the action of intense pressure waves traveling inside them and the formation of azimuthally periodic structures at the shell surfaces were observed in [3], where the schematic view of a shell before its fracture and expansion and corresponding photographs were presented. However, the authors did not analyze their findings and estimated only the axisymmetric deformation of the shell under high internal pressure produced by an explosion. The mechanical model accepted in [3] will be discussed and used below.

In experiments [4] with high-velocity lead plates impinging normally on fixed plates (made of steel or other metals), localized axisymmetric structures with typical cone-shaped splashes of the target material were observed. In the case of a 2-mm-thick lead plate with a velocity of about 500 m/s, the transverse dimension $\lambda$ of the axisymmetric structure was several times larger than the thickness of the accelerated plate (6, 5, and 8 mm for steel, copper, and titanium plates, respectively), while the height-to-diameter ratio for the splashes was equal to about 0.5.

The papers mentioned above revealed the formation of localized and periodic structures that significantly change the initially unperturbed surface of a deformable medium. A needle-shaped structure ("hedgehog") at the outer surface of a thick water shell before its decomposition into drops was observed by K.I. Kozorezov (personal communication) under conditions similar to those of the experiment reported in [3].

The well-known classical works on the stability of the interface between two different fluids in the gravity field analyzed the problem in the linear approximation (the Rayleigh–Taylor instability of a fluid over a lighter one). The nonlinear evolution of perturbations was analyzed in later papers. It was shown that the concavities of an initial small sine perturbation at such an interface are transformed into "fingers" growing with acceleration. At the same time, there are "bubbles" emerging upwards with a velocity tending to a constant value.[1]

Similar structures were also studied for an interface perturbed in two directions when three-dimensional periodic structures were formed.

In this paper, we consider the stability of a flat fluid layer against long-wave perturbations (i.e., the perturbation wavelength is much larger than the initial layer thickness) for a layer moving under the action of a constant pressure drop on its surfaces. The formation and development of a very unusual periodic structure at the layer surface were observed. Our analysis was performed within the framework of the simplest "forceless" model used previously in [3].

The theoretical results were used to carry out experiments with copper plates accelerated by explosions and to interpret the experimental results concerning the interaction of the plates with metallic targets.

A new mechanism of cumulation of the energy and momentum of a moving plate was found. This mechanism is due to the dynamical instability of the plate when its material can be treated as a liquid medium. For certain practical applications, this cumulation mechanism can have significant advantages over the well-known and widely used method of forming fast cumulative jets in oblique collisions of plates.

In connection with the problem under consideration, we mention paper [5], where the stability of a flat layer accelerated by a constant pressure drop on its surfaces was considered within the framework of a linearized

*Institute of Mechanics, Moscow State University, Michurinskiĭ pr. 1, Moscow, 119192 Russia*

[1] S.Ya. Gertsenshteĭn, V.M. Chernyavskiĭ, and Yu.M. Shtemler, *On the Rayleigh–Taylor Instability*, Preprint of Institute of Mechanics, Moscow State University, no. 49-99 (Moscow, 1999).

1028-3358/03/4805-0239$24.00 

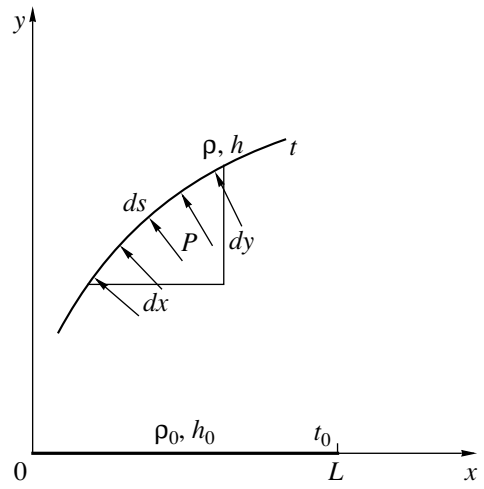


**Fig. 1.** Element of a deformed plate accelerated by an explosion.

model of potential motion of a perfect incompressible fluid. The authors found that the layer surfaces are unstable to arbitrary harmonic perturbations, because the perturbation amplitude increases exponentially with time (the perturbations certainly remain harmonic). In this case, the perturbation growth rate increases with decreasing wavelength. As was shown in that paper, the allowance for surface tension suppressing the shortest wavelength perturbations makes it possible to determine the wavelength of the fastest growing perturbation. The same result was obtained when the elastic properties of the medium were approximately taken into account.

We now derive the equations of motion of a layer. Let us assume that the thickness of the layer is much less than both the linear sizes of its surface and the characteristic range of the perturbation under consideration. This implies that the layer can be treated as a moving material surface subjected to mass and surface forces. We use the simplest model of the layer, where its strength properties are ignored; i.e., we suppose that each element of the moving layer is subjected to only mass forces and forces applied to its surfaces, and forces in the cross-sections of the layer are neglected.

To complete the model, we assume that the collision of the layer with an impermeable surface is completely inelastic; i.e., the relative momentum component tangential to the surface is conserved, while the normal component is absorbed. In particular, two colliding layers form a united layer with summed mass and momentum. In this case, the total kinetic energy is certainly transformed into the heat energy of the layer.

To simplify calculations, we consider only the two-dimensional case.

Let us consider the forces acting upon an element *ds* of the layer (Fig. 1).

In accordance with the problem formulated above, we allow for only pressure forces, assuming pressure in front of the layer to be constant. The excess pressure on the back of the layer is denoted by *p*. In this case, the equations of motion of the layer take the form

$$\rho h ds \frac{\partial^2 x}{\partial t^2} = -p dy, \quad \rho h ds = \frac{\partial^2 y}{\partial t^2} = p dx. \qquad (1)$$

Here, $x$ and $y$ are the Cartesian coordinates of a layer point; $t$ is the time; and $\rho$ and $h$ are the density and thickness of the layer, respectively.

The condition of mass conservation yields the equation

$$\rho h ds = \rho_0 h_0 d\xi = dm. \qquad (2)$$

Here, the subscript 0 stands for the initial values of the corresponding quantities and $\xi$ is the Lagrangian coordinate of the layer point (i.e., the initial value of the coordinate $s$). The quantities $\rho_0$ and $h_0$ can be functions of $\xi$. The mass coordinate $m$ can be used instead of $\xi$.

Since these equations will be used in the problem of the acceleration of an initially flat homogeneous plate, we take $\rho_0$ and $h_0$ as constants, with $\xi$ being an initial value of $x$. The plate size is denoted by $L$. To simplify our calculations, we consider only the case of $p$ = const. We divide coordinates $x$, $y$, $s$, and $\xi$ by $L$, thickness $h$ by $h_0$, and time $t$ by $\sqrt{\frac{\rho_0 h_0 L}{p}}$. In this case, Eqs. (1) and (2) take the dimensionless form without parameters:

$$\frac{\partial^2 x}{\partial t^2} = -\frac{\partial y}{\partial \xi}, \quad \frac{\partial^2 y}{\partial t^2} = \frac{\partial x}{\partial \xi}, \qquad (3)$$

$$\frac{1}{h} = \frac{\partial s}{\partial \xi} = \sqrt{\left(\frac{\partial x}{\partial \xi}\right)^2 + \left(\frac{\partial y}{\partial \xi}\right)^2}. \qquad (4)$$

After finding the dependences $x = x(\xi, t)$ and $y(\xi, t)$ from Eqs. (3), we determine the layer thickness $h(\xi, t)$ from Eq. (4).

Equation (3) has the simple solution

$$x = \xi, \quad y = \frac{t^2}{2}, \qquad (5)$$

corresponding to an undeformed plate uniformly accelerated from rest at $t = 0$.

Equations (3) and (4) are invariant under the transformation to the reference frame fixed to the moving undeformed plate. These equations are linear equations with constant coefficients. Under the given boundary $[x(0, t) = 0, x(1, t) = 1]$ and initial $[x(\xi, 0) = x_0(\xi), y(\xi, 0) = y_0(\xi), \frac{\partial x}{\partial t} = \dot{x}_0(\xi), \frac{\partial y}{\partial t} = \dot{y}_0(\xi)]$ conditions, the general solution of the problem of an accelerated plate (material surface) can be found as an eigenfunc-

tion expansion. It is easy to verify that the eigenfunctions of the problem have the form

$$x = e^{\pm\sqrt{n\pi}t}\sin(n\pi\xi), \quad y = e^{\pm\sqrt{n\pi}t}\cos(n\pi\xi),$$
$$x = e^{\pm\sqrt{n\pi}t}\cos(n\pi\xi), \quad y = e^{\pm\sqrt{n\pi}t}\sin(n\pi\xi), \qquad (6)$$
$$n = 1, 2, \ldots.$$

It is worth noting that Eqs. (3) and the superpositions of their solutions (6) describe arbitrary finite perturbations of the layer under consideration, in contrast to solutions of the linearized problem of perturbed motion of a finite-thickness layer [5], which are applicable only for small perturbations.

In order to avoid the cumbersome calculations required for considering the evolution of arbitrary initial perturbations, which must be expressed as series in eigenfunctions (6), we consider only the following simple solution satisfying the initial conditions given above:

$$x = \xi + \varepsilon\sin(2\pi\xi), \quad y = \frac{1}{2}t^2 + \varepsilon\cos(2\pi\xi), \qquad (7)$$

where $\varepsilon = \varepsilon_0\exp\sqrt{2\pi}t$. For $t = 0$ and $\varepsilon \longrightarrow 0$, the perturbed plate has the evidently harmonic shape

$$y = \varepsilon\cos(2\pi x), \quad h = 1 - \varepsilon\cdot 2\pi\cos(2\pi x) + O(\varepsilon^2).$$

We now trace its evolution. The plate profile $y' = y - \frac{1}{2}t^2 = y'(x, t)$ is shown in Fig. 2 in variables $x$ and $\frac{y}{\varepsilon}$ for $\varepsilon \longrightarrow 0$ (cosine curve), $\varepsilon = 0.05, 0.1, \frac{1}{2\pi}, 0.25, 0.5$, and 1 (in what follows, the prime is omitted). At the time $t$ corresponding to $\varepsilon = \frac{1}{2\pi}$, a cusp $x = \frac{1}{2}$ $\left(\xi = \frac{1}{2}\right)$ originates on the curve $y = y(x)$ so that the left and right sections of the deformed layer begin to approach each other. In view of the mirror symmetry of the problem, it is sufficient to consider only the left half with $\xi \in \left[0, \frac{1}{2}\right]$.

Let $\xi^*$ and $t^*$ denote the values of $\xi$ and $t$ corresponding to the starting point of the collapse. After a layer section collapses, the pressures on its sides become identical. Therefore, under the above assumption that an impact is inelastic, any point of this section moves inertially along the $x = \frac{1}{2}$ line from its position $y = y^*(t)$ at the impact instant, and its velocity is equal

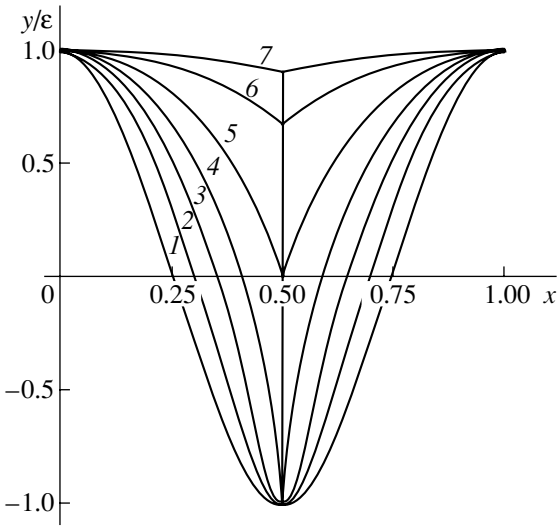


**Fig. 2.** Plate profile and the finger formed for times corresponding to (*1*) $\varepsilon \longrightarrow 0$ and $\varepsilon =$ (*2*) 0.05, (*3*) 0.1, (*4*) $\frac{1}{2\pi}$, (*5*) 0.25, (*6*) 0.5, and (*7*) 1.

to the $y$ component of its velocity at the impact instant. Therefore, this motion is described by the equation

$$y = y^* + \left.\frac{\partial y}{\partial t}\right|_{\substack{\xi = \xi^* \\ t = t^*}} (t - t^*)$$

or

$$y = \varepsilon^*\cos(2\pi\xi^*)\left(1 + \ln\frac{\varepsilon}{\varepsilon^*}\right). \qquad (8)$$

Thus, beginning with the time corresponding to $\varepsilon = \frac{1}{2\pi}$, a finger begins to grow at $x = \frac{1}{2}$ behind the layer front exponentially accelerated relative to the linearly accelerated reference frame. The growing finger is first in the $y < 0$ region, because the initial velocities of the middle section with $\xi \in \left[\frac{1}{4}, \frac{3}{4}\right]$ are negative due to the initial conditions. Beginning with $\varepsilon = \frac{1}{4}$, the maximum velocity of the finger end directed backwards is equal to $-\frac{1}{\sqrt{2\pi}}$, and the finger extends into the $y > 0$ region, while the velocity of the leading end of the finger (at the intersection point of the left and right sections of the layer) increases exponentially with time.

Using Eqs. (7), we determine the following relations between $\xi^*$, $y^*$, and $t^*$ (or $\varepsilon^*$):

$$\frac{1}{2} = \xi^* + \varepsilon^*\sin(2\pi\xi^*),$$
$$y^* = \varepsilon^*\cos(2\pi\xi^*) = \left(\frac{1}{2} - \xi^*\right)\cot(2\pi\xi^*). \qquad (9)$$

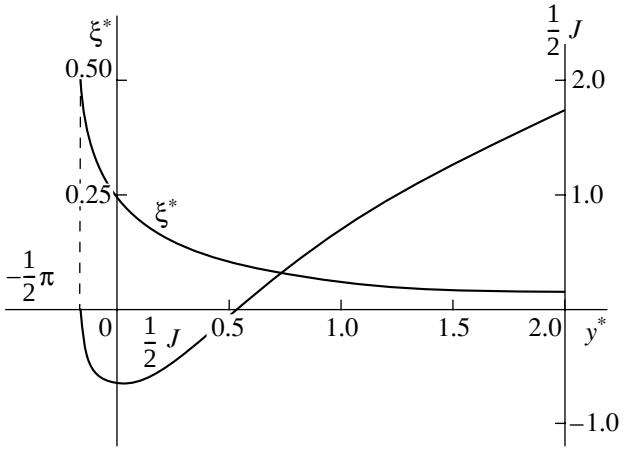


**Fig. 3.** Mass and momentum of a finger vs. $y^*$ (time $t^*$).

**Fig. 4.** Craters produced in a steel target by fingers formed on an accelerated plate.

These dependencies are presented in Fig. 3, which shows how an initial $\xi$ distribution linear in the $x$ coordinate of an unperturbed plate varies when the plate is gradually transformed into the finger in the $y$ direction. At the same time, the mass of the $\xi \in \left[\frac{1}{4}, \frac{3}{4}\right]$ ($y < 0$) half of the plate is concentrated in the slowly moving finger section (relative to the linearly accelerated coordinate system). The other half, with $\xi \in \left[0, \frac{1}{4}\right]$ and $\xi \in \left[\frac{3}{4}, 1\right]$, i.e., $y > 0$, is gradually concentrated in the finger section accelerated exponentially with time.

It is easy to evaluate the total momentum $J$ of the finger under the conditions described above:

$$\frac{1}{2}J = \sqrt{2\pi}\int_{\varepsilon^*}^{1/2} \varepsilon(\xi^*)\cos(2\pi\xi^*)d\xi^*.$$

The momentum $J$ as a function of $y^*$ is also shown in Fig. 3.

As has already been mentioned, the scale of the fastest growing perturbations cannot be determined in the model presented above.

Analyzing our experiments with circular copper plates accelerated by explosions, we found, in addition to ordinary irregularities, barely visible circular dents symmetrically distributed over a circle at the bottom of a shallow crater formed on the steel target. By analogy with the instability of liquid layers described above, which results in the development of periodic finger-shaped structures, we suppose that the same effect can occur in the case under consideration; i.e., instability can give rise to the formation of periodic structures (fingers). This consideration was the starting point of the theory presented above.

The launcher that was used in our experiments was a thin-walled cylinder with a height of ~9 cm and a diameter of ~4.5 cm. The upper half of the cylinder was filled with a ~100-g explosive on a 0.2-cm-thick copper plate. According to the model described above, initial perturbations for a launching pressure of about 100 kbar have increased by a factor of several thousands before the accelerated plate impinges upon the target under the cylinder. This suggests that high-velocity finger-shaped periodic structures can originate in our experiments.

In order to increase the perturbation growth rate in a plate, we attempted to preset its initial deformation such that it corresponded to a sufficiently developed evolution stage. The result exceeded all our expectations. Indeed, the theory under consideration and, therefore, the predicted shape of a moving layer are approximate. Moreover, following the model accepted above, we should reproduce the initial velocity profile as well as the initial shape of the accelerated plate. However, this is impossible in our experiments. Nevertheless, after a few trials, we found that presetting a periodic perturbation with six periods (this number was established experimentally) led to the result predicted by the theory; namely, six deep craters originated on the target (Fig. 4). In the case of four-period initial deformation of the plate, the symmetry of the craters was broken, so that two of them are each split into two craters. In order words, the development of finger-shaped structures tends to form just six fingers.

Ordered structures were also observed in our experiments, where a copper cylindrical shell with small longitudinal bulges regularly distributed on its inner surface was compressed by an explosion-induced detonation wave traveling along the outside of the shell.

Between longitudinal hollows caused by the impact of the shell bulges, circular dents uniformly distributed over a cylindrical target, which was coaxially placed

within the shell, were distinctly observed. It is reasonable to suppose that these dents are formed by sufficiently large periodic perturbations.

The discovered development of small perturbations, which is accompanied by energy–momentum cumulation in finger-shaped structures, was used to design an explosion unit for making deep grooves in a metal and for perforating thick metallic plates. In this case, the areas of craters or holes approach the cross area of a launched plate or the whole launcher.

Comparative experiments indicated that the usual axisymmetric combination of central and annular cumulative jets requires a significantly greater amount of explosive and a launcher with a larger diameter to achieve the same results.

## REFERENCES

1. É. Ya. Blum, M. M. Maĭorov, and A. O. Tzebers, *Magnetic Fluids* (Zinatne, Riga, 1989), pp. 192–199.
2. A. A. Deribas, *Physics of Strengthening and Welding by Explosion* (Nauka, Moscow, 1981).
3. V. A. Odintsov and L. A. Chudov, in *Mechanics* (Mir, Moscow, 1975), No. 5, pp. 85–154.
4. I. V. Yakovlev, Fiz. Goreniya Vzryva, No. 3, 447 (1973).
5. V. M. Kuznetsov and E. N. Sher, Prikl. Mekh. Tekh. Fiz., No. 2, 66 (1964).

*Translated by V. Chechin*

*Doklady Physics, Vol. 48, No. 5, 2003, pp. 244–246. Translated from Doklady Akademii Nauk, Vol. 390, No. 2, 2003, pp. 196–199.*


**MECHANICS**

# Axisymmetric Plastic Flow of a Bilayer Material through a Conical Channel

**S. E. Aleksandrov* and G. S. Mishuris****

Presented by Academician A.Yu. Ishlinskiĭ November 25, 2002

Received November 29, 2002

Solutions to problems of plasticity theory for piecewise-homogeneous materials are of significant interest for the analysis and design of metal-forming processes of composite materials. However, these solutions can qualitatively differ from the corresponding solutions for homogeneous materials. Therefore, defects arising when composite materials are fabricated can significantly differ from defects arising when homogeneous materials are fabricated. Defects arising when composite materials are fabricated were reviewed in [1]. Moreover, when the plastic flow of piecewise-homogeneous materials is studied, it is necessary to take into account the fact that the constitutive laws can be different for different domains [2].

Classical problems of plasticity theory for piecewise-homogeneous materials are of interest for revealing the main features of solutions. Such solutions were obtained in [3–5] for flow through infinite channels and compression between parallel plates. In particular, planar and axisymmetric flow of multilayer plastic materials in converging channels was considered in [3]. However, in this paper, based on the assumption that friction is low, the solution was found in the vicinity of the trivial frictionless solution. As was shown in [4] for planar flow, such an approach can provide qualitatively incorrect results for some boundary conditions. In this paper, the results obtained in [4] are generalized to the case of the axisymmetric flow of a bilayer plastic material through an infinite conical channel. The solution is based on the corresponding solution for the flow of a homogeneous material through an infinite channel [6]. Note that flow through infinite converging conical channels for other models of the material, including rotating channels, was analyzed in [7–10]. The method used in [3] was also applied in [10].

The flow of a bilayer material through a conical channel is illustrated in Fig. 1. It is assumed that each material is rigid/perfectly plastic and meets the von Mises criterion. However, the yield stresses of the materials are different. In the spherical coordinate system $\rho\varphi\theta$ shown in Fig. 1, the channel surface is defined by the equation $\varphi = \alpha$. Friction on this surface is determined by the law

$$\sigma_{\rho\varphi} = m_w k_e, \tag{1}$$

where $\sigma_{\rho\varphi}$ is the shear stress in the spherical coordinate system ($\sigma_{\rho\rho}$, $\sigma_{\varphi\varphi}$, and $\sigma_{\theta\theta}$ will denote the respective normal stresses), $k_e$ is the shear yield stress of the outer material ($k_i$ will denote the shear yield stress of the inner material), and $m_w$ is the friction factor lying in the interval $0 \le m_w \le 1$. We assume that the bimaterial interface is defined by the equation (Fig. 1)

$$\varphi = \gamma. \tag{2}$$

The quantity $\gamma$ should be determined from the solution. We assume that there is sliding at the bimaterial inter-

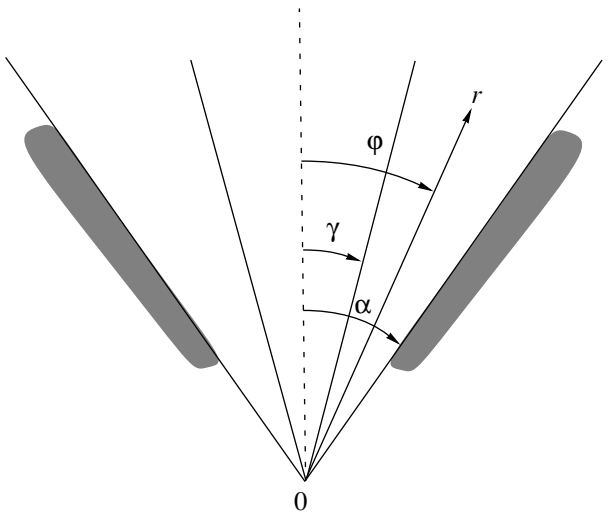


**Fig. 1.**

* *Institute for Problems in Mechanics, Russian Academy of Sciences, pr. Vernadskogo 101, Moscow, 119526 Russia*
*e-mail: salex@ipmnet.ru*

** *Department of Mathematics, Rzeszow University of Technology, W. Pola 2, Rzeszow, 35-959 Poland*

1028-3358/03/4805-0244$24.00 © 2003 MAIK “Nauka/Interperiodica”

face and that the friction law takes the form

$$\sigma_{\rho\varphi} = \pm m_b k_{\min}, \quad (3)$$

where $k_{\min} = \min\{k_i, k_e\}$ and $m_b$ is the friction factor at the bimaterial interface, $0 \le m_b \le 1$. The upper sign in (3) corresponds to the case where the velocity of the inner material is higher than the velocity of the outer material at the bimaterial interface. On the axis of symmetry, $\varphi = 0$, the natural condition

$$\sigma_{\rho\varphi} = 0 \quad (4)$$

is satisfied. Since the flow is assumed to be radial, all the kinematic boundary conditions are automatically satisfied.

In [6], the solution to the problem of the flow of a homogeneous rigid/perfectly plastic material with the shear yield stress $k$ through a converging conical channel reduces to the solution of the first-order ordinary differential equation

$$\frac{d\tau}{d\varphi} + \tau\cot\varphi + 2\sqrt{3}(1-\tau^2)^{1/2} = c_0, \quad (5)$$

where $\tau = \dfrac{\sigma_{\rho\varphi}}{k}$ and $c_0$ is an arbitrary constant. Once the solution to Eq. (5) has been found, the normal stresses and the radial velocity $u$ are determined from the equations

$$\sigma_{\varphi\varphi} = \sigma_{\theta\theta} = \sigma_{\rho\rho} - \sqrt{3}k(1-\tau^2)^{1/2} = k(A_0 - c_0\ln\rho) - 3k\int\tau d\varphi, \quad (6)$$

$$u = -\frac{B_0}{\rho^2}\exp[-2\sqrt{3}\int\tau(1-\tau^2)^{-1/2}d\varphi], \quad (7)$$

where $A_0$ and $B_0$ are arbitrary constants, which remain undetermined in the case of the flow through an infinite channel.

For the flow of the bilayer material, the solution given by Eqs. (5)–(7) is valid in each layer, assuming that $k = k_i$ in the inner layer and $k = k_e$ in the outer layer. In addition, the constants can have different values in each material layer. We denote $c_0 = c_i$, $A_0 = A_i$, and $B_0 = B_i$ in the inner material and $c_0 = c_e$, $A_0 = A_e$, and $B_0 = B_e$ in the outer material. Because the contact stresses must be continuous across the bimaterial interface, it follows from (6) that

$$c_e = sc_i = sc, \quad (8)$$

where $s = \dfrac{k_i}{k_e}$. It is also convenient to introduce the new variable $\psi$ such that $\tau = \sin 2\psi$. Then, Eq. (5) with the use of Eq. (8) takes the form

$$2\sin\varphi\cos 2\psi\frac{d\psi}{d\varphi} + \cos\varphi\sin 2\psi + 2\sqrt{3}\sin\varphi\cos 2\psi = c\sin\varphi \quad (9)$$

at $0 \le \varphi \le \gamma$ and

$$2\sin\varphi\cos 2\psi\frac{d\psi}{d\varphi} + \cos\varphi\sin 2\psi + 2\sqrt{3}\sin\varphi\cos 2\psi = sc\sin\varphi \quad (10)$$

at $\gamma \le \varphi \le \alpha$. The boundary conditions (1), (3), and (4) in terms of the function $\psi$ have the form

$$\psi = \frac{1}{2}\arcsin m_w \quad (11)$$

at $\varphi = \alpha$,

$$\psi = \pm\frac{1}{2}\arcsin\left(\frac{m_b k_{\min}}{k_e}\right) \quad (12)$$

at $\varphi = \gamma + 0$,

$$\psi = \pm\frac{1}{2}\arcsin\left(\frac{m_b k_{\min}}{k_i}\right) \quad (13)$$

at $\varphi = \gamma - 0$,

$$\psi = 0 \quad (14)$$

at $\varphi = 0$. The sign in Eqs. (12) and (13) is determined in the same way as in Eq. (3). In order to satisfy these four conditions, there are two constants of integration of Eqs. (9) and (10), $c$ and $\gamma$. The existence and uniqueness of the solution of this boundary-value problem depend substantially on $s$, the sign in Eqs. (12) and (13), and the friction factors $m_w$ and $m_b$. It is possible to show that the general structure of the solution is similar to the case of planar flow [4]. This structure is illustrated in Figs. 2 and 3. Figure 2 shows the case where the velocity of the inner material is higher than the velocity of the outer material at the bimaterial interface. The solution is unique in domain *3*, two solutions exist in domain *2*, and there is no solution in domain *1*. The solution is unique at the boundary *OA* and does not exist at the boundary *ABC*. It is possible to show that the point *A* is located below the line $s = (1 + m_b^2)^{-1/2}$. Figure 3 shows the case where the velocity of the outer material is higher than the velocity of the inner material at the bimaterial interface. There are two solutions in domain *2*, and there is no solution in domain *1*. The solution is unique at the boundary *AB*. It is possible to

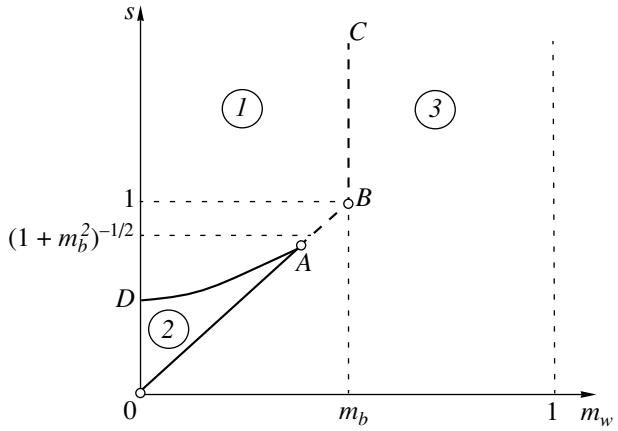


**Fig. 2.**

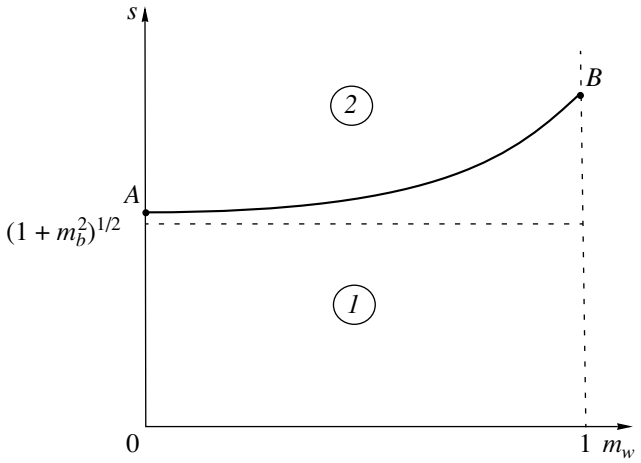


**Fig. 3.**

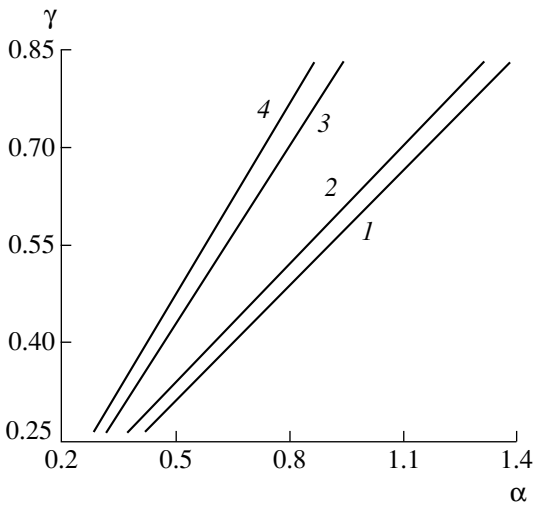


**Fig. 4.**

show that the point $A$ is located above the line $s = (1 + m_b^2)^{1/2}$. It is necessary to note that the structure of the solution at $m_b = 0$ corresponds neither to the structure shown in Fig. 2 nor to the structure shown in Fig. 3. Nevertheless, the properties of this solution can be described by means of Fig. 3. The line $AB$ keeps its shape but intersects the axis at $s = 1$. A unique solution excluding the axis $s$ exists above this line, and there is no solution below the line. In addition, no solution exists on the line $AB$ and the $s$ axis. The point $A$ ($m_w = 0$, $s = 1$) is an exception corresponding to the solution $\psi = 0$ at $0 \le \varphi \le \alpha$. The special solution at $m_b = 0$ shows that small changes in $m_b$ near $m_b = 0$ can lead to qualitative changes in the behavior of the solution. For this reason, the analysis performed in [3, 10] can lead to incorrect results.

The dependence of $\gamma$ on $\varphi$ is of a certain practical interest, because it can be used to approximately analyze some technological processes [11]. This dependence, found from a numerical solution of Eqs. (9) and (10) with the boundary conditions (11)–(14) for the $s$ values [$s$ = (*1*) 0.65, (*2*) 0.7, (*3*) 0.8, and (*4*) 0.9), is shown in Fig. 4 for the case where the velocity of the inner material is higher than the velocity of the outer material at the bimaterial interface and the solution is unique. It was assumed that $m_w = m_b = 1$ under the conditions (11) and (12).

The solution for the flow of a homogeneous material satisfying Tresca's yield condition was also obtained in [6]. This solution reduces to Eq. (5) with different numerical coefficients. Therefore, its generalization to the flow of a piecewise-homogeneous material can be obtained in the same manner as in the case of the von Mises condition.

## REFERENCES

1. W. Johnson and S. K. Ghosh, J. Mater. Sci. **16**, 285 (1981).
2. R. Sliwa, Mater. Sci. Eng. A **135**, 259 (1991).
3. D. Durban, Int. J. Solids Struct. **20** (7), 649 (1984).
4. S. Alexandrov, G. Mishuris, and W. Miszuris, Eur. J. Mech. A/Solids **19** (5), 811 (2000).
5. S. Alexandrov, G. Mishuris, and W. Miszuris, Arch. Appl. Mech. **71** (8), 555 (2001).
6. R. T. Shield, J. Mech. Phys. Solids **3** (4), 246 (1955).
7. N. Cristescu, Int. J. Mech. Sci. **17**, 425 (1975).
8. D. Durban, Trans. ASME: J. Appl. Mech. **46** (2), 322 (1979).
9. D. Durban, *Drawing of Viscoplastic Tubes through Rotating Conical Dies. Computational Methods for Predicting Material-Processing Defects* (Elsevier, Amsterdam, 1987), pp. 93–102.
10. D. Durban, G. Davidi, and D. Lior, Trans. ASME: J. Appl. Mech. **68** (6), 894 (2001).
11. S. Alexandrov, G. Mishuris, W. Miszuris, and R. E. Sliwa, in *Proceedings of 8th International Conference on Metal Forming* (Balkema, Rotterdam, 2000), p. 649.

*Translated by S. Aleksandrov*

*Doklady Physics, Vol. 48, No. 5, 2003, pp. 247–252. Translated from Doklady Akademii Nauk, Vol. 390, No. 3, 2003, pp. 337–342.*


**MECHANICS**

# Parametrically Controlled Quasi-Harmonic Regimes of Self-Oscillations and Forced Oscillations: Removal of Plurality

**M. Ya. Izrailovich**

Presented by Academician K.V. Frolov January 28, 2003

Received December 30, 2002

For exciting and damping self-oscillations and forced oscillations, additive controlling actions are most frequently used. However, parametric controlling schemes are also sometimes used [1–6], because schemes with a parametric active action are more easily realizable in some cases. At the same time, parametric control often allows the realization of those useful properties of closed systems that are more difficult to realize with additive control. In particular, a relay parametric control of self-oscillations makes it possible to obtain approximately optimal laws invariant with respect to nonlinearity of the pure elastic or pure dissipative type [7].

However, many periodic regimes are possible in systems with a parametric control, as well as in periodic regimes of systems without active controlling actions and systems with an additive control. This means that regimes different from the calculated optimal regime can exist in a synthesized system, which can give rise to a negative effect in some cases. In particular, when solving the problem of active vibration damping, regimes that differ from the calculated regime and have higher intensities than in the original uncontrolled system can arise in the controlled system.

This paper presents a method for constructing quasi-optimal parametric controls for both autonomous systems and systems with an external periodic excitation for stationary regimes of quasi-harmonic systems. The desired controlling functions are bounded in either the $L^p(0; 2\pi)$ space or the $M(0; 2\pi)$ space. In the first approximation of asymptotic methods [8], we obtain linear isoperimetric conditions imposed on the desired controlling actions. Optimizing functions are then determined by the method of moments [9]. Further, based on a generalization of the principle of construction of the extended (multiplicative stabilizing) control, which was proposed in [10] for systems with the additive control, we construct extended parametric controls, which are artificial attractors with arbitrary attraction to the nominal (quasi-optimal) limit cycle. The resulting controls are proven to ensure the uniqueness and stability of the nominal limit cycle.

*Blagonravov Institute of Mechanical Engineering, Russian Academy of Sciences, M. Khariton'evskiĭ per. 4, Moscow, 101830 Russia*

## 1. CONSTRUCTION OF CONTROLS FOR PERIODIC REGIMES OF AUTONOMOUS SYSTEMS

We consider the periodically controlled quasi-harmonic autonomous system

$$\ddot{x} + \omega_0^2 x = \varepsilon[f(x, \dot{x}) + ux], \tag{1}$$

where $\varepsilon$ is a small parameter, $u$ is the desired controlling action, and $f(x, \dot{x})$ is a given nonlinear characteristic.

Let the functional $J(x, \dot{x})$ characterize the intensity of stationary oscillations of system (1) and the intensity of the control be restricted by the condition

$$\left[\int_0^{2\pi/\omega} |u|^p dt\right]^{\frac{1}{p}} \le U_p, \tag{2}$$

where $1 \le p < \infty$, $\omega$ is the given frequency of self-oscillations such that $\omega^2 - \omega_0^2$ is equal to about $\varepsilon$, and $U_p$ is the constant characterizing the limit control resource. Inequality (2) for $p \longrightarrow \infty$ corresponds to the restriction on the amplitude of the controlling action.

We have to find $u^*(x, \dot{x})$ providing a maximum (or minimum) of the functional $J(x, \dot{x})$ in a stationary regime with a frequency of $\omega$. The problem of the maximization of the periodic-regime intensity corresponds to the synthesis of the generation system for self-oscillations, and the problem of minimization corresponds to the reduction of the level of noise self-oscillations. In the latter case, it is assumed that the nonlinear characteristic $f(x, \dot{x})$ corresponds to the characteristic of the self-oscillating type.

1028-3358/03/4805-0247$24.00 

After the change of variables

$$x = A\cos\psi, \quad \dot{x} = -\omega_0 A\sin\psi, \quad \psi = \omega_0 t + \varphi$$

and further averaging of the right-hand side of Eq. (1), we obtain the following set of first-approximation equations of the asymptotic method [8]:

$$\dot{A} = \frac{\varepsilon}{2\pi\omega_0}\left[\Phi(A) - \frac{1}{2}Au_1\right], \tag{3}$$

$$\dot{\varphi} = -\frac{\varepsilon}{2\pi\omega_0 A}\left[\Psi(A) + \frac{1}{2}Au_2\right]_{2\pi}, \tag{4}$$

where

$$\Phi(A) = -\int_0^{2\pi} f(A\cos\psi - \omega_0 A\sin\psi)\sin\psi d\psi,$$

$$\psi(A) = \int_0^{2\pi} f(A\cos\psi, -\omega_0 A\sin\psi)\cos\psi d\psi,$$

$$u_1(A) = \int_0^{2\pi} u\sin 2\psi d\psi, \quad u_2 = \int_0^{2\pi} u\cos 2\psi d\psi.$$

From Eq. (4), we obtain the frequency-squared expression

$$\omega^2 = \omega_0^2 - \frac{\varepsilon}{\pi A}\left[\psi(A) + \frac{1}{2}Au_2\right] \tag{5}$$

accurate to $\varepsilon^2$.

Since $\dot{A} = 0$, $\dot{\varphi} = 0$ for a stationary regime, Eqs. (3) and (5) provide the following isoperimetric conditions that are imposed on the desired function $u$:

$$\int_0^{2\pi} u\sin 2\psi d\psi = \beta_1(A), \quad \int_0^{2\pi} u\cos 2\psi d\psi = \beta_2(A), \tag{6}$$

where

$$\beta_1(A) = \frac{2\Phi(A)}{A},$$

$$\beta_2(A) = \frac{2[\pi(\omega_0^2 - \omega^2) - \varepsilon\Psi(A)]}{\varepsilon A}.$$

After the change of variables, the functional $J(x, \dot{x})$, which must be optimized, transforms to a function of the variable $A$. In what follows, this function is assumed to increase monotonically. In particular, for the square functional,

$$J = \int_0^{2\pi/\omega} (x^2 + \alpha\dot{x}^2)dt \simeq \frac{\pi}{\omega}(1 + \alpha^2\omega^2)A^2.$$

Therefore, the minimization and maximization of the functional $J$ are equivalent to the minimization and maximization of the amplitude $A$.

We now consider the following auxiliary problem (which is of interest itself). Let $A$ be given. It is necessary to find the function $u_0(\psi)$ that satisfies Eqs. (6) (moment relations) and has the minimum norm

$$I_p = \left(\int_0^{2\pi/\omega} |u|^p dt\right)^{\frac{1}{p}} = \frac{1}{\omega^{1/p}}\left(\int_0^{2\pi} |u|^p d\psi\right)^{\frac{1}{p}}. \tag{7}$$

According to [9], the solution of this problem has the form

$$u_0(\psi) = \frac{1}{l^q}\left|\varepsilon_1^0\sin 2\psi + \varepsilon_2^0\cos 2\psi\right|^{q-1} \times \operatorname{sgn}(\varepsilon_1^0\sin 2\psi + \varepsilon_2^0\cos 2\psi), \tag{8}$$

where $\frac{1}{q} + \frac{1}{p} = 1$ and $\varepsilon_1^0$ and $\varepsilon_2^0$ are determined by solving the extreme problem

$$\min_{\varepsilon_1, \varepsilon_2}\left(\int_0^{2\pi} |\varepsilon_1\sin 2\psi + \varepsilon_2\cos 2\psi|^q d\psi\right)^{\frac{1}{q}} = \frac{1}{l^q} \tag{9}$$

under the condition $\beta_1\varepsilon_1 + \beta_2\varepsilon_2 = 1$. In this case, $l^{-1}$ is equal to the minimum norm (7); i.e., $l^{-1} = I_p(u_0)$.

Transforming the left-hand side of Eq. (9) as

$$\min_{\varepsilon_1, \varepsilon_2}\sqrt{\varepsilon_1^2 + \varepsilon_2^2}\left[\int_0^{2\pi} |\sin(2\psi + \psi_1)|^q d\psi\right]^{\frac{1}{q}} = \min_{\varepsilon_1, \varepsilon_2}\sqrt{\varepsilon_1^2 + \varepsilon_2^2}M_q, \tag{10}$$

where

$$M_q = \left[\int_0^{2\pi} |\sin(2\psi + \psi_1)|^q d\psi\right]^{\frac{1}{q}} = \left(\int_0^{2\pi} |\sin 2\psi|^q d\psi\right)^{\frac{1}{q}};$$

we determine the minimizing $\varepsilon_1^0$ and $\varepsilon_2^0$ values in the form

$$\varepsilon_1^0 = \frac{\beta_1}{\beta_1^2 + \beta_2^2}, \quad \varepsilon_2^0 = \frac{\beta_2}{\beta_1^2 + \beta_2^2}. \tag{11}$$

According to Eqs. (10), (11), and (6), the minimum control intensity is related to the regime parameters $A$ and $\omega$ as

$$\sqrt{\beta_1^2 + \beta_2^2} = M_q(I_p^0)^q\omega^{q/p}. \tag{12}$$

The original problem of the maintenance of the maximum (or minimum) amplitude $A^*$ corresponds to the limit intensity of the controlling action. Therefore,

replacing $I_p^0$ with $U_p$ on the right-hand side of Eq. (12) in accordance with restriction (2), we arrive at the equation

$$\omega^{\frac{q}{p}}\frac{2\varepsilon A}{\pi}M_q U_p^q = \left\{\frac{\varepsilon^2\Phi^2(A)}{\pi^2} + \left[(\omega_0^2-\omega^2)A - \varepsilon\frac{\psi(A)}{\pi}\right]^2\right\}^{\frac{1}{2}}. \quad (13)$$

The optimal amplitude $A^*$ is determined as the maximum or minimum root of Eq. (13). From Eq. (8) with allowance for Eqs. (11)–(13), we obtain the corresponding function $u^*$

$$u^*(\psi) = U_p^q\left|\beta_1^*\sin 2\psi + \beta_2^*\cos 2\psi\right|^{q-1} \times \operatorname{sgn}(\beta_1^*\sin 2\psi + \beta_2^*\cos 2\psi), \quad (14)$$

where

$$\beta_1^* = \beta_1(A^*), \quad \beta_2^* = \beta_2(A^*).$$

Since $x = A^*\cos\psi$ and $\dot{x} = -\omega_0 A^*\sin\psi$, the function $u^*(x, \dot{x})$ is determined from Eq. (14) as

$$u^*(x,\dot{x}) = U_p^q\left|-2\beta_1^*\frac{x\dot{x}}{\omega_0} + \beta_2^*\left(x - \frac{\dot{x}^2}{\omega_0^2}\right)\right|^{q-1} \times (A^*)^{-2(q-1)}\operatorname{sgn}\left[-2\beta_1^*\frac{x\dot{x}}{\omega_0} + \beta_2^*\left(x^2 - \frac{\dot{x}^2}{\omega_0^2}\right)\right]. \quad (15)$$

## 2. ANALYSIS OF REGIMES OF CLOSED SELF-OSCILLATING SYSTEMS: MULTIPLICATIVE STABILIZING CONTROL

For set (1) with parametric control (15), truncated Eqs. (3) and (4) have the form

$$\dot{A} = \frac{\varepsilon}{2\pi\omega_0}\left[\Phi(A) - \frac{1}{2}Au_1^*(A)\right], \quad (16)$$

$$\dot{\varphi} = -\frac{\varepsilon}{2\pi\omega_0}\left[\psi(A) + \frac{1}{2}Au_2^*(A)\right], \quad (17)$$

where

$$u_1^*(A) = \int_0^{2\pi} u^*(A\cos\psi, -\omega_0 A\sin 2\psi)\sin 2\psi\, d\psi,$$

$$u_2^*(A) = \int_0^{2\pi} u^*(A\cos\psi, -\omega_0\sin\psi\, d\psi)\cos 2\psi\, d\psi,$$

and $u^*$ is given by Eq. (15).

We assume that the following two cases are possible for set (1) with control (15).

(i) There are $n$ limit cycles; i.e., in accordance with Eq. (16), the equation

$$\Phi(A) - \frac{1}{2}Au_1^*(A) = 0 \quad (18)$$

has $n-1$ positive roots $A_i$, $i = 1, 2, \ldots, n-1$ in addition to the $A^*$ root corresponding to the nominal regime, which can be either stable or unstable; i.e., the inequality

$$\dot{\Phi}(A) - \frac{1}{2}u_1(A) - \frac{1}{2}A\dot{u}_1(A) < 0 \quad (19)$$

for $A = A^*$ can be either satisfied or unsatisfied in view of Eq. (16).

(ii) There is the unique limit cycle $A^*$; i.e., Eq. (18) has one positive solution $A^*$; however, the regime is unstable; i.e., inequality (19) is unsatisfied for $A = A^*$.

To remove the plurality of regimes and to stabilize the regime $A^*$ (if it is unstable), the originally determined control (15) is replaced by the extended (multiplicative stabilizing) control

$$u_{\text{ms}} = \chi(A, A^*)u^*(x, \dot{x}), \quad (20)$$

where $\chi(A, A^*) = 1 + \rho\sigma(A, A^*)$, $A = \left(x^2 + \frac{\dot{x}^2}{\omega_0^2}\right)^{\frac{1}{2}}$ is the amplitude determined in terms of phase coordinates, $\sigma(A, A^*)$ is a continuously differentiable function such that

$$\sigma(A^*, A^*) = 0, \quad \frac{\partial}{\partial A}\sigma(A^*, A^*) \neq 0,$$

and $\rho$ is a constant.

When $u^*(x, \dot{x})$ given by Eq. (15) is replaced by the control $u_{\text{ms}}$ given by (20), Eq. (18) and inequality (19) for $A = A^*$ take the form

$$\Phi(A) - \frac{1}{2}A\chi(A, A^*)u_1^*(A) = 0, \quad (21)$$

$$\dot{\Phi}(A^*) - \frac{1}{2}u_1^*(A^*) - \frac{1}{2}\rho A^*\frac{\partial}{\partial A}\sigma(A^*, A^*)u_1^*(A^*) - \frac{1}{2}A^*\dot{u}_1^*(A^*) < 0. \quad (22)$$

**Theorem 1.** *There are functions $\sigma(A, A^*)$ belonging to the class defined above and values of the parameter $\rho(-\infty < \rho < \infty)$ such that Eq.* (21) *has the unique solution $A = A^*$ and inequality* (22) *is satisfied.*

As an example, we consider set (1) with the nonlinearity

$$f = f_0\operatorname{sgn}\dot{x} + |\dot{x}|\dot{x}.$$

In this case, $\omega = \omega_0$, restriction (2) is given in the form $|u| \le U$, and $\Phi(A) = a_0 + a_1A^2$, where $a_0 = 4f_0$ and

$a_1 = \frac{8}{3}\omega_0^2$. According to Eq. (15), the parametric control providing the maximum amplitude of self-oscillations has the form

$$u^*(x, \dot{x}) = -U\operatorname{sgn} x\dot{x}. \quad (23)$$

The corresponding amplitude of self-oscillations has the form

$$A^* = \frac{\pi U}{2a_1} + \left[\left(\frac{\pi U}{2a_1}\right)^2 - \frac{a_0}{a_1}\right]^{\frac{1}{2}} \quad (24)$$

for $U > \frac{2\sqrt{a_0 a_1}}{\pi}$ (excitation condition).

Equation (18) has two solutions: $A_1 = A^*$, given by Eq. (24), and $A_2 = \frac{\pi U}{2a_1} - \left[\left(\frac{\pi U}{2a_1}\right)^2 - \frac{a_0}{a_1}\right]^{\frac{1}{2}}$. Therefore, the system involves the nominal regime $A^*$ (24) and the regime with lower amplitude $A_2$. In this case, stability condition (19) has the form $2a_1A - \pi U < 0$. Therefore, the regimes $A^*$ and $A_2$ are unstable and stable, respectively. For this reason, $u^*$ given by Eq. (23) is replaced by extended control (20) given in the form

$$u_{\text{ms}} = [1 + \rho(A - A^*)]u^*.$$

In this case, Eq. (21) takes the form

$$a_0 + a_1A^2 - A[1 + \rho(A - A^*)]\pi U = 0,$$

which degenerates to a linear equation for $\rho = \frac{a_1}{\pi U}$ and has the unique solution $A = A^*$. The regime $A^*$ is stable, because

$$-(1 - \rho A^*)\pi U = \left(\frac{1}{2} + \sqrt{\frac{1}{4} - \frac{a_0 a_1}{\pi^2 U^2}} - 1\right)\pi U < 0$$

in view of inequality (22).

## 3. CONSTRUCTION OF VIBRATION DAMPING CONTROLS FOR FORCED PERIODIC REGIMES

We consider the quasi-harmonic system

$$\ddot{x} + \omega_0^2 x = \varepsilon[f(x_1\dot{x}) + B\sin\omega t + ux], \quad (25)$$

where $B\sin\omega t$ is the external perturbation, whose frequency $\omega$ differs from $\omega_0$ by a value of about $\varepsilon$. According to [8], the first-approximation equations for $A$ and $\varphi$ have the form

$$\dot{A} = \varepsilon\left[\frac{\Phi(A)}{2\pi\omega} - \frac{B}{\omega + \omega_0}\cos\varphi - \frac{1}{2}\frac{A}{2\pi\omega}u_1\right],$$
$$\dot{\varphi} = \omega_0 - \omega - \frac{\varepsilon}{2\pi\omega A}\Psi(A) + \frac{\varepsilon B}{(\omega + \omega_0)A}\sin\varphi - \frac{1}{2}\frac{\varepsilon}{2\pi\omega}u_2. \quad (26)$$

Stationary-regime equations determined from Eq. (26) for $\dot{A} = 0$, $\dot{\varphi} = 0$ have the form

$$X(A, \varphi) = \varepsilon\Phi(A) - \varepsilon\pi B\cos\varphi - \varepsilon\frac{A}{2}u_1 = 0,$$
$$Y(A, \varphi) = \Psi_1(A) + \varepsilon\pi B\sin\varphi - \varepsilon\frac{A}{2}u_2 = 0, \quad (27)$$

where $\Psi_1(A) = \pi(\omega_0^2 - \omega^2)A - \varepsilon\Psi(A)$.

Equations (27) provide the following moment relations imposed on the desired function $u$:

$$\int_0^{2\pi} u\sin 2\psi d\psi = \gamma_1(A, \varphi),$$
$$\int_0^{2\pi} u\cos 2\psi d\psi = \gamma_2(A, \varphi), \quad (28)$$

where

$$\gamma_1(A, \varphi) = \frac{2}{A}[\Phi(A) - \pi B\cos\varphi],$$
$$\gamma_2(A, \varphi) = \frac{2}{A}\left[\frac{\Psi_1(A)}{\varepsilon} + \pi B\sin\varphi\right].$$

We have to find $u^*(\psi)$ and phase $\varphi^*$ that satisfy conditions (28) and provide the minimum amplitude $A^*$ under restriction (2). To solve this problem, the following auxiliary problem is first considered. The function that satisfies moment relations (28) and has minimum norm $I_p$ (7) must be found for given $A$ and $\varphi$ values. This problem is solved similarly to the problem described above for autonomous systems. As a result, by analogy with Eq. (12), the equation relating $I_p^0$ to the regime parameters $A$ and $\varphi$ is found in the form

$$\omega^{q/p}M_q[I_p^0(A, \varphi)]^q = [\gamma_1^2(A, \varphi) + \gamma_2^2(A, \varphi)]^{\frac{1}{2}}. \quad (29)$$

Further, we determine the phase $\varphi^0(A)$ providing the minimum intensity $I_p^0(A, \varphi)$ (29). Since

$$\gamma_1^2(A, \varphi) + \gamma_2^2(A, \varphi) = \frac{4}{A^2}[|D(A)|^2 - 2|D(A)|\pi B\cos(\varphi + \varphi_1) + \pi^2 B^2],$$

$$|D(A)| = \left[\Phi^2(A) + \frac{\Psi_1^2(A)}{\varepsilon^2}\right]^{\frac{1}{2}},$$

$$\cos\varphi_1 = \frac{\Phi(A)}{|D(A)|}, \quad \sin\varphi_1 = \frac{\Psi_1(A)}{\varepsilon|D(A)|},$$

we have

$$\cos\varphi^0(A) = \frac{\Phi(A)}{|D(A)|}, \quad \sin\varphi^0(A) = -\frac{\Psi_1(A)}{\varepsilon|D(A)|}. \quad (30)$$

Substituting $\varphi = \varphi^0(A)$ given by Eq. (30) into Eq. (29) and replacing $I_p^0$ with the limit control intensity $U_p$, we arrive at the following equation for the amplitude:

$$\omega^{q/p} M_q U_p^q = \frac{2}{A}|D(A)| - \pi B. \quad (31)$$

The minimum amplitude $A^*$ is determined as the least positive root of Eq. (31). In view of Eqs. (30), parameters $\gamma_1[A, \varphi^0(A)]$ and $\gamma_2[A, \varphi^0(A)]$ for $A = A^*$ are given by the formulas

$$\gamma_1^* = \frac{2\Phi(A^*)}{A^*}\left[1 - \frac{\pi B}{|D(A^*)|}\right],$$

$$\gamma_2^* = \frac{2\Psi_1(A^*)}{\varepsilon A^*}\left[1 - \frac{\pi B}{|D(A^*)|}\right].$$

According to Eq. (15), the replacement of $\beta_1^*$ and $\beta_2^*$ by $\gamma_1^*$ and $\gamma_2^*$ leads us to the function of parametric vibration damping with feedback

$$u^*(x, \dot{x}) = U_p^q\left[-2\gamma_1^*\frac{x\dot{x}}{\omega} + \gamma_2^*\left(x^2 - \frac{\dot{x}^2}{\omega^2}\right)\right] \times A^{*-2(q-1)}\operatorname{sgn}\left[-2\gamma_1^*\frac{x\dot{x}}{\omega} + \gamma_2^*\left(x^2 - \frac{\dot{x}^2}{\omega^2}\right)\right], \quad (32)$$

providing the minimum amplitude $A^*$.

## 4. ANALYSIS OF REGIMES OF SYSTEMS WITH A VIBRATION-DAMPING ACTION: MULTIPLICATIVE–STABILIZING CONTROL

Regimes different from the minimum-amplitude regime can also exist in system (25) with parametric vibration-damping control (32). Stationary regimes are analyzed by analyzing the set of equations (27), where $u_1$ and $u_2$ must be replaced by

$$u_1^*(A) = \int_0^{2\pi} u^*(A\cos\psi, -\omega A\sin\psi)\sin 2\psi\, d\psi$$

and

$$u_2^*(A) = \int_0^{2\pi} u^*(A\cos\psi, -\omega A\sin\psi)\sin 2\psi\, d\psi,$$

respectively. According to Eq. (32), $u^*(x, \dot{x})$ in these formulas is determined by the equations

$$X(A, \varphi) = \varepsilon\Phi(A) - \varepsilon\pi B\cos\varphi - \varepsilon\frac{A}{2}u_1^*(A) = 0,$$
$$Y(A, \varphi) = \Psi_1(A) - \varepsilon\pi B\sin\varphi - \varepsilon\frac{A}{2}u_2^*(A) = 0. \quad (33)$$

Excluding the phase $\varphi$ from Eqs. (33), we arrive at the following equation for amplitudes:

$$\left[\Phi(A) - \frac{A}{2}u_1^*(A)\right]^2 + \left[\frac{\Psi_1(A)}{\varepsilon} - \frac{A}{2}u_2^*(A)\right]^2 = \pi^2 B^2. \quad (34)$$

Stability conditions for forced-oscillation regimes have the form [8]

$$A\dot{X}_A + \dot{Y}_\varphi < 0, \quad \dot{X}_A\dot{Y}_\varphi - \dot{X}_\varphi\dot{Y}_A > 0, \quad (35)$$

where $\dot{X}_A$, $\dot{X}_\varphi$, $\dot{Y}_A$, $\dot{Y}_\varphi$ are the derivatives calculated from Eqs. (33) for arguments $A$ and $\varphi$ corresponding to the regime under consideration. The substitution of thus calculated derivatives transforms conditions (35) to the form

$$A\dot{\Phi}(A) - \frac{A^2}{2}\dot{u}_1^*(A) - \frac{A}{2}u_1^*(A) + \Phi(A) - \frac{A}{2}u_1^*(A) < 0, \quad (36)$$
$$\varepsilon^2\left[\Phi(A) - \frac{A}{2}u_1^*(A)\right] \times \left[\dot{\Phi}(A) - \frac{1}{2}u_1^*(A) - \frac{A}{2}\dot{u}_1^*(A)\right] + \left[\Psi_1(A) - \frac{\varepsilon}{2}Au_2^*(A)\right] \times \left[\dot{\Psi}_1(A) - \frac{\varepsilon}{2}u_2^*(A) - \frac{\varepsilon A}{2}\dot{u}_2^*(A)\right] > 0.$$

Similar to the case of autonomous systems, it is assumed that either Eq. (34) has $n - 1$ positive solutions in addition to the solution $A^*$ or the solution $A^*$ is unique. However, inequalities (36) are not satisfied for

$A = A^*$. For this reason, the originally determined quasi-optimal control $u^*(x, \dot{x})$ given by Eq. (32) is replaced by the extended control

$$u_{ms} = \chi(A, A^*)u^*(x, \dot{x}), \qquad (37)$$

where $u^*(x, \dot{x})$ is control (32) and the structure of $\chi(A, A^*)$ is the same as that for autonomous systems. With $u_{ms}$ (37), Eq. (34) takes the form

$$\left[\dot{\Phi}(A) - \frac{A}{2}\chi(A, A^*)u_1^*(A)\right]^2$$

$$+ \left[\frac{\Psi_1(A)}{\varepsilon} - \frac{A}{2}\chi(A, A^*)u_2^*(A)\right]^2 = \pi^2 B^2. \qquad (38)$$

Stability conditions (36) for $A = A^*$ transform to

$$A^*\dot{\Phi}(A^*) - \frac{A^{*2}}{2}\dot{u}_1^* A - \frac{A^{*2}}{2}\rho\frac{\partial\sigma}{\partial A}(A^*, A^*)u_1^*(A^*)$$

$$- \frac{A^*}{2}u_1^*(A^*) + \Phi(A^*) - \frac{A^*}{2}u_1(A^*) < 0, \qquad (39)$$

$$\varepsilon^2\left[\Phi(A^*) - \frac{A}{2}u_1^*(A^*)\right]$$

$$\times\left[\dot{\Phi}(A^*) - \frac{1}{2}u_1^*(A^*) - \frac{A^*}{2}\dot{u}_1^*(A)\right.$$

$$\left. - \frac{A^*}{2}\rho\frac{\partial}{\partial A}\sigma(A^*, A^*)u_1^*(A^*)\right]$$

$$+ \left[\Psi_1(A^*) - \frac{\varepsilon}{2}u_1^*(A^*)\right]$$

$$\times\left[\dot{\Psi}_1(A^*) - \frac{\varepsilon}{2}u_1^*(A^*) - \frac{\varepsilon A^*}{2}\dot{u}_2^*(A^*)\right.$$

$$\left. - \frac{\varepsilon A^*}{2}\frac{\partial}{\partial A}\sigma(A^*, A^*)u_2(A^*)\right] > 0.$$

**Theorem 2.** *There are functions* $\sigma(A, A^*)$ *belonging to the class defined above and values of the parameter* $\rho(-\infty < \rho < \infty)$ *such that Eq.* (38) *has the unique solution* $A = A^*$ *and inequality* (39) *is satisfied.*

## ACKNOWLEDGMENTS

This work was supported by the Russian Foundation for Basic Research, project no. 00-01-00217.

## REFERENCES

1. K. V. Frolov, Mashinovedenie, No. 3, 38 (1965).
2. M. E. Gerts, Mashinovedenie, No. 5, 10 (1982).
3. L. D. Akulenko, Izv. Akad. Nauk, Mekh. Tverd. Tela, No. 3, 18 (1993).
4. M. Ya. Izrailovich, Probl. Mashinostr. Nadezhnosti Mash., No. 4, 15 (1994).
5. M. Ya. Izrailovich, Probl. Mashinostr. Nadezhnosti Mash., No. 4, 20 (1996).
6. M. Ya. Izrailovich, Izv. Akad. Nauk, Mekh. Tverd. Tela, No. 3, 54 (1997).
7. M. Ya. Izrailovich, Dokl. Akad. Nauk **376**, 751 (2000).
8. N. N. Bogolyubov and Yu. A. Mitropol'skiĭ, *Asymptotic Methods in the Theory of Nonlinear Oscillations* (Fizmatgiz, Moscow, 1963; Gordon & Breach, New York, 1962).
9. A. G. Butkovskii, *Distributed Control Systems* (Nauka, Moscow, 1965; Elsevier, New York, 1969).
10. M. Ya. Izrailovich, Dokl. Akad. Nauk **377**, 25 (2001).

*Translated by R. Tyapaev*

*Doklady Physics, Vol. 48, No. 5, 2003, pp. 253–256. Translated from Doklady Akademii Nauk, Vol. 390, No. 3, 2003, pp. 343–346.*


**MECHANICS**

# Distributions of Fluctuations in Motion of the Earth's Pole

**Yu. G. Markov* and I. N. Sinitsyn****

Presented by Academician V.V. Kozlov February 19, 2003

Received February 21, 2003

**1.** According to observation data and measurements made by the International Earth Rotation Service in the last 15–20 years, motion of the Earth's pole involves a principal component (free nutation and Chandlers wobble) with an amplitude of 0.20″–0.25″ and a period of 433 ± 2 sidereal days [1], a regular annual component (365 sidereal days) with an amplitude of about 0.07″–0.08″, and a comparatively slow irregular drift (trend) of the axis of the Earth's figure. The annual wobbles of the Earth's axis are caused by the moment of gravitational forces of the Sun, the Earth's revolution around the Sun, and the diurnal tides of the mantle [2, 3]. The causes and mechanism of exciting the annual wobbles are usually attributed to seasonal geophysical phenomena [4, 5].

Measurements of motion of the Earth's pole were statistically analyzed in many works (see, e.g., [6]). Analytical stochastic spectrally correlation models of motion of the Earth's pole were developed in [7–9] on the basis of celestial mechanics.

In this paper continuing studies [7–9], we consider one-dimensional distributions of fluctuations in motion of the deformable Earth.

**2.** We now introduce the following notation and assumptions.

(i) The projections of the instantaneous angular velocity of the Earth's rotation on the Earth's axes are denoted by $Y = [Y_1 Y_2 Y_3]^T$, where $Y_1 = p_t$, $Y_2 = q_t$, and $Y_3 = r_t$.

(ii) We assume that the axial and centrifugal moments of inertia of the deformable Earth, $A = J_{pp}$, $B = J_{qq}$, $C = J_{rr}$, $J_{pq} = J_{qp}$, $J_{qr} = J_{rq}$, $J_{rp} = J_{pr}$, in the diurnal time interval $T_* = 2\pi r_*^{-1}$, $r_* = 365\omega_*$ can be represented in the form

$$J_{ij} = J_{ij}^* + J'_{ij,1}\sin r_* t + J''_{ij,1}\cos r_* t$$

$$+ J'_{ij,2}\sin 2r_* t + J''_{ij,2}\cos 2r_* t,$$

where higher harmonics are ignored and $i, j = p, q, r$.

(iii) We introduce the term "effective diurnal tidal humps" for the following dimensionless combinations of the axial moments of inertia:

$$u_1 = \langle (C-B)A^{*-1}\cos\varphi\rangle, \quad u_2 = \langle (C-A)B^{*-1}\sin\varphi\rangle,$$

$$u_3 = \langle (B-A)C^{*-1}\sin 2\varphi\rangle.$$

Here, $\langle\ldots\rangle$ means the averaging over the diurnal time interval $T_* = 2\pi r_*^{-1}$ ($\varphi = r_* t$), $u_1 \sim u_2$, and $u_3 \ll u_{1,2}$.

(iv) The dimensionless combinations of the centrifugal moments of inertia,

$$u_4 = \langle J_{qr}A^{*-1}\rangle, \quad u_5 = \langle J_{qr}C^{*-1}\sin\varphi\rangle,$$

$$u_6 = \langle J_{qr}A^{*-1}\cos 2\varphi\rangle, \quad u_7 = \langle J_{qr}B^{*-1}\sin 2\varphi\rangle,$$

$$u_8 = \langle J_{pr}B^{*-1}\rangle, \quad u_9 = \langle J_{pr}C^{*-1}\cos\varphi\rangle,$$

$$u_{10} = \langle J_{pr}B^{*-1}\cos 2\varphi\rangle, \quad u_{11} = \langle J_{pr}A^{*-1}\sin 2\varphi\rangle,$$

$$u_{12} = \langle J_{pq}C^{*-1}\rangle, \quad u_{13} = \langle J_{pq}A^{*-1}\sin\varphi\rangle,$$

$$u_{14} = \langle J_{pq}B^{*-1}\cos\varphi\rangle, \text{ and } u_{15} = \langle J_{pq}C^{*-1}\cos 2\varphi\rangle,$$

will be referred to as effective tidal protrusions averaged over the diurnal time interval $T_* = 2\pi r_*^{-1}$, where $u_{4\ldots7} \sim u_3$, $u_{8\ldots11} \ll u_{4\ldots7}$, and $u_{12\ldots15} \ll u_{8\ldots11}$.

(v) We allow for only the moments of gravitational forces of the Sun with respect to the Earth's axes [3]. It is important to note that the moment of gravitational forces of the Moon is larger than that of the Sun by a factor of 2–3. However, since the natural frequency differs significantly from the forcing frequency, the amplitude of monthly oscillations induced by the Moon is one twentieth to one fifteenth that of annual oscillations. Therefore, monthly oscillations of the Earth's pole are not manifested in observations.

* *Moscow State Aviation Institute (University of Aerospace Technology), Volokolamskoe sh. 4, Moscow, 125080 Russia*

** *Institute for Problems of Informatics, Russian Academy of Sciences, ul. Vavilova 30/6, Moscow, 117900 Russia*

1028-3358/03/4805-0253$24.00 © 2003 MAIK "Nauka/Interperiodica"

(vi) We allow for the external linear fluctuation–dissipation moments of forces: $M_1^{\mathrm{fd}} = V_{1t} - D_1 p_t$, $M_2^{\mathrm{fd}} = V_{2t} - D_2 q_t$, and $M_3^{\mathrm{fd}} = V_{3t} - D_3 r_t$, where $V_{1t}$, $V_{2t}$, and $V_{3t}$ are the specific moments of external random forces and $D_{1,2,3}$ are the specific coefficients of the moments of dissipative forces.

(vii) At last, $\mathcal{P} = \mathcal{P}(t, p_t, q_t, r_t, \mathbf{u}, \mathbf{V})$, $\mathcal{Q} = \mathcal{Q}(t, p_t, q_t, r_t, \mathbf{u}, \mathbf{V})$, and $\mathcal{R} = \mathcal{R}(t, p_t, q_t, r_t, \mathbf{u}, \mathbf{V})$ denote the specific moments of external perturbing forces, which depend on time, state vector, constant parameters $\mathbf{u} = [u_1 u_2 \ldots u_{n_1}]^{\mathrm{T}}$, and fluctuation parameters $\mathbf{V} = [V_{1t} V_{2t} V_{3t} \ldots V_{n_2 t}]^{\mathrm{T}}$, where $n_1, n_2 \geq 3$ are the dimensions of the vectors.

**3.** Under assumptions (i)–(vii), the equations of the Earth's motion have the form

$$\dot{p}_t + N_* q_t = \mathcal{P}_1 + \mathcal{P}_2 \mathbf{V}, \quad p_{t_0} = p_0, \tag{1}$$

$$\dot{q}_t - N_* p_t = \mathcal{Q}_1 + \mathcal{Q}_2 \mathbf{V}, \quad q_{t_0} = q_0, \tag{2}$$

$$\dot{r}_t = \mathcal{R}_1 + \mathcal{R}_2 \mathbf{V}, \quad r_{t_0} = r_0. \tag{3}$$

Here,

$$\mathcal{P}_1 = 3u_1 b\omega_*^2 \cos\omega_* t - \frac{3}{2}u_4\omega_*^2(1 - 3b_1^2\cos^2\omega_* t) - \frac{3}{2}u_6\omega_*^2(1 - b_1^2\cos^2\omega_* t) - \frac{3}{2}u_{11}\omega_*^2(1 - b_1^2\cos^2\omega_* t) + \frac{3}{2}u_{13}\omega_*^2 b\cos\omega_* t - u_4 r_t^2 - D_1 p_t, \tag{4}$$

$$\mathcal{P}_2 = V_{1t} + \overline{\mathcal{P}}_2(t, p_t, q_t, r_t, \mathbf{u}), \tag{5}$$

$$\mathcal{Q}_1 = -3u_2 b\omega_*^2 \cos\omega_* t + \frac{3}{2}u_7\omega_*^2(1 - b_1^2\cos^2\omega_* t) + \frac{3}{2}u_8\omega_*^2(1 - 3b_1^2\cos^2\omega_* t) - \frac{3}{2}u_{10}\omega_*^2(1 - b_1^2\cos^2\omega_* t) - 3u_{14} b\omega_*^2\cos\omega_* t + u_8 r_t^2 - D_2 q_t, \tag{6}$$

$$\mathcal{Q}_2\mathbf{V} = V_{2t} + \overline{\mathcal{Q}}_2(t, p_t, q_t, r_t, \mathbf{u})\mathbf{V}, \tag{7}$$

$$\mathcal{R}_1 = \frac{3}{2}u_3\omega_*^2(1 - b_1^2\cos^2\omega_* t) - \frac{3}{2}u_5 b\omega_*^2\cos\omega_* t + 3u_9 b\omega_*^2\cos\omega_* t + 3u_{15}\omega_*^2(1 - b_1^2\cos^2\omega_* t) - D_3 r_r, \tag{8}$$

$$\mathcal{R}_2\mathbf{V} = V_{3t} + \overline{\mathcal{R}}_2(t, p_t, q_t, r_t, \mathbf{u})\mathbf{V}. \tag{9}$$

In Eqs. (1)–(9), $N_* = (C^* - B^*)A^{*-1}\omega_*$, and $b$ and $b_1$ are dimensionless parameters such that $0.4 \leq b \leq \frac{4}{3}\pi^{-1}$ and $b_1 \approx b$ [3]. The quantities $u_{1\ldots3}$ and $u_{4\ldots15}$ are defined in (iii) and (iv). Terms involving the squares and products of $\mathbf{u}$, $p_t$, $q_t$, and $r_t - r_*$, as well as the averaged (over the time interval $T_*$) rates of variation of the axial and centrifugal moments of inertia, are omitted in the functions $\mathcal{P}_1$, $\mathcal{Q}_1$, and $\mathcal{R}_1$. The specific moments of external random and dissipative forces are denoted by $\mathcal{P}_2$, $\mathcal{Q}_2$, and $\mathcal{R}_2$; they are nonlinear in $\mathbf{u}$, $p_t$, $q_t$, and $r_t$ and depend on the parameters $\mathbf{V}$. When the fluctuation parameters $\mathbf{V}$ represent broadband Gauss–Markov processes similar to white noise, Eqs. (1)–(3) should be treated as nonlinear stochastic differential equations in the sense of θ-differentials [10, 11] (e.g., in the Stratonovich sense). For self-correlated Gaussian noise, Eqs. (1)–(3) should be completed by the equations for linear shaping filters [10, 11].

**4.** According to [10, 11], if the parameters $\mathbf{V}$ are Gaussian random variables with zero expectation and intensity matrix $\nu(t) = [\nu_{l,h}(t)]$ ($l, h = 1, 2, \ldots, n_2$), Eqs. (1)–(3) reduces to the Ito form

$$\dot{Y} = a(Y, t) + b(Y, t)V, \quad Y(t_0) = Y_0. \tag{10}$$

Here,

$$a = a(Y, t) = [a_1 a_2 a_3]^{\mathrm{T}} = \bar{a} + \frac{1}{2}\left[\left(\frac{\partial}{\partial\eta}\right)^{\mathrm{T}} b(Y, t)\nu(t)b(\eta, t)^{\mathrm{T}}\right]^{\mathrm{T}}_{\eta = Y}, \tag{11}$$

$$\bar{a} = \bar{a}(Y, t) = [\bar{a}_1\bar{a}_2\bar{a}_3], \quad \bar{a}_1 = -N_* q_t + \mathcal{P}_1, \quad \bar{a}_2 = N_* p_t + \mathcal{Q}_1, \quad \bar{a}_3 = \mathcal{R}_1, \tag{12}$$

$$b = b(Y, t) = \mathrm{diag}[\mathcal{P}_2, \mathcal{Q}_2, \mathcal{R}_2]. \tag{13}$$

As follows from Eq. (10), the Fokker–Planck–Kolmogorov equations for the nonstationary one-dimensional density $f_1 = f_1(y; t)$ and stationary density $f_1^* = f_1^*(y)$ have the form

$$\frac{\partial f_1}{\partial t} = -\frac{\partial^{\mathrm{T}}}{\partial y}(a f_1) + \frac{1}{2}\mathrm{tr}\left[\frac{\partial}{\partial y}\frac{\partial^{\mathrm{T}}}{\partial y}(\sigma f_1)\right], \tag{14}$$

$$-\frac{\partial^{\mathrm{T}}}{\partial y}(a f_1^*) + \frac{1}{2}\mathrm{tr}\left[\frac{\partial}{\partial y}\frac{\partial^{\mathrm{T}}}{\partial y}(\sigma^* f_1^*)\right] = 0, \tag{15}$$

where

$$\sigma = \sigma(y, t) = b(y, t)\nu(t)b(y, t)^{\mathrm{T}},$$
$$\sigma^* = b^*(y)\nu^*b^*(y)^{\mathrm{T}} \quad (\det\sigma, \det\sigma^* \neq 0). \tag{16}$$

Equations (14) and (15) are the basis for stochastic kinetic models of the Earth's motion under Gaussian nonlinear random–dissipative perturbations.

**5.** If both the dissipative matrix $D = \mathrm{diag}[D_1, D_2, D_3]$ and the inertia tensor $\mathcal{T} = \mathrm{diag}[A, B, C]$ are constant and the moments of gravitational forces have the force function

$$\mathcal{U} = 3\omega_*^2[A(1-3\gamma^2) + B(1-3\gamma'^2) + C(1-3\gamma''^2)], \tag{17}$$

Eq. (15) has an exact solution. In accordance with [12], we arrive at the following statement.

**Statement.** *If the dissipative matrix $\mathcal{D}$ can be represented as $\mathcal{D} = \lambda\sigma^*$, where $\lambda$ is a certain real number, and the form $Q = y^{\mathrm{T}}\Lambda y$, where $\Lambda = \lambda\mathcal{T}$ is positive definite, then stationary (in the narrow sense) fluctuations of the vector y exist and their one-dimensional density $f_1^*$ is determined by the formula*

$$f_1^*(y, \gamma, \gamma', \gamma'') = c\exp\{-[Q(y) - 2\lambda\mathcal{U}(\gamma, \gamma', \gamma'')]\}; \tag{18}$$

*where c is the normalization constant. Distribution* (18) *is unique and limiting for an arbitrary initial distribution, and the fluctuations are statistically reversible in the Yaglom sense* [12, 13].

**6.** Using the method of orthogonal expansions of a one-dimensional distribution [10, 11], we rewrite kinetic model (14) in the form

$$f_1(y; t) \approx w_1^{\mathrm{s}}(y, m_t K_t)\left[1 + \sum_{l=3}^{n}\sum_{|\mu|=l} c_{\mu t}p_\mu(y)\right]. \tag{19}$$

Here, $w_1^{\mathrm{s}}(y, m_t K_t)$ is the standard distribution, $c_{\mu t}$ are the coefficients of the expansion in known orthogonal polynomials $\{p_\mu(y), q_\mu(y)\}$; and $n$ is the number of the expansion terms. The parameters $m_t$, $K_t$, and $c_{\mu t}$ of the one-dimensional distribution are determined by the ordinary differential equations

$$\dot m_t = \mathcal{A}(m_t, K_t, c_\lambda), \quad m_{t_0} = m_0, \tag{20}$$

$$\dot K_t = \mathcal{H}(m_t, K_t, c_\lambda), \quad K_{t_0} = K_0, \tag{21}$$

$$\dot c_{\mu t} = \mathcal{C}_\mu(m_t, K_t, c_\lambda), \quad c_{\mu t_0} = c_{\mu 0}, \tag{22}$$

where $\lambda, \mu = 1, 2, \ldots, n$; and $\mathcal{A}$, $\mathcal{H}$, and $\mathcal{C}_\mu$ are the given functions.

In the Gaussian approximation (where $f_1$ is approximated by the normal distribution [10, 11]), kinetic model (14) is described by the equations

$$f_1 = f_1(y, m_t, K_t, t) = [(2\pi)^3[K_t]]^{-1/2}\exp\{-(y-m_t)^{\mathrm{T}}K_t^{-1}(y-m_1)\}, \tag{23}$$

$$\dot m_t = \mathcal{A}(m_t, K_t, t) = M_N a(Y, t), \quad m_{t_0} = m_0, \tag{24}$$

$$\dot K_t = \mathcal{H}(m_t, K_t, t) \equiv M_N[a(Y, t)(Y^{\mathrm{T}} - m_t^{\mathrm{T}}) + (Y - m_t)a(Y, t)^{\mathrm{T}} + \sigma(Y, t)],$$
$$\sigma(Y, t) = b(Y, t)\nu(t)b(Y, t)^{\mathrm{T}}, \quad K_{t_0} = K_0. \tag{25}$$

Here, the subscript $N$ means that the mathematical expectation should be evaluated for the equivalent normal distribution with unknown expectations $m_t$ and covariance matrix $K_t$.

**7.** If the parameters correspond to the first harmonics, i.e., the linear fluctuation moments are fixed, the model based on Eqs. (24) and (25) coincides with the spectral correlation model [9].

In the linear approximation, the first and second harmonics of the Earth's inertia tensor are responsible for both additional stochastic oscillations at higher frequencies $m\omega_*$ ($m \geq 2$) and trends. In particular, for $\overline{\mathcal{P}}_2 = \overline{\mathcal{Q}}_2 = \overline{\mathcal{R}}_2 = 0$ and $J_{qr} \ggg J_{pr}$, the average statistical trend in $p_t$ and $q_t$ is determined by the formulas

$$\langle\langle\Delta m_t^p\rangle\rangle = \langle\langle\mathcal{Q}_1\rangle\rangle N_*^{-1}, \quad \langle\langle\Delta m_t^q\rangle\rangle = \langle\langle\mathcal{P}_1\rangle\rangle N_*^{-1}, \tag{26}$$

where

$$\langle\langle\mathcal{P}_1\rangle\rangle = -u_4\left[(m_t^r)^2 + D_t^r + \frac{3}{2}\omega_*^2\left(1 - \frac{3}{2}b_1^2\right)\right] - \frac{3}{2}u_6\omega_*^2\left(1 - \frac{b_1^2}{2}\right),$$
$$\langle\langle\mathcal{Q}_1\rangle\rangle = \frac{3}{2}u_7\omega_*^2\left(1 - \frac{b_1^2}{2}\right).$$

Here, $\langle\langle\ldots\rangle\rangle$ means double averaging over the time intervals $2\pi r_*^{-1}$ and $2\pi\omega_*^{-1}$, and the expectation $m_t^r$ and the variance $D_t^r$ of $r_t$ are determined by Eq. (3). Therefore, in the linear approximation, the second harmonics give rise to additional terms proportional to $b_1^2$.

The inclusion of the nonlinear (in **u**, $p_t$, $q_t$, and $r_t$) components of the moments $\mathcal{P}_{1,2}$, $\mathcal{Q}_{1,2}$, and $\mathcal{R}_{1,2}$ entering into Eqs. (1)–(3) allows us to improve the linear and nonlinear spectral correlation models [7–9]. In this case, by virtue of Eqs. (11) and (12), parametric and nonlinear stochastic perturbations directly affect both the parameters of stochastic oscillations at the frequencies $m\omega_*$ and trends.

## ACKNOWLEDGMENTS

This work was support by the Russian Foundation for Basic Research, project nos. 01-02-17250 and 01-01-00758.

## REFERENCES

1. Annu. IERS Rep. (Central Bureau IERS Observ., Paris, 2003).
2. L. D. Akulenko, S. A. Kumakshev, and Yu. G. Markov, Dokl. Akad. Nauk **379**, 191 (2001) [Dokl. Phys. **46**, 508 (2001)].
3. L. D. Akulenko, S. A. Kumakshev, and Yu. G. Markov, Dokl. Akad. Nauk **382**, 199 (2002) [Dokl. Phys. **47**, 78 (2002)].
4. W. H. Munk and G. J. F. MacDonald, *The Rotation of the Earth* (Cambridge Univ. Press, Cambridge, 1960; Mir, Moscow, 1964).
5. H. Moritz and I. I. Mueller, *Earth Rotation: Theory and Observation* (Ungar, New York, 1987; Naukova Dumka, Kiev, 1992).
6. M. Araty, *Linear Stochastic Systems with Constant Coefficients* (Springer-Verlag, Berlin, 1982; Nauka, Moscow, 1989).
7. Yu. G. Markov and I. N. Sinitsyn, Dokl. Akad. Nauk **385**, 189 (2002) [Dokl. Phys. **47**, 531 (2002)].
8. Yu. G. Markov and I. N. Sinitsyn, Dokl. Akad. Nauk **387**, 482 (2002) [Dokl. Phys. **47**, 867 (2002)].
9. Yu. G. Markov and I. N. Sinitsyn, Astron. Zh. **80** (2), 186 (2003).
10. V. S. Pugachev and I. N. Sinitsyn, *Stochastic Differential Systems: Analyses and Filtering* (Nauka, Moscow, 1990; Wiley, New York, 1987).
11. V. S. Pugachev and I. N. Sinitsyn, *Stochastic Systems: Theory and Applications* (Logos, Moscow, 2000; World Scientific, River Edge, NJ, 2001).
12. N. K. Moshchuk and I. N. Sinitsyn, Dokl. Akad. Nauk SSSR **320**, 1337 (1991) [Sov. Phys. Dokl. **36**, 690 (1991)].
13. A. M. Yaglom, Mat. Sb. **24** (3), 457 (1949).

*Translated by V. Chechin*

*Doklady Physics, Vol. 48, No. 5, 2003, pp. 257–259. Translated from Doklady Akademii Nauk, Vol. 390, No. 3, 2003, pp. 347–349.*


**MECHANICS**

# Unique (Integrated) Fatigue Curve of Metallic Materials

**A. N. Romanov**

Presented by Academician R.F. Ganiev December 3, 2002

Received December 26, 2002

More than a century ago, Woehler established that any metallic construction material is characterized by a fracture curve called a fatigue curve peculiar to the given conditions of cyclic loading. Since then, engineers and investigators have focused their efforts on obtaining fatigue curves for various constructional materials under different loading conditions (soft and rigid loadings, various testing temperatures, loading frequency, asymmetry of a cycle, etc.). These investigations were performed in two directions: elastoplastic-deformation loading, when the number of cycles before fracture is small (low-cycle fatigue with less than $10^4$ cycles before fracture), and elastic (inelastic) loading, when the number of cycles before fracture is large (more than $10^4$ cycles). Later, a unique scientific direction, cyclic fracture mechanics, was divided into the cyclic loading before the formation of a crack and loading at the crack-propagation stage. At the latter stage, as well as at the crack-initiation stage, there are rapture curves corresponding to each material and each loading condition. To date, numerous experimental data on the characteristics of material resistance to cyclic loading have been accumulated for the stages of both the initiation and propagation of cracks. Thousands of handbooks summarize these properties of construction materials used in each branch of mechanical engineering and other fields.

At the same time, rupture criteria for estimating the strength of machines, equipment, and constructions have attracted much attention in force, deformation, and energy approaches. Tens of such criteria have been suggested in each of these approaches [1]. Unfortunately, the available criteria are, as a rule, either the equations of the fatigue curve for a particular material and given loading conditions or valid only for a very limited number of materials and loading conditions. In the former case, the criteria cannot be extended to other materials and other testing conditions. In the latter case, numerous experimental data continue to be required.

*Blagonravov Institute of Mechanical Engineering, Russian Academy of Sciences, M. Khariton'evskiĭ per. 4, Moscow, 101990 Russia*

In this study, a unique fracture criterion based on the hypothesis of the damaging role of microstress on the path of plastic [2] and elastic deformations is obtained. It can be applied for all metallic materials in the entire range of cyclic loading (low- and high-cycle regions). In addition, the criterion is independent of loading conditions (temperature, frequency, and asymmetry of a cycle) at both the crack-initiation and crack-propagation stages under soft loading (loading with a given stress amplitude) [3]. This criterion has the form

$$\int_0^{N_f} \frac{\delta e_{ep}}{\varepsilon^2} dN + \int_0^{N_f} \frac{\Delta\varepsilon}{\varepsilon} dN = 1, \quad (1)$$

where $e_{ep} = \delta + e_e$.

For rigid loading (loading with a given amplitude of elastoplastic strain), it is possible to assume that $\delta$ = const. Then, Eq. (1) can be written in the form

$$\frac{\delta e_{ep}}{\varepsilon^2} N_f = 1. \quad (2)$$

The first term in Eq. (1) is responsible for the level of accumulated damage under the action of cyclic plastic and elastoplastic deformations, whereas the second, to damage due to plastic deformation unilaterally accumulated in the given number of loading cycles. The fracture happens when the level of damage is equal to unity. Dependence (1) makes it possible to find the level of accumulated damage for any number of loading cycles, including programmable loading.

The assumption concerning the damaging role of microstress in elastic and plastic deformations made it possible to describe fracture conditions by a unique dependence (1) in the entire range of fatigue life under cyclic loading [in the ranges of both low- and high-cycle fracture (see figure)].

The criteria obtained indicate that, under cyclic loading, the process of accumulation of damages and the fracture conditions obey a unique rule (law) independently of loading conditions.

Let us introduce the notation

$$\eta_e = \frac{\delta e_{ep}}{\varepsilon^2} \text{ and } \eta_p = \frac{\delta e_{ep} + \Delta\varepsilon\varepsilon}{\varepsilon^2},$$

1028-3358/03/4805-0257$24.00 

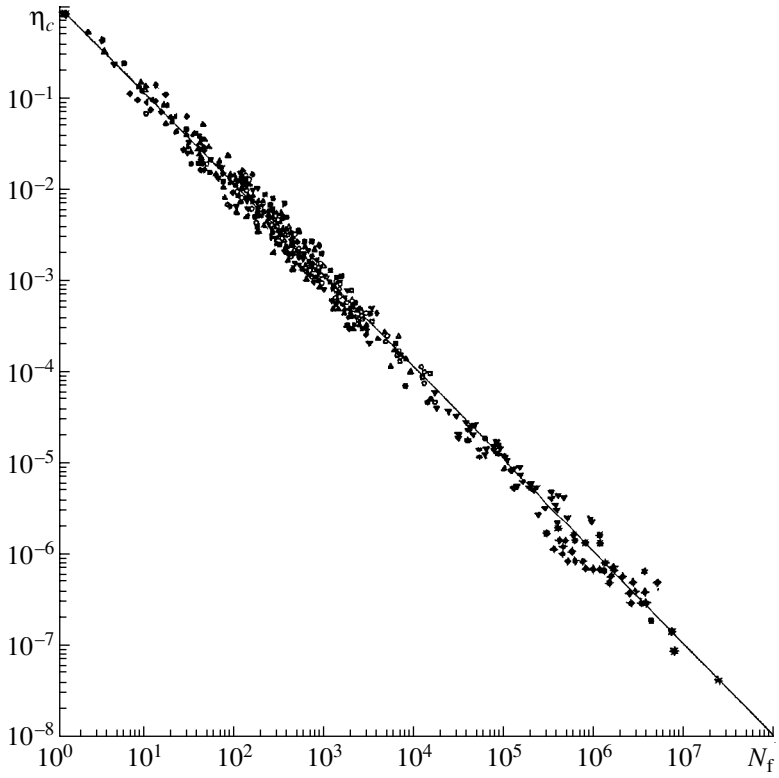


Unique (integrated) fatigue curve.

for rigid and soft loading, respectively. Then, criteria (1) and (2) can be rewritten in the form

$$\eta_e N_f = 1, \quad \eta_p N_f = 1, \tag{3}$$

where $\eta_p$ is defined from the averaged values of $\delta$ and $\Delta\varepsilon$.

Earlier, it was shown [1] that the ratio $\frac{\delta}{\varepsilon}$ satisfactorily defines the cyclic Bauschinger effect for a small number of cycles before fracture. One can assume that this ratio describes the Bauschinger effect in both the low- and high-cycle ranges.

The experimental test of criteria (1) and (2) corroborated the existence of the unique (integrated) fatigue curve for low- and high-cycle loadings (see figure). The integrated fatigue curve is common for all metallic materials (and their structural states, i.e., independent of the thermal-treatment kind) and for all cyclic-loading conditions (temperature, loading frequency, and asymmetry of a cycle). The loading conditions influence the characteristics of the resistance to deformation, which enter into Eqs. (1) and (2). However, they do not change the rule (law) of accumulating damages in accordance with these criteria, including programmable loading (two-frequency loading, steplike loading, overloading, loading with holding in half-cycles of loading, etc.).

Criterion (1) describes the kinetics of damage accumulation, whose ultimate case is the appearance of a macrocrack.

To describe the macrocrack-propagation stage, numerous criteria of final fracture (durability) were also proposed. Unlike the criteria introduced above, these criteria, as well as the available criteria describing the fracture of materials at the stage before initiation of a crack, are not universal.

The application of the concepts described above to the crack-propagation stage made it possible to obtain the durability criterion of a material (a construction) in the form

$$\int_0^{N_f} \frac{v_{ep} v_p}{v_c^2} dN + \int_0^{N_f} \frac{\Delta v}{v_c} dN = 1, \tag{4}$$

where $v_p$, $v_e$, $v_{ep}$, and $\Delta v$ are the plastic (residual and reversible), elastic, and elastoplastic (reversible) displacement of the crack edges in a half-cycle of extension and unilaterally accumulated crack opening in a cycle, respectively; and $v_c$ is the limiting crack opening under the single failure of a sample with a crack.

When crack opening is not accumulated (rigid loading), the second term in Eq. (4) is equal to zero. In this case,

$$\int_0^{N_f} \frac{v_{ep} v_p}{v_c^2} dN = 1. \quad (5)$$

In terms of the notation

$$\eta_{me} = \frac{v_{ep} v_p}{v_c^2}, \quad \eta_{mp} = \frac{v_{ep} v_p + \Delta v \cdot v_c}{v_c^2},$$

criteria (4) and (5) take the form

$$\eta_{me} N_f = 1, \quad \eta_{mp} N_f = 1. \quad (6)$$

Thus, the limiting cases of damage accumulation and loading conditions obey the same law as that for the crack-initiation stage. However, each stage is characterized by individual deformation characteristics.

Criteria (6) are corroborated experimentally (open circles in figure).

To substantiate the existence of the unique fatigue curve, we used the fatigue-test data of the following materials: 22k steel (soft and rigid loading; $r_\sigma$ = –0.3, –0.7, –0.9, and –1.0; specimens with a concentrator; $T$ = 150, 270, 350, and 450°C), TS steel (soft and rigid loading; $r_\sigma$ = –0.3, –0.7, –0.9, and –1.0; notched samples; $T$ = 270, 350, and 450°C), H18N10T steel (soft and rigid loading; $T$ = 250, 450, 550, and 650°C; programmed loading and two-frequency loading; the stages of the initiation and propagation of cracks), 16GNMA ÉShP steel, CSN steel, steel with 0.22% of carbon, 1H13 steel, 45 steel (two-step loading), SAE4340 steel (training), 713C-LC Inconel, 713C-SG Inconel, BW Vaspaloy, BK Vaspaloy, A Vaspaloy, AD-33 ($r_\sigma$ = 0, –1, and +0.5), Ni–Mo steel, and ÉI-437B steel ($T$ = 700°C).

The unique (integrated) fatigue curve is common for

(i) all metallic constructional materials;

(ii) low- and high-cycle fatigues (i.e., the entire range of durability);

(iii) the crack-initiation and crack-propagation stages;

(iv) any kind of loading (cyclic extension–compression, torsion, and bend);

(v) any positive test temperature;

(vi) any loading frequency;

(vii) any asymmetry of a loading cycle;

(viii) rigid loading (loading with a given strain) and soft loading (loading with a given stress in a cycle when the parameters of the curve are taken in average values).

Thus, a unique (integrated) fatigue curve of materials (see figure) exists in the entire range of durability (low- and high-cycle fatigues) independent of the type of a material, its structural state (thermal treatment), the kind of loading (single-frequency, double-frequency, asymmetric, with time lags, and programmable), and loading conditions (temperature and frequency). This circumstance makes it possible to formulate new approaches to fatigue tests of materials, obtaining deformation characteristics, the methods of cyclic strength calculations, the rules of choosing a material in the process of designing, the production of testing and measuring instrumentations, the volume and the character of reference data, and the conditions of optimizing the properties of constructional materials and the kinds of their treatment.

## REFERENCES

1. A. N. Romanov, *Fracture under Small-Cycle Loading* (Nauka, Moscow, 1988).
2. V. V. Novozhilov and O. G. Rybakina, in *Proceedings of the III Conference on Mechanical Problems of Fatigue* (IMASH, Moscow, 1966), p. 71.
3. A. N. Romanov, Dokl. Akad. Nauk **380**, 56 (2001) [Dokl. Phys. **46**, 672 (2001)].

*Translated by Yu. Vishnyakov*